Combined Subject Index

Abatement (pollution) See Pollution abatement		Aircraft components See Airframes	
Abrasion resistant coatings, Mechanical properties Comparison of the Microstructures and Abrasive Wear Properties of Stellite Hardfacing Alloys Deposited by Arc Weld-	1007 10511	Airframes, Materials selection Microstructure Evolution in TIAI Alloys With Boron Additions: Conventional Solidification.	1847-1859A
ing and Laser Cladding. Abrasive wear, Microstructural effects Comparison of the Microstructures and Abrasive Wear Prop-	1037-1054A	Alkali metals See Lithium Potassium	
erties of Stellite Hardfacing Alloys Deposited by Arc Weld- ing and Laser Cladding. Absolute viscosity	1037-1054A	Alkaline earth metal alloys See Magnesium base alloys Strontium	
See Viscosity Absorption (material)		Alkaline earth metal compounds See Beryllium compounds	
See also Hydrogen storage Nonuniformity of NaOH Concentration and Effective Bubble Diameter in CO ₂ injection Into Aqueous NaOH Solution. The Kinetics of Nitrogen Absorption and Desorption From a	5-12B	Alkaline earth metals See Magnesium Strontium Allotropic transformation, Heating effects	
Plasma Arc by Molten Iron. Acicular structure	175-185B	The Influence of Annealing in the Ferrite-Plus-Austenite Phase Field on the Stability of Vanadium Carbide Precipi- tates.	237-245A
Lower Acicular Ferrite. Acid leaching	1811-1818A	Alloy powders, Claddings	COT E-TOT
The Mixed-Control Kinetics of Ferric Chloride Leaching of Galena.	107-110B	Extended Solid Solution and Nonequilibrium Phase Diagram for Ni—Al Alloy Formed During Laser Cladding. Alloy powders Synthesis	363-371A
Acoustic emission Acoustic Emission From Intergranular Subcritical Crack Growth.	637-648A	Alloy powders, Synthesis Production of Nd—Fe—B Alloy Powders Using High- Pressure Gas Atomization and Their Hard Magnetic Prop-	
Quantitative Characterization of Microcracking in A533B Steel by Acoustic Emission. Growth Dynamics Study of the Martensitic Transformation in	1105-1114A	erties. Liquid Break-Up in Gas Atomization of Fine Aluminum Pow- ders.	5-11A 61-69B
Fe—30Ni Alloys. I. Quantitative Measurements of Growth Velocity.	1601-1615A	Alloy steels See Austentitic stainless steels	
Actinide metal alloys See Plutonium base alloys		Carbon manganese steels Chromium molybdenum steels Chromium molybdenum vanadium steels	
Uranium base alloys Actinide metals		Chromium steels Electrical steels Ferritic stainless steels	
See Thorium Uranium		High strength low alloy steels Maraging steels Martensitic stainless steels	
Activation energy Computer Simulation of Thermally Activated Dislocation Motion. III. In FCC Solid Solutions.	1429-1437A	Molybdenum steels Nickel chromium molybdenum steels	
Study of the Mechanism of Fast Diffusion of Cobalt in Tho- rium by Diffusion and Internal Friction Measurements.	2289-2297A	Nickel chromium steels Nickel molybdenum steels Nickel steels	
Activity (chemical) Water and Solute Activities in the Aqueous H ₂ SO ₄ — (NH ₄) ₂ SO ₄ Solutions.	13-20B	Precipitation hardening steels Silicon steels Stainless steels	
Modification of McKay—Perring Method for the Calculation of Mean Activity Coefficients of Solutes in Mixed Solutions. Optical Basicity and the Thermodynamic Properties of Slags.	110-113B 113-118B	Titanium steels Vanadium steels	
Thermodynamic Stability of Potassium β-Alumina. Activities of Boron in the Binary Fe—B, Co—B, and Cu—3 Melts.	687-691B 705-710B	Alloying See Surface alloying Alloys	
Discussion of "Thermodynamic Activity of Na ₂ O in Na ₂ O—CaO—SiO ₂ , Na ₂ O—MgO—SiO ₂ , and Na ₂ O—CaO—	757-758B	See Brazing alloys Casting alloys	
SiO ₂ —Al ₂ O ₃ Melts at 1400°C". Activities of Water and Solutes in the Solution System H ₂ SO ₄ —Cr ₂ (SO ₄) ₃ —H ₂ O.	763-771B	Dispersion hardening alloys Ferrous alloys Precipitation hardening alloys	
Direct Activity Measurements in Liquid Ag—Cu Alloys Using a Valved Knudsen Cell—Mass Spectrometer System.	845-852B	Shape memory alloys Superalloys	
Activity coefficients See Activity (chemical)		Alpha annealing See Annealing	
Adsorption The Mechanism of Adsorption of Aurocyanide Onto Activated Carbon.	315-325B	Alphatizing See Annealing	
Correction to "The Mechanism of Adsorption of Aurocyanide Onto Activated Carbon".	315-325B	Alumina See Aluminum oxide	
Aerospace Cryogenic Toughness of Commercial Aluminum—Lithium Alloys: Role of Delamination Toughening.	485-497A	Aluminum, Alloying elements Effects of Second-Phase Particles on Coarsening of Austenite in 0.15% Carbon Steels.	13-16A
Age hardening See Precipitation hardening		Aluminum, Binary systems An Experimental Technique for the Rapid Determination of Binary Phase Diagrams: the Al—Mg System.	197-203A
Age hardening steels See Precipitation hardening steels		Characterization of the High-Temperature Phase Fields Near Stoichiometric y-TIAI. Phase Equilibria of the AI—Li Binary System.	1899-1906A 2247-2258A
Aging See also Strain aging A Comparison of the Fracture Behavior of Two Heats of the		Aluminum, Casting Mathematical Modeling of an Aluminum Casting Furnace	
Secondary Hardening Steel AF1410. Phase Decomposition of Rapidly Solidified Fe-Mn-Al-C	105-123A	Combustion Chamber. On Identification of the Nucleant in Commercially Pure Alumi-	421-429B
Austenitic Alloys. Effects of Microstructure on the Behavior of an Aluminum Alloy and an Aluminum Matrix Composite Tested Under	205-214A	num Castings Inoculated With < 0.15% Titanium. Dissolution of Reactive Strontium-Containing Alloys in Liquid Aluminum and A356 Melts.	564-566A 815-831B
Low Levels of Superimposed Hydrostatic Pressure. Agitation	2409-2417A	Aluminum, Composite materials Structure of As-Cast Aluminum Matrix Composite Containing	4450
See Electromagnetic stirring Aircomatic welding		Ni ₃ Al-Type Intermetallic Ribbons. Infiltration of Fibrous Preforms by a Pure Metal. I. Theory. Infiltration of Fibrous Preforms by a Pure Metal. II. Experi-	1153-1161A 2535-2547A
See Gas metal arc welding Aircraft		ment. Aluminum, Corrosion	2549-2557A
Influence of Precipitates on the Mechanical Response and Substructure Evolution of Shock-Loaded and Quasi- Statically Deformed AI—LI—Cu Alloys.	1061-1075A	The Influence of Hydrogen on Atomic Binding Energy, Critical Slip Shear Stress, and Fatigue Crack Propagation Rate of Aluminum Single Crystals.	921-924A

The Influence of Water Vapor on the Fatigue Crack Propaga- tion Kinetics in Pure Aluminum Single Crystals.	925-933A	Cavitation Behavior of an Al—Cu Eutectic Alloy During Su- perplastic Deformation.	453-462A
Aluminum, Crystal lattices A Comparison of Ultrasonic and X-Ray Determinations of		Cryogenic Toughness of Commercial Aluminum—Lithium Al- loys: Role of Delamination Toughening. The Development of Blacks Failure Medicine Countailing Ma.	485-497A
Texture in Thin Copper and Aluminum Plates.	2431-2447A	The Development of Plastic Failure Modes in Crystalline Materials: Shear Bands in FCC Polycrystals.	579-593A
Aluminum, Diffusion In Situ Observations of Chemically Induced Grain-Boundary Migration and Discontinuous Precipitation in the		Confirmation of a Thin Sheet Toughening Mechanism and Anisotropic Fracture in Al—Fe—X Alloys. Effects of Microstructure on the Behavior of an Aluminum	2337-2344A
Aluminum—Zinc System. Interdiffusion Coefficients in the Zeta Phase of the Fe—Al	1593-1600A	Alloy and an Aluminum Matrix Composite Tested Under	2409-2417A
System. Interdiffusion in Ternary Fe—Cr—Al Alloys.	2561-2563A 2767-2781A	Low Levels of Superimposed Hydrostatic Pressure. Fatigue Crack Propagation in Rapidly Solidified Aluminum Al- loys at 25°C and 300°C.	2425-2430A
Aluminum, Dopants	2101 21011	Simulation of Static and Deformation-Enhanced Grain	2783-2792A
Improving Tantalum's Oxidation Resistance by Al* Ion Implantation.	2101-2108A	Growth Effects on Superplastic Ductility. Aluminum base alloys, Microstructure	2/03-2/32A
Aluminum, Extraction Physical Chemistry of the Carbothermic Reduction of Alu-		The Electrical Conductivity of Cast Al—Si Alloys in the Range 2-12.6 wt.% Silicon.	383-389A
mina in the Presence of a Metallic Solvent. II. Measure- ments of Kinetics of Reaction.	161-173B	Synthesis and Structural Aspects of Quasicrystals in Mg— Al—Ag System: Mg ₄ Al ₈ Ag.	805-812A
Activities in the Liquid System NaF—MgF ₂ —AIF ₃ . The Effect of Additives on Activities in Cryolite Melts.	671-674B 675-677B	Structural Study of Electrodeposited Aluminum—Manganese Alloys.	1351-1359A
Aluminum, Forming		Correction to "Deformation Mechanisms of a Rapidly Solidi- fied Al—8.8Fe—3.7Ce Alloy".	1713-1719A
Effects of Changes in Strain Path on Work Hardening in Cubic Metals.	2471-2482A	Aluminum base alloys, Nondestructive testing Eddy Current Analysis of Precipitation Kinetics in Aluminum	
Aluminum, Mechanical properties Large-Strain Deformation of Aluminum Single Crystals at Ele-		Alloys. New Ultrasonic Methods for Measuring Deformation and	605-610A
vated Temperature as a Test of the Geometric—Dynamic- Recrystallization Concept.	2182-2185A	Fracture Related Material States.	611-618A
Aluminum, Powder technology	2102 2100	Contacting Surfaces: a Problem in Fatigue and Diffusion Bonding.	627-636A
Flow Separation and Liquid Rundown in a Gas-Atomization Process.	613-622B	Aluminum base alloys, Phase transformations The Effects of Elastic Stress on the Kinetics of Ostwald Ri-	
Influence of Gas Flow on Performance of "Confined" Atom- ization Nozzles.	833-843B	pening: the Two-Particle Problem.	1175-1189A
Aluminum, Solubility Comments on the Solubility of Carbon in Molten Aluminum.	191A	Aluminum base alloys, Powder technology Liquid Break-Up in Gas Atomization of Fine Aluminum Pow-	04 000
The Solubility of Titanium Diboride in Aluminum.	2185-2187A	ders. Influence of Gas Flow on Performance of "Confined" Atom-	61-69B 833-843B
Aluminum, Ternary systems Phase Equilibria in the Al—Fe—C System: Isothermal Sec-		ization Nozzles. Aluminum base alloys, Rolling	833-8438
tions 1550-2300°C. Aluminum, X ray analysis	2703-2706A	Development of Rolling Textures in Aluminum Alloy 3004 Subjected to Varying Hot-Rolling Deformation.	1495-1507A
Real-Time X-Ray Diffraction Investigation of Metal Deforma- tion.	595-604A	Aluminum base alloys, Solubility The Solubility of Hydrogen in Solid Binary Aluminum—	
Aluminum base alloys, Casting On the influence of Coarsening on Microsegregation.		Lithium Alloys.	523-533B
Modeling of Equiaxed Microstructure Formation in Casting.	247-253A 311-322A	Precipitation of Silicon in Aluminum—Silicon: a Calorimetric Analysis of Liquid-Quenched and Solid-Quenched Alloys.	1207-1214A
Electromagnetic Refining of Aluminum Alloys by the CREM Process. I. Working Principle and Metallurgical Results.	623-629B	The Solubility of Hydrogen in Molten Aluminum Alloys. Aluminum base alloys, Structural hardening	1785-1791A
Electromagnetic Refining of Aluminum Alloys by the CREM Process. II. Specific Practical Problems and Their Solu-		Phase Transformations in the Al—Li—Hf and Al—Li—Ti Systems.	999-1019A
tions. Dissolution of Reactive Strontium-Containing Alloys in Liquid	631-643B	Influence of Precipitates on the Mechanical Response and Substructure Evolution of Shock-Loaded and Quasi-	333 101311
Aluminum and A356 Melts. Modeling of Multidimensional Solidification of an Alloy.	815-831B 1833-1845A	Statically Deformed A!—Li—Cu Alloys. Atom-Probe Analysis of GP Zones in an Al—1.7 at.% Cu	1061-1075A
A Statistically Significant Experimental Technique for Investi- gating Microsegregation in Cast Alloys.	2529-2533A	Alloy.	1585-1591A
Aluminum base alloys, Coatings The Effects of Silicon on the Reaction Between Solid Iron and		Aluminum base alloys, Welding Three-Dimensional Transient Model for Arc Welding Process:	645-659B
Liquid 55 wt.% Al—Zn Bath.	543-555A	Aluminum compounds See also Aluminum oxide	
Aluminum base alloys, Composite materials Wetting of Ceramic Particulates With Liquid Aluminum Alloys.		Aluminum compounds, Composite materials	
 Experimental Techniques. Wetting of Ceramic Particulates With Liquid Aluminum Alloys. 	527-532A	Structure of As-Cast Aluminum Matrix Composite Containing Ni ₃ Al-Type Intermetallic Ribbons.	1153-1161A
II. Study of Wettability. Study of the Interface and its Effect on Mechanical Properties	533-541A	Microstructural Observations of Pressure Cast Ni ₃ Al/Al ₂ O ₃ and Ni/Al ₂ O ₃ Composites.	2159-2166A
of Continuous Graphite Fiber-Reinforced 201 Aluminum. Crack Bridging by Uncracked Ligaments During Fatigue-	727-739A	Interface Characterization of Fiber-Reinforced Ni ₃ Al Matrix Composites.	2459-2469A
Crack Growth in SiC-Reinforced Aluminum-Alloy Compos- ites.	897-908A	Aluminum compounds, Crystal growth Intermetallic Compound Layer Growth at the Interface of	
Friction Properties of AI—1.5Mg/SiC Particulate Metal-Matrix Composites.	1564-1566A	Solid Refractory Metals Molybdenum and Niobium With Molten Aluminum.	825-836A
Recrystallization Microstructure in Cold-Rolled Aluminum Composites Reinforced by Silicon Carbide Whiskers.	1743-1753A	Aluminum compounds, Mechanical properties	
Involvement of Processing Defects in Failure of FP/Al—Li. Deformation of Whisker-Reinforced Metal-Matrix Compos-	2175-2179A	The Effect of Molybdenum Addition on Properties of Iron Al- uminides.	751-757A
ites Under Changing Temperature Conditions. Aluminum base alloys, Corrosion	2355-2368A	Notch Effects in Tensile Behavior of Ni ₃ Al and Ni ₃ Al + B. Microstructure and Tensile Properties of Fe40 at.% Al Al-	1247-1255A
The Influence of Hydrogen on Atomic Binding Energy, Critical Slip Shear Stress, and Fatigue Crack Propagation Rate of		loys With C, Zr, Hf, and B Additions. Grain-Boundary Contamination and Ductility Loss in Boron-	1701-1714A
Aluminum Single Crystals. Mode I Stress Intensity Factors Induced by Fracture Surface	921-924A	Doped Ni ₃ Al. Aluminum compounds, Microstructure	2017-2023A
Roughness Under Pure Mode III Loading: Application to the Effect of Loading Modes on Stress Corrosion Crack		Microstructure Evolution in TIAI Alloys With Boron Additions: Conventional Solidification.	1847-1859A
Growth.	1989-1999A	On the Mechanism of Cross Slip in Ni ₃ Al.	2811-2818A
Retrogression and Reaging and the Role of Dislocations in the Stress Corrosion of 7000-Type Aluminum Alloys. Microstructure and Corrosion Behavior of As-Cast and Heat-	2087-2092A	Aluminum compounds, Oxidation Transient Oxidation of Single-Crystal β -NiAl.	499-518A
Treated Al—4.5 wt.% Cu—2.0 wt.% Mn Alloys.	2499-2516A	Aluminum killed steels, Forming Experimental Investigation and Finite Element Modeling of	
Aluminum base alloys, Crystal growth Discussion of "The Mechanism of Silicon Modification in		Hemispherically Stretched Steel Sheet. Calculation of the Forming Limit Diagram.	1509-1521A 1975-1987A
Aluminum—Silicon Alloys: Impurity-Induced Twinning". Aluminum base alloys, Directional solidification	1286-1290A	Effects of Changes in Strain Path on Work Hardening in Cubic Metals.	
The Columnar-to-Equiaxed Transition in Al—3Cu.	731-734B	Aluminum killed steels, Microstructure	2471-2482A
Aluminum base alloys, Forming Calculation of the Forming Limit Diagram.	1975-1987A	Graphite Formation in High-Purity Cold-Rolled Carbon Steels.	1917-1925A
Aluminum base alloys, Mechanical properties Evidence of a Thin Sheet Toughening Mechanism in Al-		Aluminum oxide, Composite materials Microstructural Observations of Pressure Cast Ni ₃ Al/Al ₂ O ₃	
Fe—X Alloys.	155-164A	and Ni/Al ₂ O ₃ Composites.	2159-2166A

Involvement of Processing Defects in Failure of FP/AI—Li.	2175-2179A	Atomic reactors	
Micromechanics and Fatigue Crack Growth in an Alumina- Fiber-Reinforced Magnesium Alloy Composite. Infiltration of Fibrous Preforms by a Pure Metal. I. Theory.	2369-2378A	See Nuclear reactors Atomization	
Infiltration of Fibrous Preforms by a Pure Metal. II. Experi-	2535-2547A	See Atomizing	
ment. Amorphous materials	2549-2557A	Atomizing Production of Nd—Fe—B Alloy Powders Using High-	
See Metallic glasses		Pressure Gas Atomization and Their Hard Magnetic Properties.	5-11A
Formation of Metastable Structures and Amorphous Phases in Plutonium-Based Systems Using the Sputtering Tech-		Liquid Break-Up in Gas Atomization of Fine Aluminum Pow- ders.	61-69B
nique. Structural Study of E'n trodeposited Aluminum—Manganese	813-823A	A Mathematical Model of the Spray Deposition Process. Flow Separation and Liquid Rundown in a Gas-Atomization	71-85A
Alloys.	1351-1359A	Process. Influence of Gas Flow on Performance of "Confined" Atomization Nozzles.	613-622B 833-843B
Analyzing See Depth profiling Mathematical analysis		Attenuation	033-0430
Quantitative analysis Statistical analysis		See Ultrasonic attenuation Austenite	
Stress analysis Surface analysis (chemical)		See Retained austenite	
X ray diffraction		Austenitic stainless steels, Composite materials High Temperature Reaction Zone Growth in Tungsten Fiber	
See Crystal growth		Reinforced Superalloy Composites. II. Matrix Chemistry Effects.	267-272A
Androforming See Stretch forming		Austenitic stainless steels, Corrosion Behavior of Sensitized AISI Types 321 and 347 Austenitic	
Anisotropy Confirmation of a Thin Sheet Toughening Mechanism and		Stainless Steels in Hydrogen.	2187-2190A
Anisotropic Fracture in Al—Fe—X Alloys.	2337-2344A	Austenitic stainless steels, Forming Effects of Changes in Strain Path on Work Hardening in Cubic Metals.	2471-2482A
Annealing See also Solution annealing		Austenitic stainless steels, Mechanical properties	
Vacuum annealing The Effect of Microstructure on Properties and Behaviors of	63-7CA	Effect of Copper on the Strength of AISI 316 Stainless Steel. The Effect of Small Plastic Deformation and Annealing on the	421-429A
Annealed Fe ₇₈ B ₁₃ Si ₈ Amorphous Alloy Ribbon. The Influence of Annealing in the Ferrite-Plus-Austenite Phase Field on the Stability of Vanadium Carbide Precipi-	03-7CA	Properties of Polycrystais. I. Experimental Observations. The Effect of Small Plastic Deformation and Annealing on the	471-477A
tates. The Effect of Microstructure of Ferritic Spheroidal Graphite	237-245A	Properties of Polycrystals. II. Theoretical Model for the Transformation of Nonequilibrium Grain Boundaries.	479-484A
Cast Irons on intergranular Fracture at Intermediate Temperatures.	431-436A	Austenitic stainless steels, Metallography Analytical Electron Microscopy Studies of Radiation Damage.	2663-2671A
The Effect of Small Plastic Deformation and Annealing on the Properties of Polycrystals. I. Experimental Observations.	471-477A	Austenitic stainless steels, Nondestructive testing	
The Effect of Small Plastic Deformation and Annealing on the Properties of Polycrystals, II. Theoretical Model for the		Acoustic Emission From Intergranular Subcritical Crack Growth.	637-648A
Transformation of Nonequilibrium Grain Boundaries. The Microstructures of Strip-Cast Low-Carbon Steels and	479-484A	Austenitic stainless steels, Phase transformations Effect of Strain Rate on Martensitic Transformation During	
Their Response to Thermal Processing. The Microstructure of Rolled and Annealed Tungsten Rod.	1191-1198A 1669-1686A	Unlexial Testing of AISI-304 Stainless Steel. Austenitic stainless steels, Phases (state of matter)	2857-2859A
Graphite Formation in High-Purity Cold-Rolled Carbon Steels. Grain-Boundary Contamination and Ductility Loss in Boron-	1917-1925A	Phase Decomposition of Rapidly Solidified Fe—Mn—Al—C Austenitic Alloys.	205-214A
Doped Ni ₃ Al. Particle Bonding, Annealing Response, and Mechanical	2017-2023A	Austenitic stainless steels, Powder technology	200 21 101
Properties of Dynamically Consolidated Type 304 Stainless Steel Powders.	2449-2457A	Particle Bonding, Annealing Response, and Mechanical Properties of Dynamically Consolidated Type 304 Stainless	
Reaction Rate Theory Perspectives on Some Problems in Materials Science.	2583-2598A	Steel Powders. Austenitic stainless steels, Structural hardening	2449-2457A
Impurity-Defect Interactions in Radiation Hardening and Em- brittlement in BCC Metals.	2637-2649A	Martensite Formation, Strain Rate Sensitivity, and Deforma- tion Behavior of Type 304 Stainless Steel Sheet.	1239-1246A
Antifriction bearings See Ball bearings		Austenitic stainless steels, Welding Emission Spectroscopy of Plasma During Laser Welding of	
Antimony, Diffusion		AISI 201 Stainless Steel. Heat Transfer During Nd:YAG Pulsed Laser Welding and its	277-286B
The Effect of Chromium on Antimony and Nickel Grain Boundary Segregation in Iron.	2170-2171A	Effect on Solidification Structure of Austenitic Stainless Steels.	957-967A
Antimony, Ternary systems Thermodynamic Consistency of the Ternary Functions.	2047-2055A	On Microstructure—Property Correlation of Thermally Aged Type 316L Stainless Steel Weld Metal.	1115-1124A
Antineutrinos		Austenitizing	
See Antiparticles Antineutrons		Duplex Treatment of High-Strength Steels. Auto oxidation	1687-1699A
See Antiparticles Antiparticles		See Oxidation Autodiffusion	
Possible NDE Correlation With Fractography in 4340 Steel.	323A	See Diffusion	
Antiprotons See Antiparticles		Autogenous smelting See Flash smelting	
Arc welding See also Flux core wire welding		Automobile components See Automotive components	
Gas metal arc welding Gas tungsten arc welding		Automobiles	
Shielded metal arc welding Submerged arc welding		See Automotive bodies Automotive bodies, Forming	
The Kinetics of Nitrogen Absorption and Desorption From a Plasma Arc by Molten Iron.	175-185B	Experimental Investigation and Finite Element Modeling of Hemispherically Stretched Steel Sheet.	1509-1521A
Three-Dimensional Transient Model for Arc Welding Process. Comparison of the Microstructures and Abrasive Wear Prop-		Automotive components	
erties of Stellite Hardfacing Alloys Deposited by Arc Weld- ing and Laser Cladding.	1037-1054A	See also Automotive bodies Automotive components, Heat treatment	
Arc welds See Welded joints		Analytical Models for the Gas Carburizing Process.	535-546B
Argon arc welding		Automotive components, Mechanical properties Parameters Affecting Sag Resistance in Spring Steels.	1951-1959A
See Gas tungsten arc welding Arrhenius activation energy		Bacterial leaching Microbiological Leaching of Copper From Lead Mattes.	773-779B
See Activation energy Atmospheres		Bainite The Bainite Transformation in a Silicon Steel.	324-334A
See Controlled atmospheres		Bainite Formation in a Silver—Cadmium Alloy.	1169-1174A
Atomic diffusion See Diffusion		Bainite, Alloying effects The Microstructure of Chromium—Tungsten Steels.	373-382A

Ball bearings, Mechanical properties Fracture and Fatigue Crack Propagation Properties of Har-		Borides, Solubility The Solubility of Titanium Diboride in Aluminum.	2185-2187A
dened 52100 Steel.	1961-1973A	Boron, Alloying additive	
See Oxygen steel making		Notch Effects in Tensile Behavior of Ni ₃ Al and Ni ₃ Al + B. Microstructure and Tensile Properties of Fe—40 at.% Al Al-	1247-1255A
Basic oxygen steel making See Oxygen steel making		loys With C, Zr, Hf, and B Additions. Microstructure Evolution in TiAl Alloys With Boron Additions: Conventional Solidification.	1701-1714A 1847-1859A
See Vacuum annealing		Boron, Composite materials	10.11
Batch type furnaces		Interface Characterization of Fiber-Reinforced Ni ₃ Al Matrix Composites.	2459-2469A
See Bottom blown converters Bauschinger effect		Boron, Dopants Grain-Boundary Contamination and Ductility Loss in Boron-	
Parameters Affecting Sag Resistance in Spring Steels.	1951-1959A	Doped Ni ₃ Al. Improved Ductility of Ni ₃ Si by Microalloying With Boron or	2017-2023A
BCC metals, Irradiation Tracer Diffusion.	2577-2582A	Carbon. Boron, Reactions (chemical)	2025-2032A
Beams (radiation) See Ion beams		Activities of Boron in the Binary Fe—B, Co—B, and Cu—B Melts.	705-710B
Beams (structural) See I beams		Boron carbide, Composite materials	
Bearing steels, Mechanical properties Fracture and Fatigue Crack Propagation Properties of Hardened 52100 Steel.	1961-1973A	Interface Characterization of Fiber-Reinforced Ni ₃ Al Matrix Composites. Boron compounds	2459-2469A
Bearings	1001 10101	See Boron carbide BOS process	
See Ball bearings Beds		See Oxygen steel making	
See Fluidized beds Beehive kilns		Steel Dissolution in Quiescent and Gas Stirred Fe/C Melts.	363-374B
See Kilns		See Grain boundaries	
Bendability See Formability		Grain sub boundaries Phase boundary	
Beryllium compounds, Mechanical properties Mechanical Properties of High-Temperature Beryllium Inter-		Boundary lubrication See Lubrication	
metallic Compounds.	1279-1282A	Brasses, Corrosion	
Binary systems, Phases (state of matter) An Experimental Technique for the Rapid Determination of Binary Phase Diagrams: the Al—Mg System.	197-203A	The SCC of Single Crystals of β Brass in Water: Fractography and Crystallography.	1439-1444A
Freezing Diagrams. I. Development and Implications for Glass Formability.	287-297A	Brasses, Forming Effects of Changes in Strain Path on Work Hardening in	
Freezing Diagrams. II. Comparison With Experimental Observation and Relevance to Crystallization of Metallic Glass.	299-309A	Cubic Metals. Brasses, Mechanical properties	2471-2482A
Determination of the Fe—Ni Phase Diagram Below 400°C. Some Phase-Diagram Aspects of the Manganese—Carbon	719-725A	Elastic Interaction Stresses. II. The Influence of Orientation on Stresses Generated in Iso-Axial Bicrystals.	1461-1473A
System. Metastable Phase Equilibria in the Lead—Tin Alloy System. I.	747-754B	Transient Tensile Behavior of Interstitial-Free Steel and 70/30 Brass Following Plane-Strain Deformation.	1483-1493A
Experimental. Metastable Phase Equilibria in the Lead—Tin Alloy System.	785-794A	Brasses, Metal working	
II. Thermodynamic Modeling. Mass Spectrometric Study of the Partial Phase Diagram of	795-803A 975-976A	Experimental Deformation Textures of OFE Copper and 70:30 Brass From Wire Drawing, Compression, and Tor-	125-131A
the Fe—Ge System Above 1050°C. Phase Diagrams in Materials Science. Phase Diagrams in Materials Science.	1295-1323A 1295-1323B	sion. Brasses, Microstructure	125-131A
Characterization of the High-Temperature Phase Fields Near Stoichiometric γ -TiAl.	1899-1906A	Microstructure of High-Tensile Strength Brasses Containing Silicon and Manganese.	1199-1206A
Phase Equilibria of the Al—Li Binary System. Binding energy, Corrosion effects	2247-2258A	Nonbasal Plane Defects in 18R Martensite and the Effect of Abnormal Defects on Thermoelastic Martensitic Transfor-	4004 40004
The Influence of Hydrogen on Atomic Binding Energy, Critical Slip Shear Stress, and Fatigue Crack Propagation Rate of		mation. Brasses, Rolling	1631-1636A
Aluminum Single Crystals.	921-924A	Shear Band Formation in Heavily Cold Rolled 70-30 Brass. Braze	1267-1275A
Observations on the Faceted Fatigue Fracture of Cast Co—	00 4004	See Brazing	
Cr—Mo Alloy Used for Surgical Implants. Grain Egression: a New Mechanism of Fatigue-Crack Initiation in Ti—6AI—4V.	99-103A 1715-1725A	Braze bonding See Brazing	
Bismuth, Dopants	1715-1725A	Brazing The Interaction of Reaction-Bonded Silicon Carbide and Inco-	
Fatigue Crack Growth and Fracture Behavior of Bismuth- Doped Copper Bicrystals.	1221-1231A	nel 600 With a Nickel-Based Brazing Alloy.	1803-1810A
Bismuth, Impurities Gas Phase Embrittlement by Metal Vapors.	184-188A	Brazing alloys The Interaction of Reaction-Bonded Silicon Carbide and Inco- nel 600 With a Nickel-Based Brazing Alloy.	1803-1810A
Blades See Turbine blades		Brick kilns	1000-1010A
Blankets (atmospheres)		See Kilns Bridgman method	
See Controlled atmospheres Blast furnace practice		See Crystal growth	
Conceptual Model of the Iron Blast Furnace Considering Thermodynamic and Kinetic Constraints on the Process.	205-218B	Brine See Salt water	
Discussion of "Thermodynamic Activity of Na ₂ O in Na ₂ O—CaO—SiO ₂ , Na ₂ O—MgO—SiO ₂ , and Na ₂ O—CaO—SiO ₂ —Al ₂ O ₃ Melts at 1400°C".	757-758B	Brittle fracture, Temperature effects Variation of Brittle Fracture With Test Temperature in Tempered Martensitic Structure in 25i—0.4C Steel.	560-563A
Blunging See Mixing		Brittleness See Temper brittleness	
Body centered cubic metals		Bubbles	470 404
See BCC metals Boiler tubes, Corrosion		On the Formation of Potassium Bubbles in Tungsten Rod. Bubbling	179-184A
The Effects of Heat Treatment on the Sensitization and SCC Behavior of Inconel 600 Alloy. Bomb reduction	1077-1088A	Mathematical Modeling of Mixing Phenomena in a Gas Stirred Liquid Bath.	53-59B
See Reduction (chemical)		Building up See Hard surfacing	
See Pressure vessels		See Blast furnace practice	
Bonding strength Contacting Surfaces: a Problem in Fatigue and Diffusion Bonding.	627-636A	Butt welds, Mechanical properties Effects of Microstructure on Fatigue Crack Initiation and Propagation of 16Mn Steel.	413-419A

Cadmium, Recovering Cementation of Cobalt, Nickel and Cadmium in Ammoniacal • Medium Using Zinc Metal.	547-550B	Stress Relaxation of an AISI 1080 Steel. Cleavage Fracture in Pearlitic Eutectoid Steel. Discussion of "Correlations of Microstructure With Dynamic and Quasi-Static Fracture in a Plain Carbon Steel".	2011-2015A 2321-2335A 2860-2862A
Cadmium, Ternary systems Thermodynamic Consistency of the Ternary Functions.	2047-2055A	Carbon steels, Metal working Austenite Recrystallization and Carbonitride Precipitation in	-49
See Zone melting		Niobium Microalloyed Steels. Carbon steels, Microstructure	25-38A
Cage zone refining See Zone melting		Effects of Second-Phase Particles on Coarsening of Austen- ite in 0.15% Carbon Steels.	13-16A
Calcining See Roasting		Carbon steels, Rolling Effect of Deformation on Ferrite Nucleation and Growth in a Plain Carbon and Two Microalloyed Steels.	987-998A
Calorimetry Precipitation of Silicon in Aluminum—Silicon: a Calorimetric Analysis of Liquid-Quenched and Solid-Quenched Alloys.	1207-1214A	Carbon steels, Structural hardening The influence of Copper Precipitation and Plastic Deforma-	307-35UN
Carbides See also Boron carbide Silicon carbide Titanium carbide		tion Hardening on the Impact-Transition Temperature of Rolled Structural Steels. Precipitation and Fine Structure in Medium-Carbon Vanadium and Vanadium/Niobium Microalloyed Steels.	1657-1668A 2279-2288A
Carbides, Solubility Carbide Stability Diagrams in 2.25Cr—1Mo Steels.	1561-1564A	Carbon steels, Welding Prediction of Weld Pool and Reinforcement Dimensions of	007.0470
Carbon, Alloying additive Microstructure and Tensile Properties of Fe-40 at.% Al Al-		GMA Welds Using a Finite-Element Model. Lower Acicular Ferrite. Carbothermic reactions	937-947B 1811-1818A
loys With C, Zr, Hf, and B Additions. Carbon, Binary systems Some Phase-Diagram Aspects of the Manganese—Carbon	1701-1714A	Physical Chemistry of the Carbothermic Reduction of Alumina in the Presence of a Metallic Solvent. II. Measurements of Kinetics of Reaction.	161-173B
System. Carbon, Diffusion	747-754B	Carburization See Carburizing	
On the Diffusion of Carbon in Titanium Carbide.	403-411A	Carburizing	
Carbon, Dopants Improved Ductility of Ni ₃ Si by Microalloying With Boron or Carbon.	2025-2032A	See also Pack carburizing Analytical Models for the Gas Carburizing Process. A Mathematical Model Describing Carburization in Multielement Alloy Systems.	535-546B 1021-1028A
Carbon, Solubility Comments on the Solubility of Carbon in Molten Aluminum.	191A	Case carburizing See Carburizing	1027-1020-1
Carbon, Ternary systems Thermodynamic Properties of the Co—W—C System. Phase Equilibria in the AI—Fe—C System: Isothermal Sec-	935-956A	Case hardening See Carburizing	
tions 1550-2300°C.	2703-2706A	lon nitriding Nitriding	
See Boron carbide		Pack carburizing	
Carbides Carbon dioxide		Cast iron See also Nodular iron	
Titanium carbide Carbon dioxide, Diffusion Diffusivities and Viscosities of Some Gases at Elevated Temperatures: Gas Diffusivities in Porous Solids.	141-148B	Cast iron, Directional solidification Effect of Tellurium on Morphological Transitions in Fe—C— Si Alloys. I. Directional Solidification. Effect of Tellurium on Morphological Transitions in Fe—C—	1867-1873A
Carbon dioxide, Reactions (chemical) Studies of the Interfacial Kinetics of the Reaction of CO ₂ With		Si Alloys. II. Auger Analysis. Casting	1875-1881A
Liquid Iron—Nickel Alloys at 1873K. Carbon dioxide, Sorption	755-756B	See also Ceramic mold casting Continuous casting Ingot casting	
Nonuniformity of NaOH Concentration and Effective Bubble Diameter in CO ₂ Injection Into Aqueous NaOH Solution.	5-12B	Melt spinning Pressure casting	
Carbon Fibers, Coating Carbon Fibers Coated With Chromium Carbide Using the Liq- uid Metal Transfer Agent Technique.	165-170A	Slab casting Mathematical Modeling of an Aluminum Casting Furnace Combustion Chamber. Primary Dendrite Spacing and the Effect of Off-Axis Heat	421-429B
Carbon in pulp process The Mechanism of Adsorption of Aurocyanide Onto Activated		Flow.	969-973A
Carbon. Correction to "The Mechanism of Adsorption of Aurocyanide Onto Activated Carbon".	315-325B 315-325B	Casting alloys, Microstructure The Electrical Conductivity of Cast Al—Si Alloys in the Range 2-12.6 wt.% Silicon.	383-389A
Carbon manganese steels, Welding Effects of Microstructure on Fatigue Crack Initiation and Propagation of 16Mn Steel.	413-419A	Cavitation The Effect of Void Shape on Void Growth and Ductility in Axisymmetric Tension Tests.	853-861A
Carbon steels See also Aluminum killed steels		Investigations on the Influence of Internal Nitridation on Creep Crack Growth in Alloy 800H.	1553-1560A
Carbon manganese steels Killed steels		Cavitation, Deformation effects Cavitation Behavior of an Ai—Cu Eutectic Alloy During Superplastic Deformation.	453-462A
Carbon steels, Casting Effect of Thermal Conditions and Alloying Constituents (Ni,Cr) on Macrosogregation in Continuously Cast High-		Cetis See Electrolytic cells	
Carbon (0.8%), Low-Alloy Steel. The Microstructures of Strip-Cast Low-Carbon Steels and Their Response to Thermal Processing.	893-910B 1191-1198A	Cellular precipitates Phase Decomposition of Rapidly Solidified Fe—Mn—Al—C Austenitic Alloys.	205-214A
Carbon steels, Corrosion Tribologically-Driven Steady-State Hydrogen Evolution From Mild Steel by Electrochemical Extraction Technique.	557-560A	Cementation Cementation of Cobalt, Nickel and Cadmium in Ammoniacal	
Carbon steels, Forming Workability of 1045 Spheroidized Steel Under Superimposed		Medium Using Zinc Metal. Cemented carbides, Coating A TEM Study of CVD TiC _x /Ti(C, N) _x Coating on WC—Co Ce-	
Hydrostatic Pressure. Carbon steels, Heat treatment Analytical Models for the Gas Carburizing Process.	535-546B	mented Carbide. Ceramic coatings	279-285B
Carbon steels, Mechanical properties		Carbon Fibers Coated With Chromium Carbide Using the Liq- uid Metal Transfer Agent Technique. Plasma Spraying of Ceramic Particles in Argon—Hydrogen	165-170A
Effect of Phosphorus on the Formation of Retained Austenite and Mechanical Properties in Silicon-Containing Low-Carbon Steel Sheet. The Effect of Carbon Londing on the Dislocation Structure of	437-445A	D.C. Plasma Jets: Modeling and Measurements of Particles in Flight Correlation With Thermophysical Properties of Sprayed Layers.	
The Effect of Cyclic Loading on the Dislocation Structure of Fully Pearlitic Steel. Variation of Brittle Fracture With Test Temperature in Tem-	447-451A	A TEM Study of CVD TiC _x /Ti(C, N) _x Coating on WC—Co Cemented Carbide.	
pered Martensitic Structure in 2Si-0.4C Steel. Thermomechanical Fatigue, Oxidation, and Creep. I. Damage	560-563A	Ceramic mold casting Modeling of Multidimensional Solidification of an Alloy.	1833-1845A
Mechanisms. Thermomechanical Fatigue, Oxidation, and Creep. I. Life Prediction.	1755-1767A 1769-1783A	Ceramics See Silicon nitride	

CGF forging process See Forging		Chromium steels, Mechanical properties Elastic Limits and Microplastic Response in Ultrahigh	400 4044
Chalcogenides See Sulfides		Strength Carbon Steels. Heat Treatment Behavior and Tensile Properties of Cr—W Steels.	188-191A 463-470A
Chambers See Combustion chambers		Parameters Affecting Sag Resistance in Spring Steels. Chromium steels, Metal working	1951-1959A
Chapmenizing See Nitriding		Standard Gibbs Energies of Formation of the Carbides of Chromium by EMF Measurements.	911-917B
Chemical analysis		Chromium steels, Microstructure The Microstructure of Chromium—Tungsten Steels.	373-382A
See Depth profiling Quantitative analysis Surface analysis (chemical)		Chromium vanadium steels See Chromium molybdenum vanadium steels	
Chemical kinetics		Circuits	
See Reaction kinetics		See Integrated circuits Cladding	
Chemical processes See Reactions (chemical)		See also Weld cladding Comparison of the Microstructures and Abrasive Wear Prop-	
Chemical reactions See Reactions (chemical)		erties of Stellite Hardfacing Alloys Deposited by Arc Weld- ing and Laser Cladding.	1037-1054A
Chemical reduction See Reduction (chemical)		Laser-Clad Ni ₇₀ Al ₂₀ Cr ₇ Hf ₃ Alloys With Extended Solid Solution of Hafnium. I. Microstructure Evolution.	2267-2277A
Chemical tests		Laser-Clad Ni ₇₀ Al ₂₀ Cr ₇ Hf ₃ Alloys With Extended Solid Solution of Hafnium. II. Oxidation Behavior.	2489-2497A
See Depth profiling Quantitative analysis		Cleavage Cleavage Fracture in Pearlitic Eutectoid Steel.	2321-2335A
Surface analysis (chemical)		Clustering	EGET EGGGY
Chemistry See Electrochemistry		Modeling the Early Stages of Thin Film Formation by Ener- getic Atom Deposition.	2609-2617A
Physical chemistry Thermochemistry		Coal High-Pressure Coal Injection in Zinc Slag Fuming.	227-235B
Chlorination Mass Spectrometric Observations of Metal Oxychlorides		Coal Desulfurization With Aqueous Chlorine.	567-571B
Produced by Oxidation—Chlorination Reactions.	1566-1568A	See Coalescing	
Chromium, Alloying elements Effect of Thermal Conditions and Alloying Constituents		Coalescing On the Influence of Coarsening on Microsegregation.	247-253A
(Ni,Cr) on Macrosegregation in Continuously Cast High- Carbon (0.8%), Low-Alloy Steel.	893-910B	Coating	
The Effect of Chromium on Antimony and Nickel Grain Boundary Segregation in Iron.	2170-2171A	See Hot dip coating Immersion coating	
Chromium, Diffusia m Interdiffusion in Ternary Fe—Cr—Al Alloys.	2767-2781A	Silver plating Coatings	
Chromium, Refining Upgrading Ferrochromium to Chromium by Nitriding, Leach-		See Abrasion resistant coatings Ceramic coatings	
ing, and Dissociation.	219-226B	Diffusion coatings Electroplates	
Chromium molybdenum nickel steels See Nickel chromium molybdenum steels		Protective coatings Cobalt, Diffusion	
Chromium molybdenum steels		Study of the Mechanism of Fast Diffusion of Cobalt in Tho- rium by Diffusion and Internal Friction Measurements.	2289-2297A
See also Chromium molybdenum vanadium steels Nickel chromium molybdenum steels		Cobalt, Quaternary systems	
Chromium molybdenum steels, Alloy development Effects of Manganese, Silicon, and Purity on the Design of		A Study of the Thermodynamics and Phase Relationships of the Fe—Co—S—O Quaternary System.	1523-1532A
3.5NiCrMoV, 1CrMoV, and 2.25Cr—1Mo Bainitic Alloy Steels.	2197-2212A	Cobalt, Recovering Cementation of Cobalt, Nickel and Cadmium in Ammoniacal	
Chromium molybdenum steels, Claddings Phase Transformations at Steel/IN625 Clad Interfaces.	665-681A	Medium Using Zinc Metal. Cobalt, Ternary systems	547-550B
Chromium molybdenum steels. Heat treatment	000 00111	Thermodynamic Properties of the Co—W—C System.	935-956A
The Influence of Tempering Temperature on Small Fatigue Crack Behavior Monitored With Surface Acoustic Waves in Quenched and Tempered 4140 Steel.	1257-1265A	Cobalt base alloys, Coatings Comparison of the Microstructures and Abrasive Wear Properties of Stellite Hardfacing Alloys Deposited by Arc Weld-	
Chromium molybdenum steels, Mechanical properties Degradation of Mechanical Properties of Cr—Mo—V and		ing and Laser Cladding. Cobalt base alloys, Irradiation	1037-1054A
2.25Cr—1Mo Steel Components After Long-Term Service at Elevated Temperatures.	87-97A	Reaction Rate Theory Perspectives on Some Problems in Materials Science.	2583-2598A
Microvoid Formation During Shear Deformation of Ultrahigh Strength Steels.	143-153A	Cobalt base alloys, Mechanical properties	
Elastic Limits and Microplastic Response in Ultrahigh Strength Carbon Steels.	186-191A	Observations on the Faceted Fatigue Fracture of Cast Co— Cr—Mo Alloy Used for Surgical Implants.	99-103A
Chromium molybdenum steels, Solubility Carbide Stability Diagrams in 2.25Cr—1Mo Steels.	1561-1564A	Cobalt base alloys, Reactions (chemical) Activities of Boron in the Binary Fe—B, Co—B, and Cu—B	
Chromium molybdenum vanadium steels, Mechanical	1301-13047	Melts.	705-710B
properties Degradation of Mechanical Properties of Cr—Mo—V and		See Crack opening displacement	
2.25Cr—1Mo Steel Components After Long-Term Service at Elevated Temperatures.	87-97A	Coefficient of expansion See Thermal expansion	
Near-Threshold Fatigue Crack Growth Properties at Elevated Temperature for 1Cr—1Mo—0.25V Steel and 12Cr Stain-		Coefficient of friction See Friction	
less Steel. The influences of Impurity Content, Tensile Strength, and	741-749A	Coefficient of thermal expansion	
Grain Size on In-Service Temper Embrittlement of CrMoV Steels.	2345-2354A	See Thermal expansion Coercive force	
Chromium nickel molybdenum steels See Nickel chromium molybdenum steels		Production of Nd—Fe—B Alloy Powders Using High- Pressure Gas Atomization and Their Hard Magnetic Prop-	
Chromium nickel steels		erties.	5-11A
See Nickel chromium steels Chromium steels See also Austenitic stainless steels		Coercive force, Microstructural effects The Effect of Microstructure on Properties and Behaviors of Annealed Fe ₇₈ B ₁₃ Si ₉ Amorphous Alloy Ribbon.	63-70A
Chromium molybdenum steels Chromium molybdenum vanadium steels		Coercivity See Coercive force	
Ferritic stainless steels Martensitic stainless steels		Cold cracking (welds)	
Nickel chromium molybdenum steels Nickel chromium steels		See Weld defects Cold deformation	
Stainless steels		See Deformation	

Cold ductility See Ductility		Constitutional diagrams See Phase diagrams	
Cold formability See Formability		Consumption See Energy consumption	
Cold forming See Cold working		Contact testing	
Cold reduction		See Ultrasonic testing Contaminating	
See Cold working Cold rolling		See Contamination Contamination	
Modeling Recrystallization Kinetics in a Deformed Iron Single Crystal.	391-401A	Grain-Boundary Contamination and Ductility Loss in Boron- Doped Ni ₃ AI.	2017-2023A
Shear Band Formation in Heavily Cold Rolled 70-30 Brass. Recrystallization Microstructure in Cold-Rolled Aluminum Composites Reinforced by Silicon Carbide Whiskers.	1267-1275A 1743-1753A	Continuous casting Two-Dimensional Model for Twin-Roll Continuous Casting.	381-390B
Composites Reinforced by Silicon Carbide Whiskers. Graphite Formation in High-Purity Cold-Rolled Carbon Steels.	1917-1925A	Fluid Flow and Bath Temperature Destratification in Gas- Stirred Ladles. Effect of Thermal Conditions and Alloying Constituents	603-611B
Cold stretching See Stretching		(Ni,Cr) on Macrosegregation in Continuously Cast High- Carbon (0.8%), Low-Alloy Steel.	893-910B
Cold working See also Cold rolling		Continuous casting, Field effects Electromagnetic Refining of Aluminum Alloys by the CREM	
Stretch forming An X-Ray Diffraction Line Profile Analysis in Cold-Worked Hexagonal (β)-Phase and Mixed ($\alpha + \beta$)-Phase of Copper—Germanium Alloys.	1142-1144A	Process. I. Working Principle and Metallurgical Results. Electromagnetic Refining of Aluminum Alloys by the CREM Process. II. Specific Practical Problems and Their Solutions.	623-629B 631-643B
Columbium See Niobium		Continuous furnaces Analytical Models for the Gas Carburizing Process.	535-546B
Columbium base alloys		Continuous reheat furnaces	000 0 100
See Niobium base alloys Columbium compounds		See Continuous furnaces Control	
See Niobium compounds Combustion chambers		See Process control Temperature control	
Mathematical Modeling of an Aluminum Casting Furnace Combustion Chamber.	421-429B	Controllability See Stability	
Compacting See Explosive compacting		Controlled atmospheres Kinetics of Deoxidation of Liquid Copper by Graphite Parti-	
Hot isostatic pressing Compacts		cles During Submerged Injection. Dependence of the Lattice Parameter of γ' Iron Nitride,	187-196B
See Powder compacts Sintered compacts		Fe ₄ N _{1—x} , on Nitrogen Content; Accuracy of the Nitrogen Absorption Data. Oxidation and Nitridation of Alloy 800 H at a Growing Creep	1533-1539A
Compatibility See Biocompatibility		Crack and for Unstressed Samples. Investigations on the Influence of Internal Nitridation on	1541-1551A
Compliance (elasticity) See Modulus of elasticity		Creep Crack Growth in Alloy 800H. Thermomechanical Fatigue, Oxidation, and Creep. I. Damage Mechanisms.	1553-1560A 1755-1767A
Composite materials		Thermomechanical Fatigue, Oxidation, and Creep. I. Life Pre- diction.	1769-1783A
See also Fiber composites Particulate composites Whisker composites		Controlled rolling Effect of Deformation on Ferrite Nucleation and Growth in a	
Composite materials, Casting Structure of As-Cast Aluminum Matrix Composite Containing Ni ₃ Al-Type Intermetallic Ribbons.	1153-1161A	Plain Carbon and Two Microalloyed Steels. Convection Thermosolutal Convection During Dendritic Solidification of	987-998A
Compositions Equilibrium Surface Composition of Ternary Alloys.	215-223A	Alloys. II. Nonlinear Convection. Converters	883-891B
Compressing Experimental Deformation Textures of OFE Copper and		See Bottom blown converters Cooling	
70:30 Brass From Wire Drawing, Compression, and Torsion.	125-131A	See Supercooling	
Influence of Precipitates on the Mechanical Response and Substructure Evolution of Shock-Loaded and Quasi- Statically Deformed AI—LI—Cu Alloys.	1061-1075A	Cooling rate The Electrical Conductivity of Cast Al—Si Alloys in the Range 2-12.6 wt.% Silicon.	383-389A
Compression	1001-1075A	The Effect of Microstructure of Ferritic Spheroidal Graphite Cast Irons on Intergranular Fracture at Intermediate Terri-	
See Compressing Compression casting		peratures. The Microstructures of Strip-Cast Low-Carbon Steels and	431-436A
See Pressure casting Compressive modulus		Their Response to Thermal Processing. The Microstructural Details of β -Sn Precipitation in a 5Sn— ORDER Solder Allow	1191-1198A 1325-1333A
See Modulus of elasticity		95Pb Solder Alloy. Microstructural Development During Solidification of Stainless Steel Alloys.	2117-2131A
Computer programs Analytical Models for the Gas Carburizing Process.	535-546B	Solidification of High-Speed Tool Steels. Microstructure and Corrosion Behavior of As-Cast and Heat-	2133-2148A
Computer simulation A Mathematical Model of the Spray Deposition Process.	71-85A	Treated AI—4.5 wt.% Cu—2.0 wt.% Mn Alloys. Copper, Alloying elements	2499-2516A
Three-Dimensional Transient Model for Arc Welding Process. Computer Simulation of Solid Solution Strengthening in FCC Alloys. I. Friedel and Mott Limits.	645-659B 1411-1418A	Effect of Copper on the Strength of AISI 316 Stainless Steel. Copper. Binary systems	421-429A
Computer Simulation of Solid Solution Strengthening in FCC Alloys. II. At Absolute Zero Temperature.	1419-1428A	Freezing Diagrams. I. Development and Implications for Glass Formability.	287-297A
Computer Simulation of Thermally Activated Dislocation Mo- tion. III. In FCC Solid Solutions.	1429-1437A	Freezing Diagrams. II. Comparison With Experimental Observation and Relevance to Crystallization of Metallic Glass.	299-309A
Growth Dynamics Study of the Martensitic Transformation in Fe—30Ni Alloys. II. Computer Simulation of Martensitic Growth. Roll Cooling and its Relationship to Roll Life.		Copper, Crystal lattices A Comparison of Ultrasonic and X-Ray Determinations of Texture in Thin Copper and Aluminum Plates.	2431-2447A
Simulation of Static and Deformation-Enhanced Grain Growth Effects on Superplastic Ductility.		Copper, Diffusion Two-Dimensional Finite Difference Analysis of Shape Instabilities in Plates.	1385-1394A
See Continuous casting		Copper, Extraction	
Concentration cell corrosion See Pitting (corrosion)		Mathematical Modeling of Minor-Element Behavior in Flash Smelting of Copper Concentrates and Flash Converting of Copper Mattes.	39-51B
Conducting sheet analog See Heat transmission		Reaction Mechanism in a Copper Flash Smelting Furnace. A Mineralogical Study of the Deportment and Reaction of Sil-	327-336B
Conductivity See Resistivity		ver During Copper Electrorefining. Physico-Chemical Properties of Copper Electrolytes.	345-361B 375-380B
Conductivity (electrical)		The Leaching of Sintered CuS Disks With Ferric Chlorides. Kinetic Study of the Dissolution of Cuprite in Oxyacid Solu-	485-491B 573-580B
See Resistivity		tions.	373-300B

Microbiological Leaching of Copper From Lead Mattes.	773-779B	On Crack Closure of Precipitation Hardened Steels in Aque-	1055-1059A
Fluid Flow in Pachuca (Air-Agitated) Tanks. I. Laboratory- Scale Experimental Measurements. Development of a Mathematical Model for Multihearth Roast-	781-791B	ous Solution. Fatigue Crack Growth Behavior of Pressure Vessel Steels and Submerged Arc Weldments in a High-Temperature	
ers.	925-935B	Pressurized Water Environment.	2069-2085A
Copper, Forming Effects of Changes in Strain Path on Work Hardening in Cubic Metals.	2471-2482A	Corrosion mechanisms Oxidation and Nitridation of Alloy 800 H at a Growing Creep Crack and for Unstressed Samples.	1541-1551A
Copper, Irradiation Irradiation-Enhanced and -Induced Mass Transport. In Situ Studies of Ion Irradiation Effects in an Electron Micro-	2619-2626A	Corrosion potential Microstructure and Corrosion Behavior of As-Cast and Heat- Treated AI—4.5 wt.% Cu—2.0 wt.% Mn Alloys.	2499-2516A
scope.	2673-2680A	Corrosion products	400 5404
Copper, Mechanical properties Gas Phase Embrittlement by Metal Vapors. Latent Hardening in Cyclic Deformation of Copper Single	184-188A	Transient Oxidation of Single-Crystal β-NiAl. Mass Spectrometric Observations of Metal Oxychlorides Produced by Oxidation—Chlorination Reactions.	499-518A 1566-1568A
Crystals. Fatigue Crack Growth and Fracture Behavior of Bismuth- Doped Copper Bicrystals.	759-767A 1221-1231A	Corrosion rate, Cooling effects Microstructure and Corrosion Behavior of As-Cast and Heat- Treated AI—4.5 wt.% Cu—2.0 wt.% Mn Alloys.	2499-2516A
Copper, Metal working Experimental Deformation Textures of OFE Copper and 70:30 Brass From Wire Drawing, Compression, and Tor-		Corrosion resistance On Crack Closure of Precipitation Hardened Steels in Aque-	
sion. Copper, Nondestructive testing	125-131A	ous Solution. Mass Spectrometric Observations of Metal Oxychlorides Produced by Oxidation—Chlorination Reactions.	1055-1059A 1566-1568A
New Ultrasonic Methods for Measuring Deformation and Fracture Related Material States. Copper, Refining	611-618A	Corrosion resistance, Coating effects The Effects of Silicon on the Reaction Between Solid Iron and Liquid 55 wt.% AI—Zn Bath.	543-555A
Kinetics of Deoxidation of Liquid Copper by Graphite Parti- cles During Submerged Injection.	187-196B	Corrosion resistance, Heating effects The Effects of Heat Treatment on the Chromium Depletion,	343-333A
Copper, Structural hardening Dislocation Structures of Monocrystalline Copper in Cyclic Latent Hardening.	2033-2045A	Precipitation Evolution, and Corrosion Resistance of Inco- nel Alloy 690. Retrogression and Reaging and the Role of Dislocations in	2057-2067A
The Role of Grain Size and Strain in Work Hardening and Texture Development.	2803-2810A	the Stress Corrosion of 7000-Type Aluminum Alloys. CO2 arc welding	2087-2092A
Copper, Ternary systems The Thermodynamic Activities of Copper and Iron in the System Copper—Iron—Platinum at 1300°C.	127-135B	See Gas metal arc welding Crack closure	
Copper, Welding Contacting Surfaces: a Problem in Fatigue and Diffusion		Effects of Near-Tip Inhomogeneities on Scattering of Ultra- sonic Waves by Cracks. On Crack Closure of Precipitation Hardened Steels in Aque-	619-626A
Bonding. Copper base alloys See also Brasses	627-636A	ous Solution. Crack closure, Heating effects The Influence of Temperature on Small Fatigue.	1055-1059A
Copper base alloys, Irradiation Reaction Rate Theory Perspectives on Some Problems in		The Influence of Tempering Temperature on Small Fatigue Crack Behavior Monitored With Surface Acoustic Waves in Quenched and Tempered 4140 Steel.	1257-1265A
Materials Science. Mechanical Property Changes in Ion-Irradiated Metals. I.	2583-2598A	Crack growth See Crack propagation	
Ni—Cu Alloys. Mechanical Property Changes in Ion-Irradiated Metals. II.	2681-2687A	Crack initiation Quantitative Characterization of Microcracking in A533B	
High-Strength Cu—Ni—Be Alloy. Copper base alloys, Mechanical properties	2689-2693A	Steel by Acoustic Emission. Grain Egression: a New Mechanism of Fatigue-Crack Initia-	1105-1114A
Simulation of Static and Deformation-Enhanced Grain Growth Effects on Superplastic Ductility.	2783-2792A	tion in Ti—6AI—4V. An Investigation on the Mechanism of 475°C Embrittlement in	1715-1725A 2563-2567A
Copper base alloys, Microstructure X-Ray Diffraction Line Profile Analysis on the Microstructure of Cold-Worked Face-Centered Cubic Cu—Ge—Si Alloys: Effects of Dilute Solutes Silicon and Germanium.	1883-1885A	High-Chromium Ferritic Stainless Steel. Crack initiation, Corrosion effects Microstructural Trapping Effects on Hydrogen Induced Cracking of a Microalloyed Steel.	909-919A
Copper base alloys, Phase transformations Phase Stability by the Artificial Concentration Wave Method. Correction to "Microstructural Refinement of W—Ni—Fe	357-362A	A Research on Hydrogen Cracking in α-Iron. Crack initiation, Microstructural effects Effects of Microstructure on Fatigue Crack Initiation and	2379-2384A
Heavy Alloys by Alloying Additions*. Copper base alloys, Reactions (chemical)	3100-3103A	Propagation of 16Mn Steel. The Effect of Cyclic Loading on the Dislocation Structure of	413-419A
Activities of Boron in the Binary Fe—B, Co—B, and Cu—B Melts. Direct Activity Measurements in Liquid Ag—Cu Alloys Using	705-710B	Fully Pearlitic Steel. Crack opening displacement Crack Bridging by Uncracked Ligaments During Fatigue-	447-451A
a Valved Knudsen Cell—Mass Spectrometer System. Copper base alloys, X ray analysis	845-852B	Crack Growth in SiC-Reinforced Aluminum-Alloy Compos- ites.	897-908A
An X-Ray Diffraction Line Profile Analysis in Cold-Worked Hexagonal (β)-Phase and Mixed ($\alpha + \beta$)-Phase of Copper—Germanium Alloys.	1142-1144A	Micromechanics and Fatigue Crack Growth in an Alumina- Fiber-Reinforced Magnesium Alloy Composite. Crack opening displacement, Alloying effects	2369-2378A
Copper compounds, Phases (state of matter) Phase Structure of the Ti ₁ Cu _{1—x} Fe _x System.	981-985A	A Comparison of the Fracture Behavior of Two Heats of the Secondary Hardening Steel AF1410.	105-123A
Copper mattes, Refining Vacuum Distillation of Copper Matte to Remove Lead, Arse-		Crack opening displacement, Corrosion effects Mode I Stress Intensity Factors Induced by Fracture Surface Roughness Under Pure Mode III Loading: Application to the	
nic, Bismuth, and Antimony. Core hardness See Hardness	793-804B	Effect of Loading Modes on Stress Corrosion Crack Growth.	1989-1999A
Corrodents See Corrosion environments		Crack propagation Evidence of a Thin Sheet Toughening Mechanism in Al— Fe—X Alloys.	155-164A
Corrosion		New Ultrasonic Methods for Measuring Deformation and Fracture Related Material States.	611-618A
See also Corrosion fatigue Corrosion mechanisms		Acoustic Emission From Intergranular Subcritical Crack Growth.	637-648A
Pitting (corrosion) A Study of the Thermodynamics and Phase Relationships of the Fe—Co—S—O Quaternary System.	1523-1532A	Study of the Interface and Its Effect on Mechanical Properties of Continuous Graphite Fiber-Reinforced 201 Aluminum. Crack Bridging by Uncracked Ligaments During Fatigue-	727-739A
Corrosion cracking See Stress corrosion cracking		Crack Growth in SiC-Reinforced Aluminum-Alloy Composites.	897-908A
Corrosion effects		Fracture and Fatigue Crack Propagation in a Nickel-Base Me- tallic Glass.	1395-1409A
See Pitting (corrosion) Corrosion environments		Oxidation and Nitridation of Alloy 800 H at a Growing Creep Crack and for Unstressed Samples.	1541-1551A
On Crack Closure of Precipitation Hardened Steels in Aqueous Solution.	1055-1059A	Investigations on the Influence of Internal Nitridation on Creep Crack Growth in Alloy 800H. The Effects of Hold Time and Frequency on Crack Growth in	1553-1560A
Corrosion fatigue The Influence of Water Vapor on the Fatigue Crack Propaga-		Alloy 800H at 650°C.	1727-1734A
tion Kinetics in Pure Aluminum Single Crystals.	925-933A	Thermomechanical Fatigue, Oxidation, and Creep. I. Life Pre- diction.	1769-1783A

Fracture and Fatigue Crack Propagation Properties of Har-		Crevices	
dened 52100 Steel. Micromechanics and Fatigue Crack Growth in an Alumina-	1961-1973A	See Cracks Cross slip	
Fiber-Reinforced Magnesium Alloy Composite. Mechanism of Cyclic Softening and Fracture of a Nickel-Base γ '-Strengthened Alloy Under Low-Cycle Fatigue.	2369-2378A 2793-2801A	Theory of Work-Hardening Applied to Stages III and IV. On the Mechanism of Cross Slip in Ni ₃ Al.	2393-2397A 2811-2818A
Crack propagation, Alloying effects Observations on the Faceted Fatigue Fracture of Cast Co—	2700 20017	Cross tension test See Tension tests	
Cr—Mo Alloy Used for Surgical Implants. Crack propagation, Corrosion effects	99-103A	Crystal defects See also Dislocation loops	
The Role of Crack Tip Strain Rate in the Stress Corrosion Cracking of High Strength Steels in Water.	889-895A	Dislocations Interstitial impurities Point defects	
The Influence of Hydrogen on Atomic Binding Energy, Critical Slip Shear Stress, and Fatigue Crack Propagation Rate of Attractors Single Constallation	001 0044	Screw dislocations Stacking faults Nonbasal Plane Defects in 18R Martensite and the Effect of	
Aluminum Single Crystals. The Influence of Water Vapor on the Fatigue Crack Propaga-	921-924A 925-933A	Abnormal Defects on Thermoelastic Martensitic Transfor-	
tion Kinetics in Pure Aluminum Single Crystals. Application of Modeling of the Texture Dependence of Envi- ronmentally Assisted Crack Growth of Long and Short	920-933A	mation. Crystal defects, Radiation effects	1631-1636A
Gracks to Zircaloy Fuel Tubing. Mode I Stress Intensity Factors Induced by Fracture Surface	1943-1950A	Irradiation-Enhanced and -Induced Mass Transport. Crystal growth	2619-2626A
Roughness Under Pure Mode III Loading: Application to the Effect of Loading Modes on Stress Corrosion Crack Growth.	1989-1999A	Diamond Growth in O ₂ + C ₂ H ₄ and O ₂ + C ₂ H ₂ Flames. Crystal growth, Field effects	1282-1284A
Fatigue Crack Growth Behavior of Pressure Vessel Steels and Submerged Arc Weldments in a High-Temperature Pressurized Water Environment.	2069-2085A	The Effect of Ultrahigh Magnetic Fields on Dopant Distribu- tion in CZ Systems: a Modeling Study and Comparison With Asymptotic Solutions.	1637-1646A
Crack propagation, Heating effects		Crystal lattices	
The Influence of Tempering Temperature on Small Fatigue Crack Behavior Monitored With Surface Acoustic Waves in Quenched and Tempered 4140 Steel.	1257-1265A	See Face centered cubic lattice Crystal orientation	
Crack propagation, High temperature effects	1207 12007	See Crystal structure Crystal structure	
Near-Threshold Fatigue Crack Growth Properties at Elevated Temperature for 1Cr—1Mo—0.25V Steel and 12Cr Stain- less Steel.	741-749A	See also Equiaxed structure Quasicrystalline structure	
Crack propagation, impurity effects	141-1400	Unit cell Phase Transformations in the Al—Li—Hf and Al—Li—Ti	
Fatigue Crack Growth and Fracture Behavior of Bismuth- Doped Copper Bicrystals.	1221-1231A	Systems. Microstructure of High-Tensile Strength Brasses Containing Silicon and Manganese.	999-1019A 1199-1206A
Crack propagation, Microstructural effects Effects of Microstructure on Fatigue Crack Initiation and Propagation of 16Mn Steel.	413-419A	Crystal structure, Alloying effects Microstructure Evolution in TiAl Alloys With Boron Additions: Conventional Solidification.	1847-1859A
Crack propagation, Temperature effects Fatigue Crack Propagation in Rapidly Solidified Aluminum Alloys at 25°C and 300°C.	2425-2430A	Crystallinity See Crystal structure	1047-100011
Crack resistance	2423-243UA	Crystallization	
See Crack propagation Cracking (fracturing) See also Crack initiation		See also Recrystallization On Identification of the Nucleant in Commercially Pure Aluminum Castings Inoculated With < 0.15% Titanium.	564-566A
Stress corrosion cracking Thermomechanical Fatigue, Oxidation, and Creep. I. Damage		Structural Study of Electrodeposited Aluminum—Manganese Alloys. Faceted—Nonfaceted Dendritic Transitions During the Laser	1351-1359A
Mechanisms. Cracking (fracturing), Corrosion effects	1755-1767A	Processing of Al ₂ O ₃ —1.0 wt.% MgO.	2191-2194A
Microstructural Trapping Effects on Hydrogen Induced Cracking of a Microalloyed Steel.	909-919A	Crystallography Crystallography of Directionally Solidified Magnesium Alloy AZ91.	847-852A
A Research on Hydrogen Cracking in α-Iron. Cracks	2379-2384A	The SCC of Single Crystals of β Brass in Water: Fractography and Crystallography.	1439-1444A
Contacting Surfaces: a Problem in Fatigue and Diffusion Bonding.	627-636A	Atom Probe Field-Ion Microscope: a Technique for Microstructural Characterization of Irradiated Materials on the Atomic Scale.	2651-2661A
Cratering (wear) See Wear		Analytical Electron Microscopy Studies of Radiation Damage. Crystals	2663-2671A
Cratering (welding) See Weld defects		See Single crystals Cubic lattice	
Creep (materials) See also Creep rate		See Face centered cubic lattice	
Creep rupture strength New Ultrasonic Methods for Measuring Deformation and		Production of Nd—Fe—B Alloy Powders Using High-	
Fracture Related Material States. Effect of Oxygen on Tungsten Filament Sag Kinetics.	611-618A 1144-1146A	Pressure Gas Atomization and Their Hard Magnetic Properties.	5-11A
Correlation of Microstructure and Creep Stages in the (100) Oriented Superalloy SRR99 at 1253K. Oxidation and Nitridation of Alloy 800 H at a Growing Creep	1233-1238A	Curie temperature, Microstructural effects The Effect of Microstructure on Properties and Behaviors of	00.704
Crack and for Unstressed Samples. Investigations on the Influence of Internal Nitridation on	1541-1551A	Annealed Fe ₇₈ B ₁₃ Si ₉ Amorphous Alloy Ribbon. Curves	63-70A
Creep Crack Growth in Alloy 800H. The Effects of Hold Time and Frequency on Crack Growth in	1553-1560A	See Stress strain curves TTT curves	
Alloy 800H at 650°C. Thermomechanical Fatigue, Oxidation, and Creep. I. Life Pre-	1727-1734A	Cutting tool materials, Coating A TEM Study of CVD TIC _x /Ti(C, N) _x Coating on WC—Co Ce-	
diction. Deformation of Whisker-Reinforced Metal-Matrix Composites Under Changing Temperature Conditions.	1769-1783A 2355-2368A	mented Carbide. Cutting tools, Casting	279-285B
A Creep Technique for Monitoring MnS Precipitation in Sill- con Steels.	2707-2715A	Solidification of High-Speed Tool Steels.	2133-2148A
Creep limit See Creep (materials)		Cutting tools, Materials selection Preparation of Submicron Titanium Nitride Powder by Vapor- Phase Reactions.	493-497B
Creep properties See Creep (materials)		Cycles See Thermal cycling	
Creep rate, Microstructural effects		Cyclical heating	
Influence of Precipitate Morphology on Intermediate Temper- ature Creep Properties of a Nickel-Base Superalloy Single	133-141A	See Thermal cycling Czochralski process	
Crystal. Creep rupture strength, Impurity effects		See Crystal growth	
Effects of Manganese, Silicon, and Purity on the Design of 3.5NiCrMoV, 1CrMoV, and 2.25Cr—1Mo Bainitic Alloy Steels.	2197-2212A	See also Radiation damage Thermomechanical Fatigue, Oxidation, and Creep. I. Damage Mechanisms.	1755-1767A
Creeping See Creep (materials)		Thermomechanical Fatigue, Oxidation, and Creep. I. Life Pre- diction.	1769-1783A

Data storage Mechanical Properties of Thin Films.	2217-2245A	Morphology of Nonmetallic Inclusions Using Silicon, Alumi- num, and Calcium—Silicon Alloy in Steel Melt.	581-594B
Decarbonizing		Dephosphorizing	
Decarburization Kinetics of Liquid Fe—C _{sat} Alloys by CO ₂ . Decarburizing	853-861B	Thermodynamics of the Na ₂ O—P ₂ O ₅ System. Determination of the Standard Gibbs Energies of Formation	197-204B
Nonuniformity of NaOH Concentration and Effective Bubble Diameter in CO ₂ Injection Into Aqueous NaOH Solution.	5-12B	of Ba ₃ P ₂ and Ba ₃ (PO ₄) ₂ . Deposition	871-877B
Decomposition		See Hot dip coating Immersion coating	
See Eutectoid decomposition Phase decomposition		Silver plating	
Spinodal decomposition		Vapor deposition Depth profiling	
Deep carburizing See Carburizing Defects		A Mathematical Model Describing Carburization in Multielement Alloy Systems.	1021-1028A
See also Crystal defects		Description The Kingting of Nitrogen Absorption and Description From a	
Dislocation loops Dislocations		The Kinetics of Nitrogen Absorption and Desorption From a Plasma Arc by Molten Iron.	175-185B
Interstitial impurities Point defects		Desulfurizing The Sulfur Partition Ratio With Fe—C _{SAT} Melts and the Sul-	
Screw dislocations . Stacking faults		fide Capacity of CaO—SiO ₂ —Na ₂ O—(Al ₂ O ₃) Slags.	71-76B
Weld defects Involvement of Processing Defects in Failure of FP/AI—Li.	2175-2179A	Coal Desulfurization With Aqueous Chlorine. Diagrams	567-571B
Defects, Radiation effects		See Phase diagrams	
Impurity-Defect Interactions in Radiation Hardening and Em- brittlement in BCC Metals. In Situ Studies of Ion Irradiation Effects in an Electron Micro-	2637-2649A	Diamond pyramid hardness Mechanical Properties of High-Temperature Beryllium Inter-	1279-1282A
scope.	2673-2680A	metallic Compounds. Diamonds, Synthesis	12/9-1282A
See Formability		Diamond Growth in O ₂ + C ₂ H ₄ and O ₂ + C ₂ H ₂ Flames.	1282-1284A
Deformation		Diffraction See X ray diffraction	
See also Plastic deformation Prestraining		Diffusion	
An Analysis of the Low Temperature, Low and High Strain- Rate Deformation of Ti—6AI—4V.	863-874A	High Temperature Reaction Zone Growth in Tungsten Fiber Reinforced Superalloy Composites. I. Application of the	
Deformation of Rapidly Solidified Dispersion Strengthened Titanium Alloys.	875-887A	Moving Boundary Equations.	255-266A
Deforming	0/3-00/A	High Temperature Reaction Zone Growth in Tungsten Fiber Reinforced Superalloy Composites. II. Matrix Chemistry Ef-	
See Deformation		fects. Determination of the Diffusion Coefficients of NiCl ₂ , ZnCl ₂ ,	267-272A
Degradation Degradation of Mechanical Properties of Cr—Mo—V and		and CdCl ₂ in Aqueous Solution. Nucleation Kinetics of Titanium Carbonitride in Microalloyed	555-565B
2.25Cr—1Mo Steel Components After Long-Term Service at Elevated Temperatures.	87-97A	Austenite. A Small-Angle Neutron Scattering Study of the Kinetics of	689-697A
Delaminating Cryogenic Toughness of Commercial Aluminum—Lithium Al-		Phase Separation in a Supersaturated Ni—12.5 at.% Si Alloy.	699-710A
loys: Role of Delamination Toughening.	485-497A	Two-Dimensional Finite Difference Analysis of Shape Insta- bilities in Plates.	1385-1394A
See Dendritic structure		In Situ Observations of Chemically Induced Grain-Boundary Migration and Discontinuous Precipitation in the	
Dendritic structure Thermosolutal Convection During Dendritic Solidification of		Aluminum—Zinc System. A Mass Transport Theory for Interphase Precipitation With	1593-1600A
Alloys. II. Nonlinear Convection.	883-891B	Application to Vanadium Steels. Correction to "A Mass Transport Theory for Interphase Pre-	1647-1655A
Primary Dendrite Spacing and the Effect of Off-Axis Heat Flow.	969-973A	cipitation With Application to Vanadium Steels".	1647-1655A
The Microstructures of Strip-Cast Low-Carbon Steels and Their Response to Thermal Processing.	1191-1198A	Kinetics of Layer Growth and Multiphase Diffusion in Ion- Nitrided Titanium.	1819-1832A
Side Branch Morphology and Coarsening in Directionally So- lidified Pb—8.4 at.% Au.	1889-1893A	Study of the Mechanism of Fast Diffusion of Cobalt in Tho- rium by Diffusion and Internal Friction Measurements.	2289-2297A
Faceted—Nonfaceted Dendritic Transitions During the Laser Processing of Al ₂ O ₃ —1.0 wt.% MgO.	2191-2194A	Interdiffusion in Ternary Fe—Cr—Al Alloys.	2767-2781A
Processing of Al ₂ O ₃ —1.0 wt.% MgO. Dendritic Growth in the Carbon Tetrabromide and Hexachlor- ethane System.	2567-2570A	Diffusion, Alloying effects The Effect of Chromium on Antimony and Nickel Grain	
Dendritic structure, Composition effects		Boundary Segregation in Iron. Diffusion, Cooling effects	2170-2171A
The influence of Carbon Content on Austenite—Ferrite Morphology in Fe—Mn—Al Weld Metals.	2559-2561A	Efficient Estimation of Diffusion During Dendritic Solidification.	2847-2856A
Dendritic structure, Cooling effects The Growth of Tubular or Vermicular Structures in Organic		Diffusion, High temperature effects	
Monotectic Systems. On the Influence of Coarsening on Microsegregation.	171-177A 247-253A	Interdiffusion Coefficients in the Zeta Phase of the Fe—Al System.	2561-2563A
Modeling of Equiaxed Microstructure Formation in Casting. Thermosolutal Convection During Dendritic Solidification of	311-322A	Diffusion, Radiation effects	0500 00074
Alloys. I. Linear Stability Analysis. The Columnar-to-Equiaxed Transition in Al—3Cu.	711-721B	Fluctuations in Composition in Dilute Alloys Under Irradiation. Irradiation-Enhanced and -Induced Mass Transport.	2599-2607A 2619-2626A
Solidification Microstructures Near the Limit of Absolute Sta-	731-734B	Diffusion bonding	
bility. Solidification of High-Speed Tool Steels.	769-777A 2133-2148A	See Diffusion welding Diffusion coatings	
A Statistically Significant Experimental Technique for Investi- gating Microsegregation in Cast Alloys.	2529-2533A	Intermetallic Compound Layer Growth at the Interface of Solid Refractory Metals Molybdenum and Niobium With	
Efficient Estimation of Diffusion During Dendritic Solidifica- tion.	2847-2856A	Molten Aluminum.	825-836A
Dendritic structure, Field effects		Diffusion coefficient See Diffusion	
Mixed Gravity Mode Grwoth During Directional Dendritic So- lidification Aboard the KC-135.	1284-1286A	Diffusion couples	
Densification Microstructural Change During Liquid Phase Sintering of		See Diffusion	
W—Ni—Fe Alloy.	837-845A	Contacting Surfaces: a Problem in Fatigue and Diffusion	
Density Mechanical Properties of High-Temperature Beryllium Inter-		Bonding. Intermetallic Compound Layer Growth at the Interface of	627-636A
metallic Compounds.	1279-1282A	Solid Refractory Metals Molybdenum and Niobium With Molten Aluminum.	825-836A
Deoxidation See Deoxidizing		Diffusivity	
Deoxidizers		Isothermal Particle Growth in Two-Phase Titanium Alloys. Diffusivities and Viscosities of Some Gases at Elevated Tem-	39-54A
Morphology of Nonmetallic Inclusions Using Silicon, Alumi- num, and Calcium—Silicon Alloy in Steel Melt.	581-594B	peratures: Gas Diffusivities in Porous Solids. On the Diffusion of Carbon in Titanium Carbide.	141-148B 403-411A
Deoxidizing Kinetics of Deoxidation of Liquid Copper by Graphite Particles During Submerged Injection.	187-196B	Diffusivity, Composition effects The Effect of Composition on Marker Movement and Kirken- dall Porosity in Ternary Alloys.	2299-2303A

Dimensions See Particle size		Dispersoids See Dispersions	
Thickness Dioxides		Displacements (lattice) See Interstitial impurities	
See Carbon dioxide		Dissimilar metals, Joining	
Dip coating See Immersion coating Directional solidification		Intermetallic Compound Layer Growth at the Interface of Solid Refractory Metals Molybdenum and Niobium With Molten Aluminum.	825-836A
Solidification Microstructures Near the Limit of Absolute Sta- bility.	769-777A	Dissociated ammonia brazing See Brazing	
Crystallography of Directionally Solidified Magnesium Alloy AZ91.	847-852A	Dissociation	
Thermosolutal Convection During Dendritic Solidification of Alloys. II. Nonlinear Convection.	883-891B	Upgrading Ferrochromium to Chromium by Nitriding, Leaching, and Dissociation.	219-226B
Fluid Flow in Solidifying Monotectic Alloys. Dendritic Growth in the Carbon Tetrabromide and Hexachlor- ethane System.	2517-2527A 2567-2570A	Dissociation energy See Free energy of formation	
Efficient Estimation of Diffusion During Dendritic Solidifica- tion.	2847-2856A	Dissolution Kinetic Study of the Dissolution of Cuprite in Oxyacid Solu-	
Directional solidification, Field effects Mixed Gravity Mode Grwoth During Directional Dendritic So- lidification Aboard the KC-135.	1284-1286A	tions. Dissolution of Reactive Strontium-Containing Alloys in Liquid Aluminum and A356 Melts.	573-580B 815-831B
Discontinuous precipitates See Cellular precipitates		Dissolving See Dissolution	
Dislocation climb See Dislocation mobility		Drawing See Wire drawing	
Dislocation density		Drawing (heat treatment)	
Influence of Precipitates on the Mechanical Response and Substructure Evolution of Shock-Loaded and Quasi- Statically Deformed Al—Li—Cu Alloys.	1061-1075A	See Tempering Drill steels	
Dislocation density, Alloying effects	1001 10707	See Tool steels	
X-Ray Diffraction Line Profile Analysis on the Microstructure of Cold-Worked Face-Centered Cubic Cu—Ge—Si Alloys:	1000 10051	Ductile brittle transition Hydrogen Embrittlement of Iron—Nickel Alloys.	1475-1482A
Effects of Dilute Solutes Silicon and Germanium. Dislocation density, Deformation effects	1883-1885A	Ductile iron See Nodular iron	
An X-Ray Diffraction Line Profile Analysis in Cold-Worked Hexagonal (ζ)-Phase and Mixed (α + ζ)-Phase of		Ductility	
Copper—Germanium Alloys.	1142-1144A	The Effect of Void Shape on Void Growth and Ductility in Ax- isymmetric Tension Tests.	853-861A
Dislocation density, Radiation effects Mechanical Property Changes in Ion-Irradiated Metals. I. Ni—Cu Alloys.	2681-2687A	Martensite Formation, Strain Rate Sensitivity, and Deforma- tion Behavior of Type 304 Stainless Steel Sheet. Particle Bonding, Annealing Response, and Mechanical	1239-1246A
Dislocation loops	2001-2007A	Properties of Dynamically Consolidated Type 304 Stainless Steel Powders.	2449-2457A
Influence of Precipitates on the Mechanical Response and Substructure Evolution of Shock-Loaded and Quasi- Statically Deformed Al—Li—Cu Alloys.	1061-1075A	Simulation of Static and Deformation-Enhanced Grain Growth Effects on Superplastic Ductility.	2783-2792A
Dislocation loops, Radiation effects	1001-1073A	Ductility, Alloying effects Combined Effects of Oxygen and Hydrogen on Tensile Prop-	
Mechanical Property Changes in Ion-Irradiated Metals. I. Ni—Cu Alloys.	2681-2687A	erties of a Nb10 at.% V Alloy. The Effect of Molybdenum Addition on Properties of Iron Al-	273-278A
Dislocation mobility Computer Simulation of Thermally Activated Dislocation Mo-		uminides. Phase Transformations in the Al—Li—Hf and Al—Li—Ti	751-757A
tion. III. In FCC Solid Solutions. Cleavage Fracture in Pearlitic Eutectoid Steel. Fatigue Crack Propagation in Rapidly Solidified Aluminum Al-	1429-1437A 2321-2335A	Systems. Microstructure and Tensile Properties of Fe—40 at.% Al Alloys With C, Zr, Hf, and B Additions.	999-1019A 1701-1714A
loys at 25°C and 300°C.	2425-2430A	Improved Ductility of Ni ₃ Si by Microalloying With Boron or Carbon.	2025-2032A
Dislocation mobility, Stress effects Determination of Effective Stress and Dislocation Velocity in the Deformation of Titanium-Doped Iron.	1029-1036A	Ductility, Deformation effects Graphite Formation in High-Purity Cold-Rolled Carbon Steels.	1917-1925A
Dislocations See also Dislocation loops		Ductility, Heating effects	1011-10201
Screw dislocations Influence of Precipitate Morphology on Intermediate Temper- ature Creep Properties of a Nickel-Base Superalloy Single		Grain-Boundary Contamination and Ductility Loss in Boron- Doped NigAl.	2017-2023A
Crystal. The Effect of Cyclic Loading on the Dislocation Structure of	133-141A	Ductility, Impurity effects Effects of Manganese, Silicon, and Purity on the Design of	
Fully Pearlitic Steel. The Effect of Small Plastic Deformation and Annealing on the	447-451A	 Steels. 	2197-2212A
Properties of Polycrystals. I. Experimental Observations. The Effect of Small Plastic Deformation and Annealing on the	471-477A	Ductility, Pressure effects Effects of Microstructure on the Behavior of an Aluminum	
Properties of Polycrystals. II. Theoretical Model for the Transformation of Nonequilibrium Grain Boundaries.	479-484A	Alloy and an Aluminum Matrix Composite Tested Under Low Levels of Superimposed Hydrostatic Pressure.	2409-2417A
Phase Transformations in the Al—Li—Hf and Al—Li—Ti Systems.	999-1019A	Ductility, Radiation effects	
Computer Simulation of Solid Solution Strengthening in FCC Alloys. II. At Absolute Zero Temperature. Theory of Work Handeling Applied to Storge III and IV	1419-1428A 2393-2397A	Impurity-Defect Interactions in Radiation Hardening and Em- brittlement in BCC Metals.	2637-2649A
Theory of Work-Hardening Applied to Stages III and IV. On the Mechanism of Cross Silp in Ni ₃ AI.	2811-2818A	Dynamics See Kinetics	
Dislocations, Alloying effects Effect of Copper on the Strength of AISI 316 Stainless Steel. Dislocations, Deformation effects	421-429A	Dysprosium base alloys, Phases (state of matter) Physical Metallurgy of Metastable BCC Lanthanide— Magnesium Alloys for R = Lanthanum, Gadolinium and	
Dislocation Structures of Monocrystalline Copper in Cyclic Latant Hardening.	2033-2045A	Dysprosium. Eddy current gage	1575-1583A
Dislocations, Heating effects Retrogression and Reaging and the Role of Dislocations in		See Eddy current testing Eddy current testing	
the Stress Corrosion of 7000-Type Aluminum Alloys.	2087-2092A	Eddy Current Analysis of Precipitation Kinetics in Aluminum Alloys.	605-610A
Dispersion hardening alloys, Composite materials Recrystallization Microstructure in Cold-Rolled Aluminum Composites Reinforced by Silicon Carbide Whiskers.	1743-1753A	Elastic constants See also Elastic limit	
Dispersion hardening alloys, Corrosion Hydrogen Trapping in Thoria-Dispersed Nickel.	2483-2488A	Modulus of elasticity The Effects of Elastic Stress on the Kinetics of Ostwald Ri-	
Dispersion hardening alloys, Mechanical properties Deformation of Rapidly solidified Dispersion Strengthened Titanium Alloys.	875-887A	pening: the Two-Particle Problem. Elastic limit, Composition effects Elastic Limits and Microplastic Response in Ultrahigh	1175-1189A
Dispersions Microstructure Evolution in TiAl Alloys With Boron Additions:		Strength Carbon Steels. Elastic modulus	188-191A
Conventional Solidification.	1847-1859A	See Modulus of elasticity	

Elastic properties See Elastic constants		Electroreduction See Electrowinning	
Elasticity Mechanical Properties of Thin Films.	2217-2245A	Electrorefining Physico-Chemical Properties of Copper Electrolytes.	375-380B
Electric arc welding See Arc welding		Determination of the Diffusion Coefficients of NiCl ₂ , ZnCl ₂ , and CdCl ₂ in Aqueous Solution.	555-565B
Electric essemblies See Electric devices		Electrowinning A Mineralogical Study of the Deportment and Reaction of Silver During Copper Electrorefining.	345-361B
Electric circuits		Physico-Chemical Properties of Copper Electrolytes. Determination of the Diffusion Coefficients of NiCl ₂ , ZnCl ₂ ,	375-380B
See Integrated circuits Electric components		and CdCl ₂ in Aqueous Solution. Activities in the Liquid System NaF—MgF ₂ —AlF ₃ .	555-565B 671-674B
See Electric devices Electric devices		The Effect of Additives on Activities in Cryolite Melts. Elementary particles	675-677B
Diamond Growth in O ₂ + C ₂ H ₄ and O ₂ + C ₂ H ₂ Flames.	1282-1284A	See Antiparticles Elongation, Impurity effects	
Electric devices, Soldering The Microstructural Details of β-Sn Precipitation in a 5Sn— 95Pb Solder Alloy.	1325-1333A	Gas Phase Embrittlement by Metal Vapors.	184-188A
Electric welding See Arc welding Electron beam welding	1020	Elongation, Microstructural effects Effect of Phosphorus on the Formation of Retained Austenite and Mechanical Properties in Silicon-Containing Low- Carbon Steel Sheet.	437-445A
Flux core wire welding Gas metal arc welding		Emanation See Emission	
Gas tungsten arc welding Shielded metal arc welding		Embrittlement See also Hydrogen embrittlement	
Submerged arc welding Electrical conductivity		Liquid metal embrittlement An Investigation on the Mechanism of 475°C Embrittlement in	
See Resistivity Electrical phenomena		High-Chromium Ferritic Stainless Steel. Embrittlement, Heating effects	2563-2567A
See Electrode potentials		Grain-Boundary Contamination and Ductility Loss in Boron- Doped Ni ₃ Al.	2017-2023A
See Resistivity		Embrittlement, Impurity effects Gas Phase Embrittlement by Metal Vapors.	184-188A
See Resistivity		Embrittlement, Microstructural effects	104 1001
Electrical steels, Metal working A Creep Technique for Monitoring MnS Precipitation in Silicon Steels.	2707-2715A	The Effect of Microstructure of Ferritic Spheroidal Graphite Cast Irons on Intergranular Fracture at intermediate Tem- peratures. The Influences of Impurity Content, Tensile Strength, and	431-436A
Electrochemistry Electrode Mass Transfer Under Conditions of Natural and		Grain Size on In-Service Temper Embrittlement of CrMoV Steels.	2345-2354A
Forced Convection. Electrocoatings	21-29B	Emission See also Acoustic emission	
See Electroplates		Emission Spectroscopy of Plasma During Laser Welding of AISI 201 Stainless Steel.	277-286B
See also Corrosion potential Activities of Boron in the Binary Fe—B, Co—B, and Cu—B Melts.	705-710B	Endurance limit See Fatigue limit	
Electrogas welding	703-7100	Energy See Activation energy Binding energy	
See Gas metal arc welding Electroless plating		Free energy Free energy of formation	
See Immersion coating Electrolysis		Surface energy Energy consumption	
See Electrowinning Reduction (electrolytic)		Physico-Chemical Properties of Copper Electrolytes.	375-380B
Electrolytic cells Chemical Potentials of Oxygen for Fayalite—Quartz—Iron		Energy of activation See Activation energy	
and Fayalite—Quartz—Magnetite Equilibria. Thermodynamic Stability of Potassium β-Alumina.	679-685B 687-691B	See Free energy of formation	
Electrolytic reduction See Reduction (electrolytic)		Energy of formation See Free energy of formation	
Electromagnetic fields		Energy of fracture See Toughness	
Electromagnetic Refining of Aluminum Alloys by the CREM Process. I. Working Principle and Metallurgical Results.	623-629B	Energy storage	
Electromagnetic Refining of Aluminum Alloys by the CREM Process. II. Specific Practical Problems and Their Solu- tions.	631-643B	See Hydrogen storage Engines (types), Brazing	
Electromagnetic stirring		The Interaction of Reaction-Bonded Silicon Carbide and Inco- nel 600 With a Nickel-Based Brazing Alloy.	1803-1810A
Modeling of Multidimensional Solidification of an Alloy. Electromotive force series	1833-1845A	Standard Enthalpy of Formation of Sc ₅ Si ₃ .	879-882B
See Electrode potentials Electromotive series		Environment See Corrosion environments	
See Electrode potentials Electron beam welding		Space environment Equiaxed structure	
Development of Microstructures in Fe—15Ni—15Cr Single Crystal Electron Beam Welds.	1125-1138A	Electromagnetic Refining of Aluminum Alloys by the CREM Process. I. Working Principle and Metallurgical Results. Equiaxed structure, Cooling effects	623-629B
See also Scanning electron microscopy Crystallography of Directionally Solidified Magnesium Alloy A291.		Modeling of Equiaxed Microstructure Formation in Casting.	311-322A
Analytical Electron Microscopy Studies of Radiation Damage. Determination of Carbide and Matrix Compositions in High-	847-852A 2663-2671A	Equilibrium Equilibrium Partition Coefficients in Iron-Based Alloys. Equilibrium Surface Composition of Ternary Alloys.	149-160B 215-223A
Speed Steels by Analytical Electron Microscopy. Electronic assemblies	2695-2701A	Equilibrium diagrams See Phase diagrams	
See Electric devices		Eutectics, Cooling effects Solidification of High-Speed Tool Steels.	2133-2148A
See Electric devices		Inconel 718: a Solidification Diagram. Eutectics, Crystal growth	2149-2158A
See Electric devices		Discussion of "The Mechanism of Silicon Modification in Aluminum—Silicon Alloys: Impurity-Induced Twinning".	1286-1290A
Electropiates, Microstructure Structural Study of Electrodeposited Aluminum—Manganese Alloys.	1351-1359A	Eutectics, Mechanical properties Cavitation Behavior of an Al—Cu Eutectic Alloy During Superplastic Deformation.	453-462A

Eutectics, Microstructure The Electrical Conductivity of Cast Al—Si Alloys in the Range 2-12.6 wt.% Silicon.	383-389A	Fatigue Crack Growth Behavior of Pressure Vessel Steels and Submerged Arc Weldments in a High-Temperature Pressurized Water Environment.	2069-2085A
Eutectoid composition Physical Metallurgy of Metastable BCC Lanthanide— Magnesium Alloys for R = Lanthanum, Gadolinium and Dysprosium.	1575-1583A	Fatigue failure, Heating effects The Influence of Tempering Temperature on Small Fatigue Crack Behavior Monitored With Surface Acoustic Waves in Quenched and Tempered 4140 Steel.	1257-1265A
Eutectoid decomposition Some Phase-Diagram Aspects of the Manganese—Carbon System.	747-754B	Fatigue failure, High temperature effects Near-Threshold Fatigue Crack Growth Properties at Elevated Temperature for 1Cr—1Mo—0.25V Steel and 12Cr Stain-	
Eutectoid reactions See Eutectoid decomposition		less Steel. Fatigue failure, Impurity effects	741-749A
Expansion See Thermal expansion		Fatigue Crack Growth and Fracture Behavior of Bismuth- Doped Copper Bicrystals.	1221-1231A
Explosive compacting		Fatigue failure, Microstructural effects	
Particle Bonding, Annealing Response, and Mechanical Properties of Dynamically Consolidated Type 304 Stainless Steel Powders.	2449-2457A	The Effect of Cyclic Loading on the Dislocation Structure of Fully Pearlitic Steel. Involvement of Processing Defects in Failure of FP/AI—Li.	447-451A 2175-2179A
Microstructures and Mechanical Properties of Explosively Consolidated Titanium Powder With a Pressure Medium. Extraction	2831-2839A	Fatigue failure, Temperature effects Fatigue Crack Propagation in Rapidly Solidified Aluminum Al- loys at 25°C and 300°C.	2425-2430A
See also Carbon in pulp process Physical Characteristics of Gas Jets Injected Vertically Up- ward Into Liquid Metal.	595-601B	Fatigue fracture See Fatigue failure	
A Study of the Thermodynamics and Phase Relationships of the Fe-Co-S-O Quaternary System.	1523-1532A	Fatigue life	
Extractive metallurgy See also Hydrometallurgy	1020 1002/1	Thermomechanical Fatigue, Oxidation, and Creep. I. Damage Mechanisms.	1755-1767A
The Selective Oxidation of Mixed Metal Sulfides With Lime in		Thermomechanical Fatigue, Oxidation, and Creep. I. Life Pre- diction.	1769-1783A
the Presence of Steam Without Emitting Sulfur-Containing Pollutants. The Extractive Metallurgist in an Emerging World of Materi-	237-242B	Fatigue life, Microstructural effects Effects of Microstructure on Fatigue Crack Initiation and	413-419A
als.	291-313B	Propagation of 16Mn Steel. Fatigue limit, Microstructural effects	413-419A
Extrusion Workability of 1045 Spheroidized Steel Under Superimposed Hydrostatic Pressure.	1735-1741A	The Effect of Cyclic Loading on the Dislocation Structure of Fully Pearlitic Steel.	447-451A
Extrusion casting See Pressure casting		Fatigue properties See Fatigue (materials)	
Extrusion See Extrusion		FCC metals, Structural hardening Computer Simulation of Solid Solution Strengthening in FCC	
Fabrication		Alloys. I. Friedel and Mott Limits. Computer Simulation of Solid Solution Strengthening in FCC	1411-1418A
Calculation of Minimum Pressure for Liquid Metal Infiltration of a Fiber Array. Involvement of Processing Defects in Failure of FP/AI—Li.	1861-1866A 2175-2179A	Alloys, II. At Absolute Zero Temperature. Computer Simulation of Thermally Activated Dislocation Motion. III. In FCC Solid Solutions.	1419-1428A 1429-1437A
Face centered cubic lattice Structural Study of Electrodeposited Aluminum—Manganese		Ferric compounds See Iron compounds	
Alloys. Face centered cubic metals	1351-1359A	Ferrite, Alloying effects The Microstructure of Chromium—Tungsten Steels.	373-382A
See FCC metals		Ferritic stainless steels, Mechanical properties	3/3-3024
Fallure analysis See also Fractography The Development of Plastic Failure Modes in Crystalline Ma-		An Investigation on the Mechanism of 475°C Embrittlement in High-Chromium Ferritic Stainless Steel.	2563-2567A
terials: Shear Bands in FCC Polycrystals. Fast nuclear reactors	579-593A	Ferrous alloys See also Cast iron Steels	
On Microstructure—Property Correlation of Thermally Aged Type 316L Stainless Steel Weld Metal.	1115-1124A	Ferrous alloys, Casting	149-160B
Fatigue (materials) See also Corrosion fatigue		Equilibrium Partition Coefficients in Iron-Based Alloys. Ferrous alloys, Coatings	149-1000
Fatigue life Fatigue limit		Particle Melting in High Temperature Supersonic Low Pres- sure Plasma Jets.	251-262B
Low cycle fatigue Roll Cooling and Its Relationship to Roll Life.	2305-2320A	Ferrous alloys, Composite materials High Temperature Reaction Zone Growth in Tungsten Fiber	
Fatigue cracking See Fatigue (materials)		Reinforced Superalloy Composites. I. Application of the Moving Boundary Equations. High Temperature Reaction Zone Growth in Tungsten Fiber	255-266A
Fatigue failure New Ultrasonic Methods for Measuring Deformation and		Reinforced Superalloy Composites. II. Matrix Chemistry Effects.	267-272A
Fracture Related Material States. Effects of Near-Tip Inhomogeneities on Scattering of Ultra-	611-618A	Ferrous alloys, Corrosion	
sonic Waves by Cracks. Contacting Surfaces: a Problem in Fatigue and Diffusion.	619-626A	Hydrogen Embrittlement of Iron—Nickel Alloys. Oxidation and Nitridation of Alloy 800 H at a Growing Creep	1475-1482A
Bonding. Study of the Interface and Its Effect on Mechanical Properties	627-636A	Crack and for Unstressed Samples. Investigations on the Influence of Internal Nitridation on	1541-1551A
of Continuous Graphite Fiber-Reinforced 201 Aluminum. Crack Bridging by Uncracked Ligaments During Fatigue- Crack Growth in SiC-Reinforced Aluminum-Alloy Compos-	727-739A	Creep Crack Growth in Alloy 800H. Ferrous alloys, Diffusion	1553-1560A
ites. On Crack Closure of Precipitation Hardened Steels in Aque-	897-908A	The Effect of Chromium on Antimony and Nickel Grain Boundary Segregation in Iron.	2170-2171A
ous Solution. Fracture and Fatigue Crack Propagation in a Nickel-Base Me-	1055-1059A	Ferrous alloys, Irradiation Ordering in the Fe-Ni System Under Electron Irradiation.	711-718A
tallic Glass. Grain Egression: a New Mechanism of Fatigue-Crack Initia-	1395-1409A	Reaction Rate Theory Perspectives on Some Problems in Materials Science.	2583-2598A
tion in Ti—6AI—4V. The Effects of Hold Time and Frequency on Crack Growth in	1715-1725A	Ferrous alloys, Mechanical properties	2000 20001
Alloy 800H at 650°C. Fracture and Fatigue Crack Propagation Properties of Har-	1727-1734A	The Effect of Microstructure on Properties and Behaviors of	63-70A
dened 52100 Steel. Micromechanics and Fatigue Crack Growth in an Alumina-	1961-1973A	Annealed Fe ₇₈ B ₁₉ Si ₉ Amorphous Alloy Ribbon. The Effects of Hold Time and Frequency on Crack Growth in Alloy 800H at 650°C.	1727-1734A
Fiber-Reinforced Magnesium Alloy Composite. Mechanism of Cyclic Softening and Fracture of a Nickel-Base γ'-Strengthened Alloy Under Low-Cycle Fatigue.	2369-2378A 2793-2801A	Ferrous alloys, Nondestructive testing Acoustic Emission From Intergranular Subcritical Crack	007 0464
Fatigue failure, Alloving effects		Growth. Ferrous alloys, Phase transformations	637-648A
Observations on the Faceted Fatigue Fracture of Cast Co— Cr—Mo Alloy Used for Surgical Implants.	99-103A	The Influence of Annealing in the Ferrite-Plus-Austenite Phase Field on the Stability of Vanadium Carbide Precipi-	237-245A
Fatigue failure, Corrosion effects The Influence of Hydrogen on Atomic Binding Energy, Critical		Growth Dynamics Study of the Martensitic Transformation in	231-243A
Slip Shear Stress, and Fatigue Crack Propagation Rate of Aluminum Single Crystals.	921-924A	Fe—30Ni Alloys. I. Quantitative Measurements of Growth Velocity.	1601-1615A

Growth Dynamics Study of the Martensitic Transformation in		Reaction Mechanism in a Copper Flash Smelting Furnace.	327-336B
Fe—30Ni Alloys. II. Computer Simulation of Martensitic Growth.	1617-1629A	Flaw detection See Eddy current testing	
Production of Nd—Fe—B Alloy Powders Using High-		Ultrasonic testing	
Pressure Gas Atomization and Their Hard Magnetic Prop- erties.	5-11A	Flaws See Defects	
Ferrous alloys, Reactions (chemical)		Flexural vibration	
Activities of Boron in the Binary Fe—B, Co—B, and Cu—B Melts.	705-710B	See Fatigue (materials)	
Studies of the Interfacial Kinetics of the Reaction of CO ₂ With Liquid Iron—Nickel Alloys at 1873K.	755-756B	Floating zone melting See Zone melting	
Ferrous alloys, Welding Development of Microstructures in Fe—15Ni—15Cr Single	755-7508	Floating zone refining See Zone melting	
Crystal Electron Beam Welds. The Influence of Carbon Content on Austenite—Ferrite Mor-	1125-1138A	Flow See Fluid flow	
phology in Fe—Mn—Al Weld Metals.	2559-2561A	Gas flow	
Ferrous compounds See Iron compounds		Plastic flow Flow stress	
Ferrous metals		See Yield strength	
See Ferrous alloys		Fluid flow See also Gas flow	
Fiber composites, Casting Calculation of Minimum Pressure for Liquid Metal Infiltration of a Fiber Array.	1861-1866A	Mathematical Modeling of an Aluminum Casting Furnace Combustion Chamber.	421-429B
Microstructural Observations of Pressure Cast Ni ₃ Al/Al ₂ O ₃ and Ni/Al ₂ O ₃ Composites.	2159-2166A	Fluid Flow and Bath Temperature Destratification in Gas- Stirred Ladles.	603-611B
and Ni/Al ₂ O ₃ Composites. Infiltration of Fibrous Preforms by a Pure Metal. I. Theory. Infiltration of Fibrous Preforms by a Pure Metal. II. Experi-	2535-2547A	Flow Separation and Liquid Rundown in a Gas-Atomization Process.	613-622B
ment.	2549-2557A	Electromagnetic Refining of Aluminum Alloys by the CREM Process. II. Specific Practical Problems and Their Solu-	
Fiber composites, Diffusion High Temperature Reaction Zone Growth in Tungsten Fiber		tions.	631-643B
Reinforced Superalloy Composites. I. Application of the		Three-Dimensional Transient Model for Arc Welding Process. Fluid Flow in Pachuca (Air-Agitated) Tanks. I. Laboratory-	645-659B
Moving Boundary Equations. High Temperature Reaction Zone Growth in Tungsten Fiber	255-266A	Scale Experimental Measurements. Effects of Particle Loading on a Reduced Pressure Induc-	781-791B
Reinforced Superalloy Composites. II. Matrix Chemistry Effects.	267-272A	tively Coupled Radio Frequency Plasma Torch. On Effective Viscosity Models for Gas-Stirred Ladle Systems.	949-958B 967-969B
Fiber composites, Fabrication		The Effects of Elastic Stress on the Kinetics of Ostwald Ri-	
Effects of Particle Loading on a Reduced Pressure Induc- tively Coupled Radio Frequency Plasma Torch.	949-958B	pening: the Two-Particle Problem. Fluid Flow in Solidifying Monotectic Alloys.	1175-1189A 2517-2527A
Fiber composites, Mechanical properties		Infiltration of Fibrous Preforms by a Pure Metal. I. Theory. Infiltration of Fibrous Preforms by a Pure Metal. II. Experi-	2535-2547A
Study of the Interface and Its Effect on Mechanical Properties of Continuous Graphite Fiber-Reinforced 201 Aluminum.	727-739A	ment.	2549-2557A
Involvement of Processing Defects in Failure of FP/AI—Li. Micromechanics and Fatigue Crack Growth in an Alumina-	2175-2179A	Fluidity See Viscosity	
Fiber-Reinforced Magnesium Alloy Composite.	2369-2378A	Fluidized beds	
Characteristics of Hot-Pressed Fiber-Reinforced Ceramics With SiC Matrix.	2419-2423A	Modeling of Fluidized Bed Chlorination of Rutile.	959-966B
Fiber composites, Reactions (chemical) Interface Characterization of Fiber-Reinforced Ni ₃ Al Matrix		Fluids See Gases	
Composites.	2459-2469A	Flux core wire welding	
Fiber metal brazing See Brazing		Mechanisms of Inclusion Formation in Al—Ti—Si—Mn De- oxidized Steel Weld Metals.	1335-1349A
Fibers		Fluxing	
See Carbon fibers		Re-Evaluation of Standard Free Energy of Formation of CaO. Determination of the Standard Gibbs Energies of Formation	431-433B
Field ion microscopy Atom Probe Field-Ion Microscope: a Technique for		of Ca ₃ As ₂ , Ca ₃ Sb ₂ , and Ca ₃ Bi ₂ . Determination of the Standard Gibbs Energies of Formation	863-870B
Microstructural Characterization of Irradiated Materials on the Atomic Scale.	2651-2661A	of Ba ₃ P ₂ and Ba ₃ (PO ₄) ₂ .	871-877B
Fields (physics)	2031-2001A	Foaming Study on the Foaming of CaO—SiO ₂ —FeO Slags. I. Foaming	
See Electromagnetic fields Magnetic fields		Parameters and Experimental Results.	509-514B
Filaments, Crystal growth		Study on the Foaming of CaO—SiO ₂ —FeO Slags. II. Dimensional Analysis and Foaming in Iron and Steelmaking Pro-	
An Elastic Recovery Test for Recrystallization.	1885-1887A	Cesses.	515-521B
Filaments, Mechanical properties Effect of Oxygen on Tungsten Filament Sag Kinetics.	1144-1146A	Foil (metal), Phase transformations Phase Stability by the Artificial Concentration Wave Method.	357-362A
Filaments, Microstructure		Foil brazing	
On the Formation of Potassium Bubbles in Tungsten Rod.	179-184A	See Brazing Force	
Filler metal, Alloy development Tin-Based Reactive Solders for Ceramic/Metal Joints.	919-924B	See Coercive force Shock loading	
Films See Thin films		Forging	
Finite element method		Workability of 1045 Spheroidized Steel Under Superimposed Hydrostatic Pressure.	1735-1741A
Modeling of Equiaxed Microstructure Formation in Casting. The Development of Plastic Failure Modes in Crystalline Ma-	311-322A	Formability	1/35-1/41A
terials: Shear Bands in FCC Polycrystals.	579-593A	Calculation of the Forming Limit Diagram. Characterization of Formability in Cold-Rolled Steel Sheets	1975-1987A
The Effect of Void Shape on Void Growth and Ductility in Ax- isymmetric Tension Tests.	853-861A	Using Electromagnetic Acoustic Transducers.	2385-2392A
Prediction of Weld Pool and Reinforcement Dimensions of GMA Welds Using a Finite-Element Model. Elastic Interaction Stresses. II. The Influence of Orientation	937-947B	A Comparison of Ultrasonic and X-Ray Determinations of Texture in Thin Copper and Aluminum Plates.	2431-2447A
on Stresses Generated in Iso-Axial Bicrystals.	1461-1473A	Forming	
Experimental Investigation and Finite Element Modeling of Hemispherically Stretched Steel Sheet.		See Cold rolling Controlled rolling	
Fireboxes	1509-1521A	Extrusion Forging	
See Combustion chambers		Hot isostatic pressing Hot rolling	
Fission reactors See Nuclear reactors		Rolling	
Fisaures		Stretch forming Stretching	
See Cracks		Thermomechanical treatment Wire drawing	
Diamond Growth in O ₂ + C ₂ H ₄ and O ₂ + C ₂ H ₂ Fiames.	1282-1284A	Fossil fuels	
Flash smelting Mathematical Modeling of Minor-Element Rehavior in Flash		See Coal	
Mathematical Modeling of Minor-Element Behavior in Flash Smelting of Copper Concentrates and Flash Converting of Copper Mattes.	39-51B	Foundry practice Dissolution of Reactive Strontium-Containing Alloys in Liquid Aluminum and A356 Melts.	815-831B

Fractography		Friction	
Possible NDE Correlation With Fractography in 4340 Steel. The SCC of Single Crystals of β Brass in Water: Fractography	323A	Shear Band Formation in Heavily Cold Rolled 70-30 Brass. Experimental Investigation and Finite Element Modeling of	1267-1275A
and Crystallography. Effect of Tellurium on Morphological Transitions in Fe—C—	1439-1444A	Hemispherically Stretched Steel Sheet. Determination of Friction Coefficient for Sheet Materials	1509-1521A
Si Alloys. II. Auger Analysis.	1875-1881A	Under Stretch-Forming Conditions.	2179-2182A
Effects of Microstructure on the Behavior of an Aluminum Alloy and an Aluminum Matrix Composite Tested Under Low Levels of Superimposed Hydrostatic Pressure.	2409-2417A	Friction, Composition effects Friction Properties of Al—1.5Mg/SiC Particulate Metal-Matrix Composites.	1501 15001
Stereo (Scanning Electron Microscopy) Section Fractography of Isolated Cleavage Regions in Nuclear Vessel Steels.	2862-2866A	Fuel injection	1564-1566A
Fracture mechanics	LUGE EUGGA	Steel Dissolution in Quiescent and Gas Stirred Fe/C Melts.	363-374B
See also Crack opening displacement Crack Bridging by Uncracked Ligaments During Fatigue-		Fuels	
Crack Growth in SiC-Reinforced Aluminum-Alloy Compos-		See Coal Fuming (slag)	
ites. Investigations on the Influence of Internal Nitridation on	897-908A	See Slag fuming	
Creep Crack Growth in Alloy 800H. The Effects of Hold Time and Frequency on Crack Growth in	1553-1560A	Furnaces	
Alloy 800H at 650°C.	1727-1734A	See Bottom blown converters Continuous furnaces	
Fracture and Fatigue Crack Propagation Properties of Har- dened 52100 Steel.	1961-1973A	Hearth roasters Kilns	
Micromechanics and Fatigue Crack Growth in an Alumina- Fiber-Reinforced Magnesium Alloy Composite.	2369-2378A	Fuselages	M.
Effects of Microstructure on the Behavior of an Aluminum	2000 207 071	See Airframes	
Alloy and an Aluminum Matrix Composite Tested Under Low Levels of Superimposed Hydrostatic Pressure.	2409-2417A	Fusion welding See Arc welding	
Discussion of "Correlations of Microstructure With Dynamic and Quasi-Static Fracture in a Plain Carbon Steel".	2860-2862A	Electron beam welding	
Fracture strength, Microstructural effects		Flux core wire welding Gas metal arc welding	
The Effect of Microstructure on Properties and Behaviors of Annealed Fe ₇₈ B ₁₃ Si ₉ Amorphous Alloy Ribbon.	63-70A	Gas tungsten arc welding Laser beam welding	
Fracture testing	00 707	Shielded metal arc welding Submerged arc welding	
Quantitative Characterization of Microcracking in A533B Steel by Acoustic Emission.	1105-1114A	Gadolinium base alloys, Phases (state of matter)	
Fracture toughness	1103-1114A	Physical Metallurgy of Metastable BCC Lanthanide— Magnesium Alloys for R = Lanthanum, Gadolinium and	
Evidence of a Thin Sheet Toughening Mechanism in Al-	455 4544	Dysprosium.	1575-1583A
Fe—X Alloys. Characteristics of Hot-Pressed Fiber-Reinforced Ceramics	155-164A	Galvanic cells	
With SiC Matrix.	2419-2423A	See Electrolytic cells Celvenized steels Forming	
Fracture toughness, Alloying effects A Comparison of the Fracture Behavior of Two Heats of the		Galvanized steels, Forming Experimental Investigation and Finite Element Modeling of	
Secondary Hardening Steel AF1410.	105-123A	Hemispherically Stretched Steel Sheet.	1509-1521A
Fracture toughness, Cryogenic effects Cryogenic Toughness of Commercial Aluminum—Lithium Al-		Galvannealing See Annealing	
loys: Role of Delamination Toughening.	485-497A	Gas	
Fracture toughness, Heating effects The Effects of Surface Hardening on Fracture Toughness of		See Gases	
Carburized Steel.	519-525A	Gas flow Influence of Gas Flow on Performance of "Confined" Atom-	
Duplex Treatment of High-Strength Steels.	1687-1699A	ization Nozzles.	833-843B
Fracture toughness, Microstructural effects Correlation of Microstructure and Tempered Martensite Embrittlement in Two 4340 Steels.	1089-1103A	Gas metal arc welding Mechanisms of Inclusion Formation in Al—Ti—Si—Mn De- oxidized Steel Weld Metals.	1335-1349A
Fracture toughness, Pressure effects Microvoid Formation During Shear Deformation of Ultrahigh		Gas metal arc welding, Automation Prediction of Weld Pool and Reinforcement Dimensions of	
Strength Steels.	143-153A	GMA Welds Using a Finite-Element Model.	937-947B
Fracture toughness, Size effects Confirmation of a Thin Sheet Toughening Mechanism and		Gas permeability See Permeability	
Anisotropic Fracture in Al—Fe—X Alloys.	2337-2344A	Gas tungsten arc welding	
Fracture toughness, Temperature effects Discussion of "Correlations of Microstructure With Dynamic and Quasi-Static Fracture in a Plain Carbon Steel".	2860-2862A	On Microstructure—Property Correlation of Thermally Aged Type 316L Stainless Steel Weld Metal. Inconel 718: a Solidification Diagram.	1115-1124A 2149-2158A
Fracturing		Gases	
See also Brittle fracture Intergranular fracture		Physical Characteristics of Gas Jets Injected Vertically Up- ward Into Liquid Metal.	595-601B
Transgranular fracture Confirmation of a Thin Sheet Toughening Mechanism and		Gearing	
Anisotropic Fracture in Al—Fe—X Alloys.	2337-2344A	See Gears	
Fracturing, Alloying effects Observations on the Faceted Fatigue Fracture of Cast Co—		Gears, Heat treatment Analytical Models for the Gas Carburizing Process.	535-546B
Cr—Mo Alloy Used for Surgical Implants. Microstructure and Tensile Properties of Fe—40 at.% Al Al-	99-103A	Germanium, Alloying elements	
loys With C, Zr, Hf, and B Additions.	1701-1714A	X-Ray Diffraction Line Profile Analysis on the Microstructure of Cold-Worked Face-Centered Cubic Cu—Ge—Si Alloys:	
Fracturing, Microstructural effects	0004 00054	Effects of Dilute Solutes Silicon and Germanium.	1883-1885A
Cleavage Fracture in Pearlitic Eutectoid Steel. Frames	2321-2335A	Germanium, Binary systems Mass Spectrometric Study of the Partial Phase Diagram of	
See Airframes		the Fe—Ge System Above 1050°C.	975-976A
Free energy		Germanium, Ternary systems A Note on the Ag—Au—Ge Equilibrium Phase Diagram.	2167-2170A
See also Activation energy Free energy of formation Thermodynamic Consistency of the Ternary Functions.	2047-2055A	Gibbs free energy See Free energy	
Free energy of activation		Glass	
See Activation energy		See Metallic glasses	
Free energy of dissociation See Free energy of formation		Glass transition temperature Freezing Diagrams. I. Development and Implications for	007 007
Free energy of formation		Glass Formability. Freezing Diagrams. II. Comparison With Experimental Obser-	287-297A
Chemical Potentials of Oxygen for Fayalite—Quartz—Iron and Fayalite—Quartz—Magnetite Equilibria.	679-685B	vation and Relevance to Crystallization of Metallic Glass.	299-309A
Thermodynamic Stability of Potassium β-Alumina. Determination of the Standard Gibbs Energies of Formation	687-691B	Gold, Extraction The Mechanism of Adsorption of Aurocyanide Onto Activated	
of Ca ₃ As ₂ , Ca ₃ Sb ₂ , and Ca ₃ Bi ₂ .	863-870B	Carbon. Correction to "The Mechanism of Adsorption of Aurocyanide	315-325B
of Ba ₃ P ₂ and Ba ₃ (PO ₄) ₂ . Standard Gibbs Energies of Formation of the Carbides of Chromium by FMF Measurements.	871-877B	Onto Activated Carbon*.	315-325B
Standard Gibbs Energies of Formation of the Carbides of Chromium by EMF Measurements.	911-917B	Fluid Flow in Pachuca (Air-Agitated) Tanks. I. Laboratory- Scale Experimental Measurements.	781-791B

Gold, Ternary systems A Note on the Ag—Au—Ge Equilibrium Phase Diagram.	2167-2170A	Grain structure Effects of Second-Phase Particles on Coarsening of Austen-	
GP zone See Guinier Preston zone		ite in 0.15% Carbon Steels. On the Formation of Potassium Bubbles in Tungsten Rod. Microstructure of High-Tensile Strength Brasses Containing	13-16A 179-184A
Gradients See Temperature gradient		Silicon and Manganese. Grain structure, Alloying effects	1199-1206A
Grain boundaries See also Grain sub boundaries		The Electrical Conductivity of Cast Al—Si Alloys in the Range 2-12.6 wt.% Silicon.	383-389A
On the Formation of Potassium Bubbles in Tungsten Rod. Gas Phase Embrittlement by Metal Vapors. The Effect of Small Plastic Deformation and Annealing on the	179-184A 184-188A	Grain structure, Composition effects The Microstructure of Rapidly Solidified Ti—Fe Melt-Spun	
Properties of Polycrystals. I. Experimental Observations. The Effect of Small Plastic Deformation and Annealing on the	471-477A	Ribbons. Grain structure, Cooling effects The Evolution of Microstructure in the Undercooled Zn—Sn	2841-2845A
Properties of Polycrystals. II. Theoretical Model for the Transformation of Nonequilibrium Grain Boundaries. The Development of Plastic Failure Modes in Crystalline Ma-	479-484A	Entrained Droplets.	2109-2115A
The Development of Plastic Failure Modes in Crystalline Ma- terials: Shear Bands in FCC Polycrystals. Deformation of Rapidly Solidified Dispersion Strengthened Titanium Alloys.	579-593A 875-887A	Grain structure, Welding effects Development of Microstructures in Fe—15Ni—15Cr Single Crystal Electron Beam Welds.	1125-1138A
The Effects of Heat Treatment on the Sensitization and SCC Behavior of Inconel 600 Alloy.	1077-1088A	Grain sub boundaries	
Grain-Boundary Contamination and Ductility Loss in Boron- Doped Ni ₃ Al.	2017-2023A	The Rate Dependence and Microstructure of High-Purity Silver Deformed to Large Strains Between 0.16 and 0.30 T _m .	2001-2010A
Retrogression and Reaging and the Role of Dislocations in the Stress Corrosion of 7000-Type Aluminum Alloys. The Effect of Chromium on Antimony and Nickel Grain	2087-2092A	Graphite, Composite materials Study of the Interface and Its Effect on Mechanical Properties of Continuous Graphite Fiber-Reinforced 201 Aluminum.	727-739A
Boundary Segregation in Iron. Grain boundaries, Heating effects	2170-2171A	Graphitic structure See also Nodular graphitic structure	
Grain boundaries, Heating effects The Microstructure of Selected Annealed Vanadium-Base Alloys. Grain boundary migration	1927-1932A	Graphitic structure, Deformation effects Graphite Formation in High-Purity Cold-Rolled Carbon	1917-1925A
In Situ Observations of Chemically Induced Grain-Boundary Migration and Discontinuous Precipitation in the Aluminum—Zinc System.	1593-1600A	Steels. Graphitization, Deformation effects Graphite Formation in High-Purity Cold-Rolled Carbon	
Grain boundary migration, Deformation effects Microstructural Modeling of Recrystallization in Deformed		Steels. Gray iron	1917-1925A
Iron Single Crystals. Grain growth	1933-1942A	See Nodular iron Greasing	
Calculation of the Product Phase Grain Edge Length and Quadruple Points per Unit Volume During Solid State		See Lubrication	
Transformations. Dendritic Growth in the Carbon Tetrabromide and Hexachlor-	349-355A	Growth See Crystal growth	
ethane System. Grain growth, Deformation effects	2567-2570A	Grain growth Guinier Preston zone	
Modeling Recrystallization Kinetics in a Deformed Iron Single Crystal.	391-401A	Atom-Probe Analysis of GP Zones in an Al—1.7 at.% Cu Alloy.	1585-1591A
Effect of Deformation on Ferrite Nucleation and Growth in a Plain Carbon and Two Microalloyed Steels. Microstructural Modeling of Recrystallization in Deformed	987-998A	Hafnium, Alloying additive Microstructure and Tensile Properties of Fe—40 at.% Al Alloys With C, Zr, Hf, and B Additions.	1701-1714A
Iron Single Crystals. Simulation of Static and Deformation-Enhanced Grain Growth Effects on Superplastic Ductility.	1933-1942A 2783-2792A	Hafnium, Alloying elements Phase Transformations in the AI—Li—Hf and AI—Li—Ti	
Grain growth, Diffusion effects Isothermal Particle Growth in Two-Phase Titanium Alloys.	39-54A	Systems. Laser-Clad Ni ₇₀ Al ₂₀ Cr ₇ Hf ₃ Alloys With Extended Solid Solution of Hafnium. I. Microstructure Evolution.	999-1019A 2267-2277A
Grain growth, Heating effects The Microstructure of Rolled and Annealed Tungsten Rod.	1669-1686A	Laser-Clad Ni ₇₀ Al ₂₀ Cr ₇ H ₇₃ Alloys With Extended Solid Solution of Hafnium. II. Oxidation Behavior.	2489-2497A
Grain growth, Welding effects Weid Thermal Cycles and Precipitation Effects in Ti-V-		Halogenation See Chlorination	
Containing HSLA Steels.	2093-2100A	Hard coating	
Grain orientation Correction to "Microstructural Refinement of W—Ni—Fe Heavy Alloys by Alloying Additions".	3100-3103A	See Hard surfacing Hard facing See Hard surfacing	
Grain refinement On Identification of the Nucleant in Commercially Pure Alumi-		Hard metals	
num Castings Inoculated With < 0.15% Titanium. Electromagnetic Refining of Aluminum Alloys by the CREM	564-566A	See Cemented carbides Hard soldering	
Process. I. Working Principle and Metallurgical Results. Grain refinement, Alloying effects	623-629B	See Brazing Hard surfacing	
Effects of Second-Phase Particles on Coarsening of Austentie in 0.15% Carbon Steels. Correction to "Orientation Dependence of $\beta_1 \rightarrow \beta_1$ Stress-	13-16A	Comparison of the Microstructures and Abrasive Wear Properties of Stellite Hardfacing Alloys Deposited by Arc Welding and Laser Cladding.	1037-1054A
Induced Martensitic Transformation in a Cu—AI—Ni Alloy*. Microstructure and Tensile Properties of Fe—40 at.% Al Alloys With C. 7r. Hr. and B. Additions.	915-923A 1701-1714A	Hardenability, Impurity effects	
loys With C, Zr, Hf, and B Additions. Grain refinement, Deformation effects		Effects of Manganese, Silicon, and Purity on the Design of 3.5NiCrMoV, 1CrMoV, and 2.25Cr—1Mo Bainitic Alloy Steels.	2197-2212A
Effect of Deformation on Ferrite Nucleation and Growth in a Plain Carbon and Two Microalloyed Steels.	987-998A	Hardening	E107-EE1EA
Grain size Modeling of Equiaxed Microstructure Formation in Casting. Calculation of the Product Phase Grain Edge Length and	311-322A	See Carburizing Hard surfacing Ion nitriding	
Quadruple Points per Unit Volume During Solid State Transformations.	349-355A	Nitriding Pack carburizing Precipitation hardening	
Correlation of Microstructure and Tempered Martensite Em- brittlement in Two 4340 Steels. The Microstructure of Strip Coast Low Codes Steels and	1089-1103A	Solution strengthening Strain aging	
The Microstructures of Strip-Cast Low-Carbon Steels and Their Response to Thermal Processing. Cleavage Fracture in Pearlitic Eutectoid Steel.	1191-1198A 2321-2335A	Strain hardening Hardmetais	
The Influences of Impurity Content, Tensile Strength, and Grain Size on In-Service Temper Embrittlement of CrMoV		See Cemented carbides Hardness	
Steels. The Role of Grain Size and Strain in Work Hardening and Texture Development.	2345-2354A 2803-2810A	See also Diamond pyramid hardness Microhardness	
Grain size, Alloying effects The Effect of Molybdenum Addition on Properties of Iron Al-		Mechanical Properties of Thin Films.	2217-2245A
The Effect of Molybdenum Addition on Properties of Iron Al- uminides. Grain size, Heating effects	751-757A	Hardness, Alloying effects Heat Treatment Behavior and Tensile Properties of Cr—W Steels.	463-470A
The Effect of Microstructure of Ferritic Spheroidal Graphite Cast Irons on Intergranular Fracture at Intermediate Tem- peratures.		Hardness, Heating effects The Effects of Surface Hardening on Fracture Toughness of Carburized Steel.	519-525A

The Microstructure of Rolled and Annealed Tungsten Rod.	1669-1686A	High strength low alloy steels, Corrosion	
Hardness, Radiation effects Mechanical Property Changes in Ion-Irradiated Metals. I.		Microstructural Trapping Effects on Hydrogen Induced Cracking of a Microalloyed Steel.	909-919A
Ni—Cu Alloys. Mechanical Property Changes in Ion-Irradiated Metals. II.	2681-2687A	High strength low alloy steels, Structural hardening Characterization of Titanium Carbosulfide Precipitation in Ti-	
High-Strength Cu—Ni—Be Alloy.	2689-2693A	tanium Microalloyed Steels. Analysis of the Temperature Dependence of Strain-	1907-1915A
Hazelett process See Continuous casting		Hardening Behavior in High-Strength Steel.	2819-2829A
Hearth roasters		High strength low alloy steels, Welding Weld Thermal Cycles and Precipitation Effects in Ti—V-	
Development of a Mathematical Model for Multihearth Roasters.	925-935B	Weld Thermal Cycles and Precipitation Effects in Ti—V- Containing HSLA Steels.	2093-2100A
Heat affected zone, Mechanical properties Effects of Microstructure on Fatigue Crack Initiation and		See Hot isostatic pressing	
Propagation of 16Mn Steel.	413-419A	Hot cracking See Cracking (fracturing)	
Heat affected zone, Microstructure Development of Microstructures in Fe—15Ni—15Cr Single Crystal Electron Beam Welds.	1125-1138A	Hot cracking (welds) See Weld defects	
Mechanisms of Inclusion Formation in Al—Ti—Si—Mn De- oxidized Steel Weld Metals.	1335-1349A	Hot deformation	
Weld Thermal Cycles and Precipitation Effects in Ti—V-Containing HSLA Steels.	2093-2100A	See Deformation Hot dip coating	
Heat engines	2093-2100A	The Effects of Silicon on the Reaction Between Solid Iron and Liquid 55 wt.% Al—Zn Bath.	543-555A
See Engines (types)		Intermetallic Compound Layer Growth at the Interface of Solid Refractory Metals Molybdenum and Niobium With	0.0000
Heat flow See Heat transmission		Molten Aluminum.	825-836A
Heat flux		Hot ductility See Ductility	
See Heat transmission Heat measurement		Hot extraction	
See Calorimetry		See Extraction Hot hardness	
Heat resistant alloys See Superalloys		See Hardness	
Heat transfer	74.00	Hot isostatic pressing Phies Transformations at Steel/IN625 Clad Interfaces.	665-681A
A Mathematical Model of the Spray Deposition Process. Mathematical Model of the Stack Region of a Commercial	71-85A	Hot pressing	
Lead Blast Furnace. Two-Dimensional Model for Twin-Roll Continuous Casting.	97-106B 381-390B	See Hot isostatic pressing	
A Heat-Transfer Model for the Rotary Kiln. I. Pilot Kiln Trials. A Heat-Transfer Model for the Rotary Kiln. II. Development of	391-402B	Hot reduction See Hot working	
the Cross-Section Model. Mathematical Modeling of an Aluminum Casting Furnace	403-419B	Hot rolling Development of Rolling Textures in Aluminum Alloy 3004	
Combustion Chamber. Effect of Thermal Conditions and Alloying Constituents	421-429B	Subjected to Varying Hot-Rolling Deformation. The Microstructure of Rolled and Annealed Tungsten Rod.	1495-1507A 1669-1686A
(Ni,Cr) on Macrosegregation in Continuously Cast High- Carbon (0.8%), Low-Alloy Steel.	893-910B	Graphite Formation in High-Purity Cold-Rolled Carbon	1917-1925A
Development of a Mathematical Model for Multihearth Roasters.	925-935B	Steels. Hot roughing	1917-1923A
Effects of Particle Loading on a Reduced Pressure Inductively Coupled Radio Frequency Plasma Torch.	949-958B	See Hot rolling	
Heat Transfer During Nd:YAG Pulsed Laser Welding and Its Effect on Solidification Structure of Austenitic Stainless	343-3300	Hot strength See Tensile strength	
Steels. Roll Cooling and Its Relationship to Roll Life.	957-967A 2305-2320A	Hot stretch forming See Stretch forming	
Infiltration of Fibrous Preforms by a Pure Metal. I. Theory.	2535-2547A	Hot tensile strength	
Infiltration of Fibrous Preforms by a Pure Metal. II. Experi- ment.	2549-2557A	See Tensile strength	
Heat transmission Modeling of Equiaxed Microstructure Formation in Casting.	311-322A	Hot work tool steels, Heat treatment Duplex Treatment of High-Strength Steels.	1687-1699A
Three-Dimensional Transient Model for Arc Welding Process. Primary Dendrite Spacing and the Effect of Off-Axis Heat	645-659B	Hot working See also Hot rolling	
Flow. Heat treatment	909-973A	A Creep Technique for Monitoring MnS Precipitation in Sill- con Steels.	2707-2715A
See Annealing Austenitizing		Hydrogen, Alloying additive	
Carburizing Grain refinement		Combined Effects of Oxygen and Hydrogen on Tensile Properties of a Nb—10 at.% V Alloy.	273-278A
lon nitriding Nitriding		Hydrogen, Diffusion Tribologically-Driven Steady-State Hydrogen Evolution From	
Pack carburizing		Mild Steel by Electrochemical Extraction Technique. Behavior of Sensitized AISI Types 321 and 347 Austenitic	557-580A
Precipitation hardening Quenching and tempering		Stainless Steels in Hydrogen.	2187-2190A
Solution annealing Solution heat treatment		Hydrogen, Impurities Study of the Hydrogen Internal Friction Peak in Nb—10 at.%	
Tempering Vacuum annealing		V in the Presence of Oxygen. Hydrogen Retrapping After Thermal Charging of Hydrogen in	1215-1219A
Heavy metals See Antimony		Iron Single Crystal.	1793-1802A
Bismuth Cadmium		Hydrogen, Solubility The Solubility of Hydrogen in Solid Binary Aluminum—	E00 F000
Lead (metal)		Lithium Alloys. The Solubility of Hydrogen in Molten Aluminum Alloys.	523-533B 1785-1791A
Mercury (metal) Tin		Hydrogen embrittlement Tribologically-Driven Steady-State Hydrogen Evolution From	
Heliarc welding See Gas tungsten arc welding		Mild Steel by Electrochemical Extraction Technique. Microstructural Trapping Effects on Hydrogen Induced	557-560A
Helmholtz free energy		Cracking of a Microalloyed Steel. The Influence of Hydrogen on Atomic Binding Energy, Critical	909-919A
See Free energy High alloy steels		Slip Shear Stress, and Fatigue Crack Propagation Rate of	921-924
Ferritic stainless steels Ferritic stainless steels		Aluminum Single Crystals. The Influence of Water Vapor on the Fatigue Crack Propagation Kinetics in Pure Aluminum Single Crystals.	925-933A
rerruc: stainless steels Maraging steels Martensitic stainless steels		On Crack Closure of Precipitation Hardened Steels in Aque-	
Martensitic stainless steels Stainless steels		ous Solution. Hydrogen Embrittlement of Iron—Nickel Alloys.	1055-1059/ 1475-1482/
High speed tool steels, Casting Solidification of High-Speed Tool Steels.	2133-2148A	Mode I Stress Intensity Factors Induced by Fracture Surface Roughness Under Pure Mode III Loading: Application to the	
High speed tool steels, Metallography		Effect of Loading Modes on Stress Corrosion Crack Growth.	1989-1999
Determination of Carbide and Matrix Compositions in High- Speed Steels by Analytical Electron Microscopy.	2695-2701A	A Research on Hydrogen Cracking in α-Iron. Hydrogen Trapping in Thoria-Dispersed Nickel.	2379-2384A 2483-2488A

Hydrogen potential See Electrode potentials		Physical Characteristics of Gas Jets Injected Vertically Up- ward Into Liquid Metal.	595-601B
Hydrogen storage Phase Structure of the Ti ₁ Cu _{1-x} Fe _X System.	981-985A	Fluid Flow and Bath Temperature Destratification in Gas- Stirred Ladles.	603-611B
Hydrometallurgy		Inoculation On Identification of the Nucleant in Commercially Pure Alumi-	
Nonuniformity of NaOH Concentration and Effective Bubble Diameter in CO ₂ Injection Into Aqueous NaOH Solution.	5-12B	num Castings Inoculated With $< 0.15\%$ Titanium. Correction to "Orientation Dependence of $\beta_1 \rightarrow \beta_1$ Stress-	564-566A
Water and Solute Activities in the Aqueous H ₂ SO ₄ — (NH ₄) ₂ SO ₄ Solutions.	13-20B	Induced Martensitic Transformation in a Cu—Al—Ni Alloy".	915-923A
The Leaching of Galena in Cupric Chloride Media. The Leaching of Sintered CuS Disks With Ferric Chlorides.	475-483B 485-491B	Instability See Stability	
Activities of Water and Solutes in the Solution System H ₂ SO ₄ —Cr ₂ (SO ₄) ₃ —H ₂ O.	763-771B	Integrated circuits Mechanical Properties of Thin Films.	2217-2245A
Hydrostatic pressure		Intensity	
Microvoid Formation During Shear Deformation of Ultrahigh Strength Steels.	143-153A	See Stress intensity Interface reactions	
Workability of 1045 Spheroidized Steel Under Superimposed Hydrostatic Pressure. Effects of Microstructure on the Behavior of an Aluminum Alloy and an Aluminum Matrix Composite Tested Under	1735-1741A	Extended Solid Solution and Nonequilibrium Phase Diagram for Ni—Al Alloy Formed During Laser Cladding. The Effects of Silicon on the Reaction Between Solid Iron and	363-371A
Low Levels of Superimposed Hydrostatic Pressure.	2409-2417A	Liquid 55 wt.% AI—Zn Bath. Study of the Interface and Its Effect on Mechanical Properties	543-555A
Hysteresis Parameters Affecting Sag Resistance in Spring Steels.	1951-1959A	of Continuous Graphite Fiber-Reinforced 201 Aluminum. Intermetallic Compound Layer Growth at the Interface of	727-739A
I beams, Structural hardening The Influence of Copper Precipitation and Plastic Deforma-		Solid Refractory Metals Molybdenum and Niobium With Molten Aluminum.	825-836A
tion Hardening on the Impact-Transition Temperature of Rolled Structural Steels.	1657-1668A	Microstructural Observations of Pressure Cast Ni ₃ Al/Al ₂ O ₃ and Ni/Al ₂ O ₃ Composites. Interface Characterization of Fiber-Reinforced Ni ₃ Al Matrix	2159-2166A
limenite, Reduction (chemical)		Composites.	2459-2469A
The Influence of Weathering on the Reduction of Ilmenite With Carbon.	735-745B	Interface reactions, High temperature effects High Temperature Reaction Zone Growth in Tungsten Fiber	
Immersion coating See also Hot dip coating		Reinforced Superalloy Composites. I. Application of the Moving Boundary Equations.	255-266A
Carbon Fibers Coated With Chromium Carbide Using the Liq- uid Metal Transfer Agent Technique.	165-170A	High Temperature Reaction Zone Growth in Tungsten Fiber Reinforced Superalloy Composites. II. Matrix Chemistry Ef-	
Immersion testing (ultrasonic)		fects.	267-272A
See Ultrasonic testing Impact strength		A TEM Study of CVD TiC _x /Ti(C, N) _x Coating on WC—Co Cemented Carbide.	279-285B
The Influence of Copper Precipitation and Plastic Deforma- tion Hardening on the Impact-Transition Temperature of		Wetting of Ceramic Particulates With Liquid Aluminum Alloys. II. Study of Wettability.	533-541A
Rolled Structural Steels.	1657-1668A	Tin-Based Reactive Solders for Ceramic/Metal Joints. The Effects of Elastic Stress on the Kinetics of Ostwald Ri-	919-924B
Impact strength, Temperature effects Variation of Brittle Fracture With Test Temperature in Tempered Martensitic Structure in 2Si—0.4C Steel.	560-563A	pening: the Two-Particle Problem. The Role of Boundary Conditions in Modeling the Elastic	1175-1189A
Impact toughness	300-303A	Fields Around a Misfitting Precipitate. Two-Dimensional Finite Difference Analysis of Shape Insta-	1277-1279A
See Impact strength Imperfections		bilities in Plates. An Elastically Induced Morphological Instability of a Misfitting	1385-1394A
See Defects		Precipitate. Faceted—Nonfaceted Dendritic Transitions During the Laser	2171-2175A
See Permeability		Processing of Al ₂ O ₃ —1.0 wt.% MgO. Confirmation of a Thin Sheet Toughening Mechanism and	2191-2194A
Impurities See also Interstitial impurities		Anisotropic Fracture in Al—Fe—X Alloys. Hydrogen Trapping in Thoria-Dispersed Nickel.	2337-2344A 2483-2488A
The Influences of Impurity Content, Tensile Strength, and Grain Size on In-Service Temper Embrittlement of CrMoV Steels.	2345-2354A	Interfaces, Microstructure Phase Transformations at Steel/IN625 Clad Interfaces. Structure of As-Cast Aluminum Matrix Composite Containing Ni. Al. Time Interpreted like Pilibbone.	665-681A 1153-1161A
See also Nonmetallic inclusions		Ni₃Al-Type Intermetallic Ribbons. Interfacial energy	1155-1161A
Mechanisms of Inclusion Formation in AI—Ti—Si—Mn De- oxidized Steel Weld Metals.	1335-1349A	See Surface energy Interfacial surface tension	
Induction (magnetic) See Magnetic induction		See Surface tension	
Inelasticity		Intergranular fracture, Alloying effects Notch Effects in Tensile Behavior of Ni ₃ Al and Ni ₃ Al + B.	1247-1255A
See Elasticity Inert gas welding		Improved Ductility of Ni₃Si by Microalloying With Boron or Carbon.	2025-2032A
See Gas tungsten arc welding		Intergranular fracture, Impurity effects Fatigue Crack Growth and Fracture Behavior of Bismuth-	
See Rare gases		Doped Copper Bicrystals.	1221-1231A
Infiltration Wetting of Ceramic Particulates With Liquid Aluminum Alloys. I. Experimental Techniques.	527-532A	Intergranular fracture, Microstructural effects The Effect of Microstructure of Ferritic Spheroidal Graphite Cast Irons on Intergranular Fracture at Intermediate Temperatures.	431-436A
Wetting of Ceramic Particulates With Liquid Aluminum Alloys. II. Study of Wettability.	533-541A	Interlayers	401-4007
Calculation of Minimum Pressure for Liquid Metal Infiltration of a Fiber Array. Microstructural Observations of Pressure Cast Ni ₃ Al/Al ₂ O ₃	1861-1866A	The Interaction of Reaction-Bonded Silicon Carbide and Inco- nel 600 With a Nickel-Based Brazing Alloy.	1803-1810A
infiltration of Fibrous Preforms by a Pure Metal. I. Theory.	2159-2166A 2535-2547A	Intermetallic compounds See Intermetallics	
Infiltration of Fibrous Preforms by a Pure Metal. II. Experi- ment.	2549-2557A	Intermetallic phases Phase Structure of the Ti ₁ Cu _{1—X} Fe _X System.	981-985A
Ingot casting Formation of Hot-Top Segregation in Steel Ingot and Effect of		Characterization of the High-Temperature Phase Fields Near Stoichiometric γ -TiAl.	1899-1906A
Steel Compositions. Structure of As-Cast Aluminum Matrix Composite Containing	723-730B	Phase Equilibria of the Al—Li Binary System. Intermetallic phases, Diffusion	2247-2258A
Ni ₃ Al-Type Intermetallic Ribbons.	1153-1161A	Interdiffusion Coefficients in the Zeta Phase of the Fe—Al System.	2561-2563A
Inhibition The Role of Crack Tip Strain Rate in the Stress Corrosion Cracking of High Strength Steels in Water.	889-895A	Intermetallic phases, Heating effects Alloy Partitioning in Ti—24AI—11Nb by Analytical Electron	
Initiation See Crack initiation		Microscopy. Intermetallic phases, Sorption	1139-1142A
Injection See also Fuel injection		Behavior of Sensitized AISI Types 321 and 347 Austenitic Stainless Steels in Hydrogen.	2187-2190A
High-Pressure Coal Injection in Zinc Slag Fuming. Impingement of Particles-Gas Jet on a Uniformly Flowing Water.	227-235B 499-508B	Intermetallics, Composite materials Structure of As-Cast Aluminum Matrix Composite Containing Ni ₃ Al-Type Intermetallic Ribbons.	1153-1161A

Microstructural Observations of Pressure Cast Ni ₉ Al/Al ₂ O ₃ and Ni/Al ₂ O ₃ Composites. Interface Characterization of Fiber-Reinforced Ni ₃ Al Matrix	2159-2166A	Iron, Quaternary systems A Study of the Thermodynamics and Phase Relationships of the Fe—Co—S—O Quaternary System.	1523-1532A
Composites.	2459-2469A	Iron, Rolling	1523-1532A
Intermetallics, Crystal growth Intermetallic Compound Layer Growth at the Interface of Solid Refractory Metals Molybdenum and Niobium With Molyber Aluminum	825-836A	Modeling Recrystallization Kinetics in a Deformed Iron Single Crystal. Iron, Structural hardening	391-401A
Molten Aluminum. Intermetallics, Mechanical properties The Effect of Molybdenum Addition on Properties of Iron Al-	825-830A	Theory of Work-Hardening Applied to Stages III and IV. Iron, Ternary systems	2393-2397A
uminides. Notch Effects in Tensile Behavior of Ni ₃ Al and Ni ₃ Al + B.	751-757A 1247-1255A	The Thermodynamic Activities of Copper and Iron in the Sys- tem Copper—Iron—Platinum at 1300°C.	127-135B
Mechanical Properties of High-Temperature Beryllium Inter- metallic Compounds.	1279-1282A	Phase Equilibria in the Al—Fe—C System: Isothermal Sections 1550-2300°C.	2703-2706A
Microstructure and Tensile Properties of Fe—40 at.% Al Alloys With C, Zr, Hf, and B Additions. Improved Ductility of Ni ₃ Si by Microalloying With Boron or Carbon.	1701-1714A 2025-2032A	The Kinetics of Nitrogen Absorption and Desorption From a Plasma Arc by Molten Iron.	175-185B
ntermetallics, Microstructure	2025-2032A	Iron and steel making See also Ironmaking	
Microstructure Evolution in TIAI Alloys With Boron Additions: Conventional Solidification. On the Mechanism of Cross Slip in Ni ₃ AI.	1847-1859A 2811-2818A	Oxygen steel making Steel making Thermodynamics of the Na ₂ O—P ₂ O ₅ System.	197-204B
ntermetallics, Oxidation Transient Oxidation of Single-Crystal β-NiAl.	499-518A	Impingement of Particles-Gas Jet on a Uniformly Flowing Water.	499-508B
ntermetallics, Phases (state of matter) Phase Structure of the Ti ₁ Cu _{1—x} Fe _x System.	981-985A	Study on the Foaming of CaO—SiO ₂ —FeO Slags. I. Foaming Parameters and Experimental Results. Study on the Foaming of CaO—SiO ₂ —FeO Slags. II. Dimen-	509-514B
nternal friction	901-903A	sional Analysis and Foaming in Iron and Steelmaking Pro- cesses.	515-521B
See also Snoek effect Beinite Formation in a Silver—Cadmium Alloy. Study of the Mechanism of Fast Diffusion of Cobalt in Tho-	1169-1174A	Iron base alloys See Ferrous alloys	
rium by Diffusion and Internal Friction Measurements.	2289-2297A	Iron compounds, Mechanical properties The Effect of Molybdenum Addition on Properties of Iron Al-	
See Residual stress		uminides. Microstructure and Tensile Properties of Fe—40 at.% Al Al-	751-757A
nterstitial defects See Interstitial impurities		loys With C, Zr, Hf, and B Additions. Iron compounds, Phases (state of matter)	1701-1714A
Interstitial impurities Study of the Hydrogen Internal Friction Peak in Nb—10 at.%	1015 10104	Phase Structure of the Ti ₁ Cu _{1-x} Fe _x System. Iron powder	981-985A
V in the Presence of Oxygen. Hydrogen Retrapping After Thermal Charging of Hydrogen in Iron Single Crystal.	1215-1219A 1793-1802A	See Iron	
on beam sputtering Modeling the Early Stages of Thin Film Formation by Ener-	1700 10021	Ironmaking Optical Basicity and the Thermodynamic Properties of Siags. Conceptual Model of the Iron Blast Furnace Considering	113-118B
getic Atom Deposition.	2609-2617A	Thermodynamic and Kinetic Constraints on the Process. Discussion of "Thermodynamic Activity of Na ₂ O in Na ₂ O—CaO—SiO ₂ , Na ₂ O—MgO—SiO ₂ , and Na ₂ O—CaO—	205-218B
Ion Beam Characterization and Treatment.	2627-2636A	SiO ₂ —Al ₂ O ₃ Melts at 1400°C°.	757-758B
on implentation Improving Tantalum's Oxidation Resistance by Al* Ion Implantation.	2101-2108A	Irradiation damage See Radiation damage	
Ion Beam Characterization and Treatment.	2627-2636A	Isostatic pressing See Hot isostatic pressing	
Kinetics of Layer Growth and Multiphase Diffusion in Ion- Nitrided Titanium.	1819-1832A	Joints See Butt welds Welded joints	
onizing radiation scattering See Neutron scattering		Junghans Rossi casting See Continuous casting	
Iron See also Cast iron		Kaldo process	
Nodular iron Iron, Binary systems		See Oxygen steel making Killed steels	
Determination of the Fe—Ni Phase Diagram Below 400°C. Mass Spectrometric Study of the Partial Phase Diagram of the Fe—Ge System Above 1050°C.	719-725A 975-976A	See also Aluminum killed steels Killed steels, Casting Formation of Hot-Top Segregation in Steel Ingot and Effect of	
Iron, Coating The Effects of Silicon on the Reaction Between Solid Iron and		Steel Compositions. Killed steels, Mechanical properties	723-730B
Liquid 55 wt.% Al—Zn Bath. Iron, Corrosion	543-555A	Correlation of Microstructure and Tempered Martensite Em- brittlement in Two 4340 Steels.	1089-1103A
A Research on Hydrogen Cracking in α-Iron. Iron, Crystal growth	2379-2384A	Kilns The Extractive Metallurgist in an Emerging World of Materi-	291-313B
Microstructural Modeling of Recrystallization in Deformed Iron Single Crystals. Iron, Crystal lattices	1933-1942A	als. A Heat-Transfer Model for the Rotary Kiln. I. Pilot Kiln Trials. A Heat-Transfer Model for the Rotary Kiln. II. Development of the Cross-Section Model.	391-402B 403-419B
Hydrogen Retrapping After Thermal Charging of Hydrogen in Iron Single Crystal.	1793-1802A	Kinetics See also Reaction kinetics	400 4100
Iron, Diffusion Two-Dimensional Finite Difference Analysis of Shape Insta-		The Mixed-Control Kinetics of Ferric Chloride Leaching of Galena.	107-110B
bilities in Plates. Interdiffusion Coefficients in the Zeta Phase of the Fe—Al		Conceptual Model of the Iron Blast Furnace Considering Thermodynamic and Kinetic Constraints on the Process.	205-218B 853-861B
System. Interdiffusion in Ternary Fe—Cr—Al Alloys.	2561-2563A 2767-2781A	Decarburization Kinetics of Liquid Fe C _{sat} Alloys by CO ₂ . Ladle metallurgy	655-6615
Iron, Heat treatment Dependence of the Lattice Parameter of γ' Iron Nitride, Fe ₄ N _{1-x} , on Nitrogen Content; Accuracy of the Nitrogen		Fluid Flow and Bath Temperature Destratification in Gas- Stirred Ladles. Fluid Flow in Pachuca (Air-Agitated) Tanks. I. Laboratory-	603-611B 781-791B
Absorption Data. Iron, Irradiation	1533-1539A	Scale Experimental Measurements. On Effective Viscosity Models for Gas-Stirred Ladle Systems.	967-969B
Impurity-Defect Interactions in Radiation Hardening and Em- brittlement in BCC Metals. In Situ Studies of Ion Irradiation Effects in an Electron Micro- scope.	2637-2649A	Lamellar structure Influence of Precipitate Morphology on Intermediate Temper- ature Creep Properties of a Nickel-Base Superalloy Single Crystal.	133-141A
Iron, Mechanical properties Determination of Effective Stress and Dislocation Velocity in the Deformation of Titanium-Doped iron.		Lamellar structure, Cooling effects The Microstructural Details of β-Sn Precipitation in a 5Sn— 95Pb Solder Alloy.	1325-1333A
Iron, Nondestructive testing Ultrasonic and Magnetic Analyses of Porosity in Iron Com-		Lamellar structure, Stress effects Observations of Directional Gamma Prime Coarsening Dur-	
pacts.	571-578A	ing Engine Operation.	683-688A
			0.40

Lanthanide metal alloys See Dysprosium base alloys Gadolinium base alloys Lanthanum base alloys		Side Branch Morphology and Coarsening in Directionally So- lidified Pb—8.4 at.% Au. Efficient Estimation of Diffusion During Dendritic Solidifica- tion.	1889-1893A 2847-2856A
Lanthanide metals See Lanthanum Neodymium		Lead base alloys, Microstructure The Microstructural Details of β-Sn Precipitation in a 5Sn— 95Pb Solder Alloy.	1325-1333A
Lanthanum, Alloying elements A Comparison of the Fracture Behavior of Two Heats of the		Life See Fatigue life	1020-10004
Secondary Hardening Steel AF1410. Lanthanum base alloys, Phases (state of matter) Physical Metallurgy of Metastable BCC Lanthanide— Magnesium Alloys for R = Lanthanum, Gadolinium and	105-123A	Light metals See Aluminum Aluminum base alloys Magnesium	
Dysprosium. Laser beam welding	1575-1583A	Magnesium base alloys Titanium	
Emission Spectroscopy of Plasma During Laser Welding of AISI 201 Stainless Steel. Heat Transfer During Nd:YAG Pulsed Laser Welding and its Effect on Solidification Structure of Austenitic Stainless Steels.	277-286B 957-967A	Titanium base alloys Light water reactors See also Pressurized water reactors Application of Modeling of the Texture Dependence of Environmentally Assisted Crack Growth of Long and Short Cracks to Zircaloy Fuel Tubins	1943-1950A
Laser processing See also Laser beam welding		Line defects	1343-1330A
Extended Solid Solution and Nonequilibrium Phase Diagram for Ni—Al Alloy Formed During Laser Cladding. Comparison of the Microstructures and Abrasive Wear Properties of Stellite Hardfacing Alloys Deposited by Arc Welding and Laser Cladding.	363-371A 1037-1054A	See Dislocations Liquid metal embrittlement Application of Modeling of the Texture Dependence of Envi- ronmentally Assisted Crack Growth of Long and Short Cracks to Zircaloy Fuel Tubing.	1943-1950A
Faceted—Nonfaceted Dendritic Transitions During the Laser Processing of Al ₂ O ₃ —1.0 wt.% MgO. Laser-Clad Ni ₇₀ Al ₂₀ Cr ₇ Hf ₃ Alloys With Extended Solid Solu-	2191-2194A	Liquid metals, Physical properties	1040 10001
tion of Hafnium. I. Microstructure Evolution. Laser-Clad Ni ₇₀ Al ₂₀ Cr ₇ H ₃ Alloys With Extended Solid Solution of Hafnium. II. Oxidation Behavior.	2267-2277A	Physical Characteristics of Gas Jets Injected Vertically Up- ward Into Liquid Metal. Liquid metals, Reactions (chemical)	595-601B
Laser welding	2489-2497A	Activities of Boron in the Binary Fe—B, Co—B, and Cu—B Melts.	705-710B
See Laser beam welding Lattice constant		Studies of the Interfacial Kinetics of the Reaction of CO ₂ With Liquid Iron—Nickel Alloys at 1873K.	755-756B
See Lattice parameters Lattice defects		Direct Activity Measurements in Liquid Ag—Cu Alloys Using a Valved Knudsen Cell—Mass Spectrometer System.	845-852B
See Crystal defects Lattice parameters		Liquid metals, Refining Kinetics of Deoxidation of Liquid Copper by Graphite Parti- cles During Submerged Injection.	187-196B
Dependence of the Lattice Parameter of γ' Iron Nitride, Fe ₄ N _{1-∞} , on Nitrogen Content; Accuracy of the Nitrogen Absorption Data.	1533-1539A	Liquid metals, Solubility Comments on the Solubility of Carbon in Molten Aluminum. The Solubility of Hydrogen in Molten Aluminum Alloys.	191A 1785-1791A
The Microstructure of Selected Annealed Vanadium-Base Al- loys.	1927-1932A	The Solubility of Titanium Diboride in Aluminum.	2185-2187A
Lattice parameters, Alloying effects X-Ray Diffraction Line Profile Analysis on the Microstructure of Cold-Worked Face-Centered Cubic Cu—Ge—Si Alloys:	4000 40054	Liquid metals, Sorption The Kinetics of Nitrogen Absorption and Desorption From a Plasma Arc by Molten Iron.	175-185B
Effects of Dilute Solutes Silicon and Germanium. Lattice sites	1883-1885A	Liquid metals, Surface properties Estimation of the Surface Tensions of Binary Liquid Alloys.	693-703B
Analysis of γ'/γ Equilibrium in Ni—AI—X Alloys by the Cluster Variation Method With the Lennard—Jones Potential. Hydrogen Retrapping After Thermal Charging of Hydrogen in	649-664A	Liquid phase diffusion See Diffusion	
iron Single Crystal. Lattices See Face centered cubic lattice	1793-1802A	Liquid phase sintering Reaction Sintering of an Fe—6 wt.% B—48 wt.% Mo Alloy in the Presence of Liquid Phases. Microstructural Change During Liquid Phase Sintering of	17-24A
Layers See also Interlayers		W-Ni-Fe Alloy. Liquidus	837-845A
Surface layer Layers, Microstructure		Equilibrium Partition Coefficients in Iron-Based Alloys. Lithium, Binary systems	149-160B
Structure of As-Cast Aluminum Matrix Composite Containing Ni ₉ Al-Type Intermetallic Ribbons.	1153-1161A	Phase Equilibria of the Al—Li Binary System. Lixiviation	2247-2258A
Leaching See also Acid leaching Bacterial leaching		See Leaching Loads (forces)	
Upgrading Ferrochromium to Chromium by Nitriding, Leaching, and Dissociation.	219-226B	See Shock loading	
The Leaching of Galena in Cupric Chloride Media. The Leaching of Sintered CuS Disks With Ferric Chlorides. Fluid Flow in Pachuca (Air-Agitated) Tanks. I. Laboratory- Scale Experimental Measurements.	475-483B 485-491B	Loops (dislocation) See Dislocation loops Losses Emission Spectroscopy of Plasma During Laser Welding of	
Lead (metal), Binary systems Metastable Phase Equilibria in the Lead—Tin Alloy System. I.	781-791B	AISI 201 Stainless Steel. Low alloy steels	277-286B
Experimental. Metastable Phase Equilibria in the Lead—Tin Alloy System. II. Thermodynamic Modeling.	785-794A 795-803A	See Carbon manganese steels Electrical steels Silicon steels	
Lead (metal), Extraction Critical Evaluation of the Thermochemical Properties of Lead Sulfates.	77-85B	Low cycle fatigue Mechanism of Cyclic Softening and Fracture of a Nickel-Base y'-Strengthened Alloy Under Low-Cycle Fatigue.	2793-2801A
Thermogravimetric Study of Lead Sulfide Chlorination Be- tween 783-953K. Mathematical Model of the Stack Region of a Commercial Lead Blast Furnace.	87-96B 97-106B	Low cycle fatigue, Impurity effects Effects of Manganese, Silicon, and Purity on the Design of 3.5NiCrMoV, 1CrMoV, and 2.25Cr—1Mo Bainitic Alloy	
The Mixed-Control Kinetics of Ferric Chloride Leaching of Galena.	107-110B	Steels. Lubrication	2197-2212A
The Leaching of Galena in Cupric Chloride Media. Lead (metal), Impurities	475-483B	Determination of Friction Coefficient for Sheet Materials Under Stretch-Forming Conditions.	2179-2182A
Gas Phase Embrittlement by Metal Vapors. Lead (metal), Ternary systems	184-188A	Macrofractography See Fractography	
Thermodynamic Consistency of the Ternary Functions. Lead base alloys, Directional solidification	2047-2055A	Magnesium, Alloying elements The Electrical Conductivity of Cast Al—Si Alloys in the Range 2-12.6 wt.% Silicon.	383-389A
Thermosolutal Convection During Dendritic Solidification of Alioys. I. Linear Stability Analysis. Thermosolutal Convection During Dendritic Solidification of Alioys. II. Nonlinear Convection.	711-721B 883-891B	Magnesium, Binary systems An Experimental Technique for the Rapid Determination of Binary Phase Diagrams: the Al—Mg System.	

Magnesium, Powder technology Flow Separation and Liquid Rundown in a Gas-Atomization		Mathematical Model of the Stack Region of a Commercial Lead Blast Furnace.	97-106B
Process. Influence of Gas Flow on Performance of "Confined" Atom-	613-622B	Determination of the Diffusion Coefficients of NiCl ₂ , ZnCl ₂ , and CdCl ₂ in Aqueous Solution.	555-565B
ization Nozzles. Magnesium base alloys, Composite materials Microphophopic and Entirum Crock Growth in an Alumina	833-843B	Development of a Mathematical Model for Multihearth Roast- ers. Fluid Flow in Solidifying Monotectic Alloys.	925-935B 2517-2527A
Micromechanics and Fatigue Crack Growth in an Alumina- Fiber-Reinforced Magnesium Alloy Composite. Magnesium base alloys, Metallography	2369-2378A	Mass transfer, Radiation effects Irradiation-Enhanced and -Induced Mass Transport.	2619-2626A
Crystallography of Directionally Solidified Magnesium Alloy AZ91.	847-852A	Materials testing See Depth profiling Quantitative analysis	
Magnetic fields The Effect of Ultrahigh Magnetic Fields on Dopant Distribution in CZ Systems: a Modeling Study and Comparison With Asymptotic Solutions.	1637-1646A	Surface analysis (chemical) Ultrasonic testing Mathematical analysis	
Phase Distributions in Rapidly Solidified Stainless Steels.	2259-2266A	High-Pressure Coal Injection in Zinc Stag Fuming. Correction to "Thermodynamic Consistency of the Interaction	227-2358
Magnetic flux welding See Gas metal arc welding		Parameter Formalism". Transient Tensile Behavior of Interstitial-Free Steel and 70/30	269-275B
Magnetic force See Magnetic fields		Brass Following Plane-Strain Deformation. A Mass Transport Theory for Interphase Precipitation With	1483-1493A
Magnetic hysteresis		Application to Vanadium Steels. Correction to "A Mass Transport Theory for Interphase Pre-	1647-1655A
See Hysteresis Magnetic induction		cipitation With Application to Vanadium Steels". The Solubility of Hydrogen in Molten Aluminum Alloys.	1647-1655A 1785-1791A
Growth Dynamics Study of the Martensitic Transformation in Fe—30Ni Alloys. I. Quantitative Measurements of Growth	1004 10454	Hydrogen Rétrapping Āfter Thermal Charging of Hydrogen in Iron Single Crystal. Calculation of Minimum Pressure for Liquid Metal Infiltration	1793-1802A
Velocity. Magnetic properties	1601-1615A	of a Fiber Array. Theory of Work-Hardening Applied to Stages III and IV.	1861-1866A 2393-2397A
See Coercive force Curie temperature		Infiltration of Fibrous Preforms by a Pure Metal. I. Theory.	2535-2547A
Magnetic relaxation		Analysis of the Temperature Dependence of Strain- Hardening Behavior in High-Strength Steel.	2819-2829A
See Magnetic induction Magnetization		Efficient Estimation of Diffusion During Dendritic Solidifica- tion.	2847-2856A
Production of Nd—Fe—B Alloy Powders Using High- Pressure Gas Atomization and Their Hard Magnetic Prop-		Mathematical models Mathematical Modeling of Minor-Element Behavior in Flash Smelting of Copper Concentrates and Flash Converting of	
erties. Ultrasonic and Magnetic Analyses of Porosity in Iron Com-	5-11A	Copper Mattes. Mathematical Modeling of Mixing Phenomena in a Gas	39-51B
pacts. Malcomizing	571-578A	Stirred Liquid Bath. A Mathematical Model of the Spray Deposition Process.	53-59B 71-85A
See Nitriding		Mathematical Model of the Stack Region of a Commercial Lead Blast Furnace.	
Manganese, Alloying elements Carbide Stability Diagrams in 2.25Cr—1Mo Steels.	1561-1564A	Equilibrium Surface Composition of Ternary Alloys. Similarity Solutions for Phase-Change Problems.	215-223A 225-235A
Manganese, Binary systems Some Phase-Diagram Aspects of the Manganese—Carbon System.	747-754B	The Role of Transport Phenomena in the Plasma Synthesis of Fine Particles: the Production of Silicon Powder. Calculation of the Product Phase Grain Edge Length and	243-250B
Manganese, Diffusion	20.544	Quadruple Points per Unit Volume During Solid State Transformations.	
Isothermal Particle Growth in Two-Phase Titanium Alloys. Manganese, Impurities	39-54A	Two-Dimensional Model for Twin-Roll Continuous Casting. Modeling Recrystallization Kinetics in a Deformed Iron Single	381-390B
Effects of Manganese, Silicon, and Purity on the Design of 3.5NiCrMoV, 1CrMoV, and 2.25Cr—1Mo Bainitic Alloy Steels.	2197-2212A	Crystal. A Heat-Transfer Model for the Rotary Kiln. I. Pilot Kiln Trials. A Heat-Transfer Model for the Rotary Kiln. II. Development of	391-401A 391-402B
Manual metal arc welding See Shielded metal arc welding		the Cross-Section Model. Mathematical Modeling of an Aluminum Casting Furnace	403-419B
Maraging steels, Mechanical properties		Combustion Chamber. The Effect of Small Plastic Deformation and Annealing on the	421-429B
A Comparison of the Fracture Behavior of Two Heats of the Secondary Hardening Steel AF1410.	105-123A	Properties of Polycrystals. II. Theoretical Model for the Transformation of Nonequilibrium Grain Boundaries.	479-484A
Microvoid Formation During Shear Deformation of Ultrahigh Strength Steels.	143-153A	Analytical Models for the Gas Carburizing Process. Three-Dimensional Transient Model for Arc Welding Process. Nucleation Kinetics of Titanium Carbonitride in Microalloyed	535-546B 645-659B
Martensite, Alloying effects The Microstructure of Chromium—Tungsten Steels.	373-382A	Austenite. Vacuum Distillation of Copper Matte to Remove Lead, Arse-	689-697A
Martensitic stainless steels, Mechanical properties Near-Threshold Fatigue Crack Growth Properties at Elevated		nic, Bismuth, and Antimony. Thermosolutal Convection During Dendritic Solidification of	
Temperature for 1Cr—1Mo—0.25V Steel and 12Cr Stainless Steel.	741-749A	Alloys. II. Nonlinear Convection. Development of a Mathematical Model for Multihearth Roast-	883-891B
Martensitic transformations Electron Microscopy Study of the Early Stage of the Marten-		ers. Prediction of Weld Pool and Reinforcement Dimensions of	925-9358
sitic Transformation in a U(Ga) Alloy. Growth Dynamics Study of the Martensitic Transformation in	1163-1168A	GMA Welds Using a Finite-Element Model. Effects of Particle Loading on a Reduced Pressure Induc-	937-947B
Fe—30Ni Alloys. I. Quantitative Measurements of Growth Velocity.	1601-1615A	tively Coupled Radio Frequency Plasma Torch. Modeling of Fluidized Bed Chlorination of Rutile.	949-958B 959-966B
Growth Dynamics Study of the Martensitic Transformation in Fe—30Ni Alloys. II. Computer Simulation of Martensitic		On Effective Viscosity Models for Gas-Stirred Ladle Systems. A Mathematical Model Describing Carburization in Multiele-	
Growth. Nonbasal Plane Defects in 18R Martensite and the Effect of	1617-1629A	ment Alloy Systems. Calculation of the $Ti(C_yN_{1-y})$ — $Ti_4C_2S_2$ —MnS—Austenite Equilibrium in Titanium-Bearing Steels.	1021-1028A
Abnormal Defects on Thermoelastic Martensitic Transformation.	1631-1636A	Precipitation Behavior of MnS During δ/γ Transformation in	
[011] Twinning in Fe—Ni—C Martensites.	2739-2747A	Fe—Si Alloys. Two-Dimensional Finite Difference Analysis of Shape Insta-	1375-1383A
Martensitic transformations, Deformation effects Effect of Strain Rate on Martensitic Transformation During Uniaxial Testing of AISI-304 Stainless Steel.	2857-2859A	bilities in Plates. The Effect of Ultrahigh Magnetic Fields on Dopant Distribu- tion in CZ Systems: a Modeling Study and Comparison	
Marteneitic transformations, Microstructural effects Correction to "Microstructural Refinement of W—Ni—Fe Heavy Alloys by Alloying Additions".	3100-3103A	With Asymptotic Solutions. Modeling of Multidimensional Solidification of an Alloy. Application of Modeling of the Texture Dependence of Environmentally Assisted Crack Growth of Long and Short	1637-1646A 1833-1845A
Mass spectra Atom-Probe Analysis of GP Zones in an Al—1.7 at.% Cu		Cracks to Zircaloy Fuel Tubing. Calculation of the Forming Limit Diagram.	1943-1950A 1975-1987A
Alloy. Mass transfer	1585-1591A	The Solubility of Titanium Diboride in Aluminum. Hydrogen Trapping in Thoria-Dispersed Nickel. Modeling the Early Stages of Thin Film Formation by Ener-	2185-2187A 2483-2488A
Nonuniformity of NaOH Concentration and Effective Bubble Diameter in CO ₂ Injection Into Aqueous NaOH Solution.	5-12B	getic Atom Deposition.	2609-2617A
Electrode Mass Transfer Under Conditions of Natural and Forced Convection.	21-29B	Mathematics See Finite element method	
Mathematical Modeling of Minor-Element Behavior in Flash Smelting of Copper Concentrates and Flash Converting of Copper Mattes.		Mathematical analysis Mathematical models Topology	

Mattes See also Copper mattes		Fracture and Fatigue Crack Propagation in a Nickel-Base Metallic Glass.	1395-1409A
Mattes, Recovering	773-779B	Metallographic structures See Microstructure	1393-1409A
Microbiological Leaching of Copper From Lead Mattes. Measurement	773-7795	Metallography	
See Calorimetry Mechanical hysteresis		See Quantitative metallography Metalloid compounds	
See Hysteresis		See Silicon carbide	
Mechanical properties		Silicon compounds	
See Bonding strength Creep (materials)		Metalloids See Boron	
Creep rate		Silicon	
Creep rupture strength Diamond pyramid hardness		Tellurium	
Diamond pyramid hardness Ductile brittle transition Ductility		Metastable phases Phase Decomposition of Rapidly Solidified Fe—Mn—Al—C	
Elastic constants		Austenitic Alloys.	205-214A
Elastic limit Elasticity		Freezing Diagrams. I. Development and Implications for Glass Formability.	287-297A
Elongation		Freezing Diagrams. II. Comparison With Experimental Obser-	
Fatigue (materials) Fatigue life		vation and Relevance to Crystallization of Metallic Glass. Transient Oxidation of Single-Crystal β-NiAl.	299-309A 499-518A
Fatigue limit		Analysis of γ'/γ Equilibrium in Ni—Al—X Alloys by the Cluster	640 6644
Fracture strength Fracture toughness		Variation Method With the Lennard—Jones Potential. Metastable Phase Equilibria in the Lead—Tin Alloy System. I.	649-664A
Hardness		Experimental. Metastable Phase Equilibria in the Lead—Tin Alloy System.	785-794A
Hydrogen embrittlement Impact strength		II. Thermodynamic Modeling.	795-803A
Internal friction		Formation of Metastable Structures and Amorphous Phases in Plutonium-Based Systems Using the Sputtering Tech-	
Microhardness Modulus of elasticity		nique.	813-823A
Notch sensitivity		Phase Diagrams in Materials Science. Phase Diagrams in Materials Science.	1295-1323A 1295-1323B
Notch toughness Plastic flow		Physical Metallurgy of Metastable BCC Lanthanide-	
Plasticity Residual stress		Magnesium Alloys for R = Lanthanum, Gadolinium and Dysprosium.	1575-1583A
Shear properties		The Evolution of Microstructure in the Undercooled Zn-Sn	
Shear strength Shear stress		Entrained Droplets.	2109-2115A
Snoek effect		Metastable phases, Microstructure Phase Transformations in the Al—Li—Hf and Al—Li—Ti	
Stress relaxation Superplasticity		Systems.	999-1019A
Tear strength Temper brittleness		Microalloyed steels See High strength low alloy steels	
Tensile properties		Microbial leaching	
Tensile strength Toughness		See Bacterial leaching	
True strain Wear resistance		Microcracking See Crack initiation	
Yield strength		Microfractography	
Mechanical tests		See Fractography	
See also Fracture testing Tension tests		Microhardness	
Mechanical Properties of Thin Films.	2217-2245A	Mechanical Properties of High-Temperature Beryllium Inter- metallic Compounds.	1279-1282A
Mechanics See Fracture mechanics		Microhardness, Coating effects	
Kinetics		A TEM Study of CVD TiC _x /Ti(C, N) _x Coating on WC—Co Cemented Carbide.	279-285B
Melt spinning		Microhardness, Deformation effects	
Precipitation of Silicon in Aluminum—Silicon: a Calorimetric Analysis of Liquid-Quenched and Solid-Quenched Alloys.	1207-1214A	Recrystallization Microstructure in Cold-Rolled Aluminum	1743-1753A
The Microstructure of Rapidly Solidified Ti—Fe Melt-Spun Ribbons.	2841-2845A	Compositès Reinforced by Silicon Carbide Whiskers. Microscopy	1740-1753A
Melting	2011 201011	See Electron microscopy	
See Plasma arc melting Zone melting		Field ion microscopy Scanning electron microscopy	
Melting furnaces		Microstructure	
See Bottom blown converters		See also Graphitic structure Lamellar structure	
Memory (shape)		Nodular graphitic structure	
See Shape memory		Reaction Sintering of an Fe—6 wt.% B—48 wt.% Mo Alloy in the Presence of Liquid Phases.	17-24A
Memory devices See Data storage		Microstructure, Alloying effects	
Mercury (metal), Physical properties		Effect of Tellurium on Morphological Transitions in Fe—C— Si Alloys. I. Directional Solidification.	1867-1873A
Physical Characteristics of Gas Jets Injected Vertically Up- ward Into Liquid Metal.	595-601B	Effect of Tellurium on Morphological Transitions in Fe-C-	
Metal carbides	393-0016	Si Alloys. II. Auger Analysis.	1875-1881A
See Boron carbide		Microstructure, Heating effects Structure and Properties of a β Solution Treated, Quenched,	
Titanium carbide		and Aged Silicon-Bearing Near-α Titanium Alloy.	55-62A
Metal powders See also Alloy powders		The Effect of Microstructure on Properties and Behaviors of Annealed Fe ₇₈ B ₁₃ Si ₉ Amorphous Alloy Ribbon.	63-70A
Metal powders, Synthesis		Microstructure, Welding effects	
The Role of Transport Phenomena in the Plasma Synthesis of Fine Particles: the Production of Silicon Powder.	243-250B	Effects of Microstructure on Fatigue Crack Initiation and Propagation of 16Mn Steel.	413-419A
Metal scrap	L-10-200D	Mig arc welding	
See Steel scrap		See Gas metal arc welding	
Metal working See Cold rolling		Miscibility The Evolution of Microstructure in the Undercooled Zn—Sn	
Controlled rolling		Entrained Droplets.	2109-2115A
Forging Hot rolling		Mixing Mathematical Modeling of Mixing Phanomena in a Gas	
Rolling Stretch forming		Mathematical Modeling of Mixing Phenomena in a Gas Stirred Liquid Bath.	53-59B
Thermomechanical treatment		Mobility	
Wire drawing		See Dislocation mobility	
Metallic glasses, Mechanical properties The Effect of Microstructure on Properties and Behaviors of		Modification Dissolution of Reactive Strontium-Containing Alloys in Liquid	

Correction to "Orientation Dependence of $\beta_1 \rightarrow \beta_1$ Stress-		Nickel, Irradiation	
Induced Martensitic Transformation in a Cu—Al—Ni Alloy". Modulus of elasticity	915-923A	Irradiation-Enhanced and -Induced Mass Transport. In Situ Studies of Ion Irradiation Effects in an Electron Microscope.	2619-2626A 2673-2680A
Mechanical Properties of High-Temperature Beryllium Inter- metallic Compounds. Mechanical Properties of Thin Films.	1279-1282A 2217-2245A	Nickel, Nondestructive testing Acoustic Emission From Intergranular Subcritical Crack Growth.	637-648A
Modulus of elasticity, Radiation effects Mechanical Property Changes in Ion-Irradiated Metals. ii. High-Strength Cu—Ni—Be Alloy.	2689-2693A	Nickel, Recovering Cementation of Cobalt, Nickel and Cadmium in Ammoniacal	
Moisture See Water		Medium Using Zinc Metal. Nickel base alloys, Brazing The Interaction of Reaction-Bonded Silicon Carbide and Inco-	547-550B
Molten metals See Liquid metals		nel 600 With a Nickel-Based Brazing Alloy. Nickel base alloys, Cladding	1803-181CA
Molybdenum, Alloying elements The Effect of Molybdenum Addition on Properties of Iron Aluminides.	751-757A	Phase Transformations at Steel/IN625 Clad Interfaces. Laser-Clad Ni ₇₀ Al ₂₀ Cr ₇ Hf ₃ Alloys With Extended Solid Solution of Hafnium. I. Microstructure Evolution.	665-681A 2267-2277A
Molybdenum base alloys, Powder technology Reaction Sintering of an Fe—6 wt.% B—48 wt.% Mo Alloy in the Presence of Liquid Phases.	17-24A	Laser-Clad Ni ₇₀ Al ₂₀ Cr ₇ Hf ₃ Alloys With Extended Solid Solution of Hafnium. II. Oxidation Behavior.	2489-2497A
Molybdenum chromium nickel steels See Nickel chromium molybdenum steels	11.541	Nickel base alloys, Claddings Extended Solid Solution and Nonequilibrium Phase Diagram for Ni—Al Alloy Formed During Laser Cladding.	363-371A
Molybdenum chromium steels See Chromium molybdenum steels		Nickel base alloys, Composite materials High Temperature Reaction Zone Growth in Tungsten Fiber Reinforced Superalloy Composites. II. Matrix Chemistry Ef-	
Molybdenum compounds, Crystal growth Intermetallic Compound Layer Growth at the Interface of Solid Refractory Metals Molybdenum and Niobium With		fects. Nickel base alloys, Corrosion	267-272A
Molybdenum nickel chromium steels See Nickel chromium molybdenum steels	825-836A	The Effects of Heat Treatment on the Sensitization and SCC Behavior of Inconel 600 Alloy. Hydrogen Embrittlement of Iron—Nickel Alloys.	1077-1088A 1475-1482A
Molybdenum nickel steels See Nickel molybdenum steels		Mass Spectrometric Observations of Metal Oxychlorides Produced by Oxidation—Chlorination Reactions. The Effects of Heat Treatment on the Chromium Depletion,	1566-1568A
Molybdenum steels See also Chromium molybdenum steels		Precipitation Evolution, and Corrosion Resistance of Inco- nel Alloy 690.	2057-2067A
Chromium molybdenum vanadium steels Nickel chromium molybdenum steels Nickel molybdenum steels		Nickel base alloys, Diffusion Two-Dimensional Finite Difference Analysis of Shape Instabilities in Plates.	1385-1394A
Molybdenum steels, Corrosion		The Effect of Composition on Marker Movement and Kirken- dall Porosity in Ternary Alloys.	2299-2303A
Fatigue Crack Growth Behavior of Pressure Vessel Steels and Submerged Arc Weldments in a High-Temperature Pressurized Water Environment.	2069-2085A	Nickel base alloys, Heat treatment A Mathematical Model Describing Carburization in Multielement Alloy Systems.	1021-1028A
Molybdenum steels, Rolling Effect of Deformation on Ferrite Nucleation and Growth in a Plain Carbon and Two Microalloyed Steels.	987-998A	Nickel base alloys, Irradiation Ordering in the Fe—Ni System Under Electron Irradiation. Fluctuations in Composition in Dilute Alloys Under Irradiation.	711-718A 2599-2607A
Monitoring Eddy Current Analysis of Precipitation Kinetics in Aluminum Alloys.	605-610A	Irradiation-Enhanced and -Induced Mass Transport. In Situ Studies of Ion Irradiation Effects in an Electron Microscope.	2619-2626A 2673-2680A
The Influence of Tempering Temperature on Small Fatigue Crack Behavior Monitored With Surface Acoustic Waves in Quenched and Tempered 4140 Steel.	1257-1265A	Mechanical Property Changes in Ion-Irradiated Metals. I. Ni—Cu Alloys.	2681-2687A
Characterization of Formability in Cold-Rolled Steel Sheets Using Electromagnetic Acoustic Transducers. A Creep Technique for Monitoring MnS Precipitation in Sill-	2385-2392A	Nickel base alloys, Mechanical properties Influence of Precipitate Morphology on Intermediate Temperature Creep Properties of a Nickel-Base Superalloy Single	
con Steels. Monocrystals	2707-2715A	Crystal. Correlation of Microstructure and Creep Stages in the (100) Oriented Superalloy SRR99 at 1253K.	133-141A 1233-1238A
See Single crystals		Fracture and Fatigue Crack Propagation in a Nickel-Base Me- tallic Glass.	1395-1409A
Multi hearth roasters See Hearth roasters		The Correlation Between the Temperature Dependence of the CRSS and the Formation of Superlattice-Intrinsic	
Multipurpose reactors See Nuclear reactors Natural strain		Stacking Faults in the Nickel-Base Superalloy PWA 1480. Mechanism of Cyclic Softening and Fracture of a Nickel-Base γ'-Strengthened Alloy Under Low-Cycle Fatigue.	1888-1889A 2793-2801A
See True strain		Nickel base alloys, Microstructure Observations of Directional Gamma Prime Coarsening Dur-	****
Necking Calculation of the Forming Limit Diagram. Necdymium, Extraction	1975-1987A	ing Engine Operation. An Elastically Induced Morphological Instability of a Misfitting Precipitate.	683-688A 2171-2175A
A Molten Salt Process for Producing Neodymium and Neodymium—Iron Alloys.	805-813B	Nickel base alloys, Phase transformations Phase Stability by the Artificial Concentration Wave Method.	357-362A
Neutron scattering A Small-Angle Neutron Scattering Study of the Kinetics of Phase Separation in a Supersaturated Ni—12.5 at.% Si Alloy.		Nickel base alloys, Phases (state of matter) Analysis of γ'/γ Equilibrium in Ni—Ai—X Alloys by the Cluster Variation Method With the Lennard—Jones Potential.	649-664A
Nickel, Alloying elements Observations on the Faceted Fatigue Fracture of Cast Co—		Nickel base alloys, Reactions (chemical) Studies of the Interfacial Kinetics of the Reaction of CO ₂ With Liquid Iron—Nickel Alloys at 1873K.	755-756B
Cr—Mo Alloy Used for Surgical Implants. Effect of Thermal Conditions and Alloying Constituents (Ni,Cr) on Macrosegregation in Continuously Cast High- Carbon (0.8%), Low-Alloy Steel.		Nickel base alloys, Solubility Correction to "Thermodynamic Consistency of the Interaction Parameter Formalism".	269-275B
Nickel, Binary systems Determination of the Fe—Ni Phase Diagram Below 400°C.	719-725A	Nickel base alloys, Structural hardening A Small-Angle Neutron Scattering Study of the Kinetics of Phase Separation in a Supersaturated Ni—12.5 at.% Si	
Nickel, Cladding Extended Solid Solution and Nonequilibrium Phase Diagram for Ni—Al Alloy Formed During Laser Cladding.	363-371A	Alloy. Solidification of the Nickel-Base Superalloy 718: a Phase Diagram Approach.	699-710A
Nickel, Composite materials Microstructural Observations of Pressure Cast Ni ₃ Al/Al ₂ O ₃		Nickel base alloys, Welding Inconel 718: a Solidification Diagram.	2149-2158A
and Ni/Al ₂ O ₃ Composites. Nickel, Corrosion Hydrogen Embrittlement of Iron—Nickel Alloys.	2159-2166A 1475-1482A	Nickel chromium molybdenum steels, Alloy development Effects of Manganese, Silicon, and Purity on the Design of 3.5NiCrMoV, 1CrMoV, and 2.25Cr—1Mo Bainitic Alloy	9107 00101
Hydrogen Trapping in Thoria-Dispersed Nickel. Nickel, Diffusion The Effect of Chromium on Antimony and Nickel Grain	2483-2488A	Steels. Nickel chromium molybdenum steels, Corrosion The Role of Crack Tip Strain Rate in the Stress Corrosion	2197-2212A
Boundary Segregation in Iron.	2170-2171A	Cracking of High Strength Steels in Water.	889-895A

Fatigue Crack Growth Behavior of Pressure Vessel Steels and Submerged Arc Weldments in a High-Temperature Pressurized Water Environment.	2069-2085A	Investigations on the Influence of Internal Nitridation on Creep Crack Growth in Alloy 800H. Nitrogen, Diffusion	1553-1560A
Nickel chromium molybdenum steels, Heat treatment The Effects of Surface Hardening on Fracture Toughness of Carburized Steel.	519-525A	Diffusivities and Viscosities of Some Gases at Elevated Tem- peratures: Gas Diffusivities in Porous Solids.	141-148B
Duplex Treatment of High-Strength Steels.	1687-1699A	Nitrogen, Sorption The Kinetics of Nitrogen Absorption and Desorption From a	
Nickel chromium molybdenum steels, Mechanical properties		Plasma Arc by Molten Iron.	175-185B
Microvoid Formation During Shear Deformation of Ultrahigh Strength Steels.	143-153A	Noble gases See Rare gases	
The Effect of Void Shape on Void Growth and Ductility in Axisymmetric Tension Tests.	853-861A	Noble metals See Precious metals	
Correlation of Microstructure and Tempered Martensite Em- brittlement in Two 4340 Steels.	1089-1103A	Nodular graphitic structure	
Nickel chromium motybdenum steels, Metallography Possible NDE Correlation With Fractography in 4340 Steel. Stereo (Scanning Electron Microscopy) Section Fractography	323A	Ultrasonic Nondestructive Evaluation of Matrix Structures and Nodularity in Cast Irons.	2399-2407A
Stereo (Scanning Electron Microscopy) Section Fractography of Isolated Cleavage Regions in Nuclear Vessel Steels.	2862-2866A	Nodular iron, Mechanical properties The Effect of Microstructure of Ferritic Spheroidal Graphite	
Nickel chromium steels	EGGE EGGGA	Cast Irons on Intergranular Fracture at Intermediate Temperatures.	431-436A
See also Nickel chromium molybdenum steels Nickel chromium steels, Heat treatment		Nodular iron, Microstructure	401 4001
Duplex Treatment of High-Strength Steels.	1687-1699A	Ultrasonic Nondestructive Evaluation of Matrix Structures and Nodularity in Cast Irons.	2399-2407A
Nickel compounds, Composite materials Structure of As-Cast Aluminum Matrix Composite Containing	1150 11614	Nodules (graphite) See Nodular graphitic structure	
Ni ₃ Al-Type Intermetallic Ribbons. Microstructural Observations of Pressure Cast Ni ₃ Al/Al ₂ O ₃	1153-1161A	Nondestructive testing	
and Ni/Al ₂ O ₃ Composites. Interface Characterization of Fiber-Reinforced Ni ₃ Al Matrix	2159-2166A	See Eddy current testing Ultrasonic testing	
Composites. Nickel compounds, Mechanical properties	2459-2469A	Nonferrous smelting	
Notch Effects in Tensile Behavior of NigAl and NigAl + B. Grain-Boundary Contamination and Ductility Loss in Boron-	1247-1255A	See Smelting Nonmetallic inclusions	
Doped Ni ₃ Ai. Improved Ductility of Ni ₃ Si by Microalloying With Boron or	2017-2023A	Morphology of Nonmetallic Inclusions Using Silicon, Alumi- num, and Calcium—Silicon Alloy in Steel Melt.	581-594B
Carbon.	2025-2032A	Microstructural Trapping Effects on Hydrogen Induced Cracking of a Microalloyed Steel.	909-919A
Nickel compounds, Microstructure On the Mechanism of Cross Slip in Ni ₃ Al.	2811-2818A	Quantitative Characterization of Microcracking in A533B Steel by Acoustic Emission.	1105-1114A
Nickel compounds, Oxidation Transient Oxidation of Single-Crystal β -NiAl.	499-518A	Nonmetallic inclusions, Cooling effects	
Nickel molybdenum chromium steels	435-310A	Precipitation Behavior of MnS During δ/γ Transformation in Fe—Si Alloys. Solidification of High-Speed Tool Steels.	1375-1383A 2133-2148A
See Nickel chromium molybdenum steels Nickel molybdenum steels		Nonmetallic inclusions, Microstructure	2133-2140A
See also Nickel chromium molybdenum steels		Characterization of Titanium Carbosulfide Precipitation in Ti- tanium Microalloyed Steels.	1907-1915A
Nickel molybdenum steels, Mechanical properties Quantitative Characterization of Microcracking in A533B Steel by Acoustic Emission.	1105-1114A	Nonmetallic inclusions, Solubility Calculation of the Ti(C ₂ N _{1-y})—Ti ₄ C ₂ S ₂ —MnS—Austenite Equilibrium in Titanium-Bearing Steels.	1361-1374A
Nickel molybdenum steels, Metallography Stereo (Scanning Electron Microscopy) Section Fractography of Isolated Cleavage Regions in Nuclear Vessel Steels.	2862-2866A	Notch ductility See Ductility	1001 101 41
Nickel steels		Notch effect	
See also Nickel chromium molybdenum steels Nickel chromium steels Nickel molybdenum steels		See Notch sensitivity Notch impact strength	
Nickel steels, Heat treatment		See Impact strength	
Carbide Precipitation During Stage I Tempering of Fe—Ni— C Martensites.	2749-2765A	Notch sensitivity, Alloying effects Notch Effects in Tensile Behavior of Ni ₃ Al and Ni ₃ Al + B.	1247-1255A
Nickel steels, Microstructure [011] Twinning in Fe-Ni-C Martensites.	2739-2747A	Notch toughness, Heating effects Duplex Treatment of High-Strength Steels.	1687-1699A
Nickel steels, Structural hardening Spinodal Decomposition During Aging of Fe—Ni—C Mar-		Notched bar tensile test See Tension tests	
tensites.	2717-2737A	Nuclear fusion reactors	
Niobium, Alloying elements Austenite Recrystallization and Carbonitride Precipitation in		Behavior of Sensitized AISI Types 321 and 347 Austenitic Stainless Steels in Hydrogen.	2187-2190A
Niobium Microalloyed Steels. Precipitation and Fine Structure in Medium-Carbon Vanadium	25-38A	Nuclear fusion reactors, Materials selection Combined Effects of Oxygen and Hydrogen on Tensile Prop-	
and Vanadium/Niobium Microalloyed Steels. Niobium, Irradiation	2279-2288A	erties of a Nb—10 at.% V Alloy. The Microstructure of Chromium—Tungsten Steels.	273-278A 373-382A
Impurity-Defect Interactions in Radiation Hardening and Em- brittlement in BCC Metals.	2637-2649A	Heat Treatment Behavior and Tensile Properties of Cr—W Steels.	463-470A
Niobium base allovs. Mechanical properties	2007-2043A	The Microstructure of Selected Annealed Vanadium-Base Alloys.	1927-1932A
Combined Effects of Oxygen and Hydrogen on Tensile Properties of a Nb—10 at.% V Alloy. Study of the Hydrogen Internal Friction Peak in Nb—10 at.%	273-278A	Nuclear reactors	1021 10021
Study of the Hydrogen Internal Friction Peak in Nb—10 at.% V in the Presence of Oxygen.	1215-1219A	See also Fast nuclear reactors Light water reactors	
Niobium compounds, Crystal growth		Nuclear fusion reactors Pressurized water reactors	
		Study of the Hydrogen Internal Friction Peak in Nb—10 at.% V in the Presence of Oxygen.	1215-1219A
Intermetallic Compound Layer Growth at the Interface of Solid Refractory Metals Molybdenum and Niobium With		Stereo (Scanning Electron Microscopy) Section Fractography	
Solid Refractory Metals Molybdenum and Niobium With Molten Aluminum.	825-836A	of Isolated Cleavage Regions in Nuclear Vessel Steels.	2862-2866A
Solid Refractory Metals Molybdenum and Niobium With		of Isolated Cleavage Regions in Nuclear Vessel Steels. Nuclear scattering	2862-2866A
Solid Refractory Metals Molybdenum and Niobium With Molten Aluminum. Niobium compounds, Mechanical properties Mechanical Properties of High-Temperature Beryllium Intermetallic Compounds. Nitrides		of Isolated Cleavage Regions in Nuclear Vessel Steels. Nuclear scattering See Neutron scattering	2862-2866A
Solid Refractory Metals Molybdenum and Niobium With Molten Aluminum. Niobium compounds, Mechanical properties Mechanical Properties of High-Temperature Beryllium Intermetallic Compounds. Nitrides See Silicon nitride Nitriding		of Isolated Cleavage Regions in Nuclear Vessel Steels. Nuclear scattering See Neutron scattering Nucleation Calculation of the Product Phase Grain Edge Length and Quadruple Points per Unit Volume During Solid State	
Solid Refractory Metals Molybdenum and Niobium With Molten Aluminum. Niobium compounds, Mechanical properties Mechanical Properties of High-Temperature Beryllium Intermetallic Compounds. Nitrides See Silicon nitride Nitriding See also Ion nitriding Upgrading Ferrochromium to Chromium by Nitriding, Leach-	1279-1282A	of Isolated Cleavage Regions in Nuclear Vessel Steels. Nuclear scattering See Neutron scattering Nucleation Calculation of the Product Phase Grain Edge Length and Quadruple Points per Unit Volume During Solid State Transformations.	2862-2866A 349-355A
Solid Refractory Metals Molybdenum and Niobium With Molten Aluminum. Niobium compounds, Mechanical properties Mechanical Properties of High-Temperature Beryllium Intermetallic Compounds. Nitrides See Silicon nitride Nitriding See also Ion nitriding Upgrading Ferrochromium to Chromium by Nitriding, Leaching, and Dissociation. Dependence of the Lattice Parameter of γ' Iron Nitride,	1279-1282A 219-226B	of Isolated Cleavage Regions in Nuclear Vessel Steels. Nuclear scattering See Neutron scattering Nucleation Calculation of the Product Phase Grain Edge Length and Quadruple Points per Unit Volume During Solid State	
Solid Refractory Metals Molybdenum and Niobium With Molten Aluminum. Niobium compounds, Mechanical properties Mechanical Properties of High-Temperature Beryllium Intermetallic Compounds. Nitrides See Silicon nitride Nitriding See also Ion nitriding Upgrading Ferrochromium to Chromium by Nitriding, Leaching, and Dissociation.	1279-1282A 219-226B	of Isolated Cleavage Regions in Nuclear Vessel Steels. Nuclear scattering See Neutron scattering Nucleation Calculation of the Product Phase Grain Edge Length and Quadruple Points per Unit Volume During Solid State Transformations. Nucleation, Deformation effects Effect of Deformation on Ferrite Nucleation and Growth in a	349-355A

Order disorder Analysis of γ'/γ Equilibrium in Ni—Al—X Alloys by the Cluster		Particle shape The Effects of Elastic Stress on the Kinetics of Ostwald Ri-	
Variation Method With the Lennard—Jones Potential.	649-664A	pening: the Two-Particle Problem.	1175-1189A
Determination of the Fe—Ni Phase Diagram Below 400°C. Synthesis and Structural Aspects of Quasicrystals in Mg— AI—Ag System: Mg ₄ Al ₆ Ag.	719-725A 805-812A	Particle size A Small-Angle Neutron Scattering Study of the Kinetics of Phase Separation in a Supersaturated Ni—12.5 at.% Si	
Order disorder, Alloying effects The Effect of Molybdenum Addition on Properties of Iron Al-		Alloy. Influence of Gas Flow on Performance of "Confined" Atom-	699-710A
uminides. Order disorder, Radiation effects	751-757A	ization Nozzles. Microstructural Change During Liquid Phase Sintering of	833-843B
Ordering in the Fe—Ni System Under Electron Irradiation.	711-718A	W—Ni—Fe Alloy. The Effects of Elastic Stress on the Kinetics of Ostwald Ri-	837-845A
Ordering See Order disorder		pening: the Two-Particle Problem. Friction Properties of Al—1.5Mg/SiC Particulate Metal-Matrix Composites.	1175-1189A 1564-1566A
Ores See Ilmenite		Particle size, Alloying effects	1004-10004
Orientation		X-Ray Diffraction Line Profile Analysis on the Microstructure of Cold-Worked Face-Centered Cubic Cu—Ge—Si Alloys:	
See Grain orientation Orientation relationships Preferred orientation		Effects of Dilute Solutes Silicon and Germanium. Particle size distribution	1883-1885A
Orientation relationships		Production of Nd—Fe—B Alloy Powders Using High- Pressure Gas Atomization and Their Hard Magnetic Prop-	
Electron Microscopy Study of the Early Stage of the Marten- sitic Transformation in a U(Ga) Alloy.	1163-1168A	erties. Liquid Break-Up in Gas Atomization of Fine Aluminum Pow-	5-11A
Microstructure of High-Tensile Strength Brasses Containing Silicon and Manganese.	1199-1206A	ders. Modeling of Fluidized Bed Chlorination of Rutile.	61-69B 959-966B
Discussion of "The Mechanism of Silicon Modification in Aluminum—Silicon Alloys: Impurity-Induced Twinning". The Microstructural Details of S.S. Proceptition in a Screen	1286-1290A	Particles (of physics) See Antiparticles	
The Microstructural Details of β -Sn Precipitation in a 5 Sn— 95Pb Solder Alloy. Elastic Interaction Stresses. II. The Influence of Orientation	1325-1333A	Particulate composites, Mechanical properties	
on Stresses Generated in Iso-Axial Bicrystals. Microstructural Modeling of Recrystallization in Deformed Iron Single Crystals.	1461-1473A 1933-1942A	Crack Bridging by Uncracked Ligaments During Fatigue- Crack Growth in SiC-Reinforced Aluminum-Alloy Compos- ites.	897-908A
OSM process	1999-1942A	Friction Properties of Al—1.5Mg/SiC Particulate Metal-Matrix Composites.	1564-1566A
See Oxygen steel making Oxidation	100 5101	Effects of Microstructure on the Behavior of an Aluminum Alloy and an Aluminum Matrix Composite Tested Under Low Levels of Superimposed Hydrostatic Pressure.	2409-2417A
Transient Oxidation of Single-Crystal β -NiAl. The Mechanism of Oxidation of Ferrous Sulfide (FeS) Pow-	499-518A	Particulate composites, Physical properties Wetting of Ceramic Particulates With Liquid Aluminum Alloys.	
ders in the Range of 648-923K. Oxidation and Nitridation of Alloy 800 H at a Growing Creep Crack and for Unstressed Samples.	661-670B 1541-1551A	I. Experimental Techniques. Wetting of Ceramic Particulates With Liquid Aluminum Alloys.	527-532A
Mass Spectrometric Observations of Metal Oxychlorides Produced by Oxidation—Chlorination Reactions.	1566-1568A	II. Study of Wettability.	533-541A
Thermomechanical Fatigue, Oxidation, and Creep. I. Damage Mechanisms. Thermomechanical Fatigue, Oxidation, and Creep. I. Life Pre-	1755-1767A	Permeability Tribologically-Driven Steady-State Hydrogen Evolution From Mild Steel by Electrochemical Extraction Technique.	557-580A
diction.	1769-1783A	Phase boundary Characterization of the High-Temperature Phase Fields Near	
Oxidation potential See Electrode potentials		Stoichiometric γ-TiAl. Interdiffusion in Ternary Fe—Cr—Al Alloys.	1899-1906A 2767-2781A
Oxidation rate, Heating effects Improving Tantalum's Oxidation Resistance by Al* Ion Implantation.	2101-2108A	Phase boundary, Cooling effects Phase Distributions in Rapidly Solidified Stainless Steels.	2259-2266A
Oxidation reduction potential See Electrode potentials		Phase decomposition See also Eutectoid decomposition Spinodal decomposition	
Oxidation resistance, Coating effects		Fluid Flow in Solidifying Monotectic Alloys.	2517-2527A
Laser-Clad Ni ₇₀ Al ₂₀ Cr ₇ Hf ₃ Alloys With Extended Solid Solution of Hafnium. I. Microstructure Evolution. Laser-Clad Ni ₇₀ Al ₂₀ Cr ₇ Hf ₃ Alloys With Extended Solid Solution of Hafnium. II. Oxidation Behavior.	2267-2277A 2489-2497A	Phase decomposition, Heating effects Phase Decomposition of Rapidly Solidified Fe—Mn—Al—C Austentitic Alloys.	205-214A
Oxidation resistance, Heating effects	2405-2451 K	Phase diagram reactions See also Austenitizing	
Improving Tantalum's Oxidation Resistance by Al* Ion Implantation. Oxides	2101-2108A	Eutectoid decomposition Martensitic transformations Phase decomposition	
See Aluminum oxide Carbon dioxide		Spinodal decomposition Physical Metallurgy of Metastable BCC Lanthanide—	
Oxidizing		Magnesium Alloys for R = Lanthanum, Gadolinium and Dysprosium.	1575-1583A
See Oxidation Oxygen, Alloying additive		Solidification of the Nickel-Base Superalloy 718: a Phase Diagram Approach.	2866-2868A
Combined Effects of Oxygen and Hydrogen on Tensile Properties of a Nb—10 at.% V Alloy.	273-278A	Phase diagrams sothermal Particle Growth in Two-Phase Titanium Alloys.	39-54A
Oxygen, Impurities		The Thermodynamic Activities of Copper and Iron in the Sys- tem Copper—Iron—Platinum at 1300°C.	127-135B
Study of the Hydrogen Internal Friction Peak in Nb—10 at.% V in the Presence of Oxygen. Oxygen, Quaternary systems	1215-1219A	An Experimental Technique for the Rapid Determination of Binary Phase Diagrams: the Al—Mg System. High Temperature Reaction Zone Growth in Tungsten Fiber	197-203A
A Study of the Thermodynamics and Phase Relationships of the Fe—Co—S—O Quaternary System.	1523-1532A	Reinforced Superalloy Composites. I. Application of the Moving Boundary Equations.	255-266A
Oxygen conversion processes See Oxygen steel making		Freezing Diagrams. I. Development and Implications for Glass Formability.	287-297A
Oxygen steel making	000 000	Freezing Diagrams. II. Comparison With Experimental Observation and Relevance to Crystallization of Metallic Glass.	299-309A 334-337A
Steel Dissolution in Quiescent and Gas Stirred Fe/C Melts. Oxynitriding	363-374B	Solubility of Vanadium in α and β Titanium. The Solubility of Hydrogen in Solid Binary Aluminum— Lithium Alloys	523-533B
See Ion nitriding		Lithium Alloys. The Mechanism of Oxidation of Ferrous Sulfide (FeS) Powders in the Range of 648-923K.	
Pack carburizing The Effects of Surface Hardening on Fracture Toughness of Carburized Steel.	519-525A	Activities of Boron in the Binary Fe—B, Co—B, and Cu—B Melts.	705-710B
Packing (crystal density)	U.J GEON	Determination of the Fe—Ni Phase Diagram Below 400°C. Some Phase-Diagram Aspects of the Manganese—Carbon	719-725A
See Crystal structure Parameters		System. Metastable Phase Equilibria in the Lead—Tin Alloy System. I.	747-754B
See Lattice parameters Welding parameters		Experimental. Metastable Phase Equilibria in the Lead—Tin Alloy System.	785-794A 795-803A
Partial pressure The Thermodynamic Activities of Copper and Iron in the Sys-	407	II. Thermodynamic Modeling. Formation of Metastable Structures and Amorphous Phases in Plutonium-Based Systems Using the Sputtering Tech-	
tem Copper—Iron—Platinum at 1300°C.	127-135B	nique.	013-023A

Dissolution of Reactive Strontium-Containing Alloys in Liquid		Resistivity	
Aluminum and A356 Melts.	815-831B	Solid solubility	
Intermetallic Compound Layer Growth at the Interface of Solid Refractory Metals Molybdenum and Niobium With		Solubility Surface tension	
Molten Aluminum. Standard Gibbs Energies of Formation of the Carbides of	825-836A	Thermal expansion Thermal stability	
Chromium by EMF Measurements.	911-917B	Vapor pressure	
Thermodynamic Properties of the Co—W—C System. Mass Spectrometric Study of the Partial Phase Diagram of	935-956A	Viscosity Wettability	
the Fe—Ge System Above 1050°C.	975-976A	Piles (nuclear)	
Structure of As-Cast Aluminum Matrix Composite Containing Ni ₃ Al-Type Intermetallic Ribbons.	1153-1161A	See Nuclear reactors	
Phase Diagrams in Materials Science. Phase Diagrams in Materials Science.	1295-1323A 1295-1323B	Pistons, Materials selection Friction Properties of Al—1.5Mg/SiC Particulate Metal-Matrix	
The Microstructural Details of β-Sn Precipitation in a 5Sn-		Composites.	1564-1566A
95Pb Solder Alloy. A Study of the Thermodynamics and Phase Relationships of	1325-1333A	Pitting (corrosion), Cooling effects	
the Fe—Co—S—O Quaternary System. Microstructure Evolution in TiAl Alloys With Boron Additions:	1523-1532A	Microstructure and Corrosion Behavior of As-Cast and Heat- Treated Al—4.5 wt.% Cu—2.0 wt.% Mn Alloys.	2499-2516A
Conventional Solidification. Characterization of the High-Temperature Phase Fields Near	1847-1859A	Plasma arc casting See Casting	
Stoichiometric γ-TiAl. Improved Ductility of Ni ₃ Si by Microalloying With Boron or	1899-1906A	Plasma arc melting	
Carbon. The Evolution of Microstructure in the Undercooled Zn—Sn	2025-2032A	The Kinetics of Nitrogen Absorption and Desorption From a Plasma Arc by Molten Iron.	175-185B
Entrained Droplets. A Note on the Ag—Au—Ge Equilibrium Phase Diagram.	2109-2115A 2167-2170A	Plasma arc plating	
Phase Equilibria of the AI—Li Binary System. Microstructure and Corrosion Behavior of As-Cast and Heat-	2247-2258A	See Plasma spraying Plasma arc spraying	
Treated Al-4.5 wt.% Cu-2.0 wt.% Mn Alloys.	2499-2516A	See Plasma spraying	
Fluid Flow in Solidifying Monotectic Alloys. Phase Equilibria in the Al—Fe—C System: Isothermal Sec-	2517-2527A	Plasma arc torches	
tions 1550-2300°C.	2703-2706A	Effects of Particle Loading on a Reduced Pressure Induc- tively Coupled Radio Frequency Plasma Torch.	949-958B
Interdiffusion in Ternary Fe—Cr—Al Alloys. The Microstructure of Rapidly Solidified Ti—Fe Melt-Spun	2767-2781A	Plasma jet spraying	***************************************
Ribbons.	2841-2845A	See Plasma spraying	
Phase ratio, Alloying effects The Microstructure of Chromium—Tungsten Steels.	373-382A	Plasma processing See also Plasma arc melting	
Phase ratio, Composition effects		Plasma spraying	
The Influence of Carbon Content on Austenite—Ferrite Mor- phology in Fe—Mn—Al Weld Metals.	2559-2561A	The Role of Transport Phenomena in the Plasma Synthesis of Fine Particles: the Production of Silicon Powder.	243-250B
Phase stability	2009-2001A	Kinetics of Layer Growth and Multiphase Diffusion in Ion-	
Phase Stability by the Artificial Concentration Wave Method.	357-362A	Nitrided Titanium.	1819-1832A
The Mechanism of Oxidation of Ferrous Sulfide (FeS) Pow- ders in the Range of 648-923K.	661-670B	Plasma spraying Particle Melting in High Temperature Supersonic Low Pres-	
Phase Diagrams in Materials Science.	1295-1323A	sure Plasma Jets. Plasma Spraying of Ceramic Particles in Argon—Hydrogen	251-262B
Phase Diagrams in Materials Science.	1295-1323B	D.C. Plasma Jets: Modeling and Measurements of Particles	
Phase structure See Solid phases		in Flight Correlation With Thermophysical Properties of Sprayed Layers.	263-276B
Phase transformations		Effects of Particle Loading on a Reduced Pressure Induc-	
See also Allotropic transformation Austenitizing		tively Coupled Radio Frequency Plasma Torch.	949-958B
Martensitic transformations		Plastic deformation Elastic Limits and Microplastic Response in Ultrahigh	
The Bainite Transformation in a Silicon Steel. Calculation of the Product Phase Grain Edge Length and	324-334A	Strength Carbon Steels. Cavitation Behavior of an Al—Cu Eutectic Alloy During Su-	188-191A
Quadruple Points per Unit Volume During Solid State Transformations.	349-355A	perplastic Deformation.	453-462A
Phase Transformations at Steel/IN625 Clad Interfaces.	665-681A	The Effect of Small Plastic Deformation and Annealing on the Properties of Polycrystals. I. Experimental Observations.	471-477A
Bainite Formation in a Silver—Cadmium Alloy. The Role of Boundary Conditions in Modeling the Elastic Fields Around a Misfitting Precipitate.	1169-1174A	The Effect of Small Plastic Deformation and Annealing on the Properties of Polycrystals. II. Theoretical Model for the	
Fields Around a Misfitting Precipitate.	1277-1279A	Transformation of Nonequilibrium Grain Boundaries.	479-484A
Phase transformations, Cooling effects Precipitation Behavior of MnS During δ/γ Transformation in		The Development of Plastic Failure Modes in Crystalline Ma- terials: Shear Bands in FCC Polycrystals.	579-593A
Fe—Si Alloys.	1375-1383A	Real-Time X-Ray Diffraction investigation of Metal Deforma- tion.	595-604A
Phase transformations, Diffusion effects Similarity Solutions for Phase-Change Problems.	225-235A	New Ultrasonic Methods for Measuring Deformation and	
Phases (state of matter)	225-235A	Fracture Related Material States. Fracture and Fatigue Crack Propagation in a Nickel-Base Me-	611-618A
See Intermetallic phases		tallic Glass. Calculation of the Forming Limit Diagram.	1395-1409A 1975-1987A
Metastable phases Solid phases		Large-Strain Deformation of Aluminum Single Crystals at Ele-	1010 10011
Phosphorus, Alloying elements		vated Temperature as a Test of the Geometric—Dynamic- Recrystallization Concept.	2182-2185A
Effect of Phosphorus on the Formation of Retained Austenite and Mechanical Properties in Silicon-Containing Low-		Plastic flow	
Carbon Steel Sheet.	437-445A	Deformation of Rapidly Solidified Dispersion Strengthened Titanium Alloys.	875-887A
Photo oxidation		The Rate Dependence and Microstructure of High-Purity Sil-	
See Oxidation		ver Deformed to Large Strains Between 0.16 and 0.30 T _m . Particle Bonding, Annealing Response, and Mechanical	2001-2010A
Photodissociation See Dissociation		Properties of Dynamically Consolidated Type 304 Stainless Steel Powders.	2449-2457A
Photography See Stereophotography		Effects of Changes in Strain Path on Work Hardening in Cubic Metals.	2471-2482A
Physical chemistry		Simulation of Static and Deformation-Enhanced Grain Growth Effects on Superplastic Ductility.	2783-2792A
Physical Chemistry of the Carbothermic Reduction of Alumina in the Presence of a Metallic Solvent. II. Measure-		Plastic strain	-100 E10EA
ments of Kinetics of Reaction.	161-173B	See Plastic deformation	
Discussion of "Thermodynamic Consistency of the Interac- tion Parameter Formalism".	434-439B	Plasticity See also Superplasticity	
Physical metallurgy		The Effects of Hold Time and Frequency on Crack Growth in	4707
Physical Metallurgy of Metastable BCC Lanthanide— Magnesium Alloys for R = Lanthanum, Gadolinium and		Alloy 800H at 650°C. Mechanical Properties of Thin Films.	1727-1734A 2217-2245A
Dysprosium.	1575-1583A	Plate metal, Crystal lattices	
Physical properties See Coercive force		A Comparison of Ultrasonic and X-Ray Determinations of	2431-2447A
Curie temperature		Texture in Thin Copper and Aluminum Plates. Plating	E-101-2-44/A
Density Diffusivity			
		See Silver plating	
Miscibility Permeability		See Silver plating Platinum, Ternary systems The Thermodynamic Activities of Copper and Iron in the Sys-	

See Platinum		Precipitates, Microstructure Phase Transformations in the Al—Li—Hf and Al—Li—Ti	
Piutonium base alloys, Phases (state of matter)		Systems.	999-1019A
Formation of Metastable Structures and Amorphous Phases in Plutonium-Based Systems Using the Sputtering Tech- nique.	813-823A	Precipitation Influence of Precipitate Morphology on Intermediate Temperature Creep Properties of a Nickel-Base Superalloy Single	
Point defects		Crystal. Precipitation of Silicon in Aluminum—Silicon: a Calorimetric	133-141A
See also Interstitial impurities		Analysis of Liquid-Quenched and Solid-Quenched Alloys	1207-1214A
Point defects, Radiation effects Tracer Diffusion. Reaction Rate Theory Perspectives on Some Problems in	2577-2582A	Calculation of the $Ti(C_{\nu}N_{1-\nu})-Ti_{4}C_{2}S_{2}-MnS-Austenite}$ Equilibrium in Titanium-Bearing Steels. In Situ Observations of Chemically Induced Grain-Boundary Migration and Discontinuous Precipitation in the	1361-1374A
Materials Science.	2583-2598A	Aluminum—Zinc System.	1593-1600A
Pole figures Characterization of Formability in Cold-Rolled Steel Sheets Using Electromagnetic Acoustic Transducers. A Comparison of Ultrasonic and X-Ray Determinations of	2385-2392A	A Mass Transport Theory for Interphase Precipitation With Application to Vanadium Steels. Correction to "A Mass Transport Theory for Interphase Pre- cipitation With Application to Vanadium Steels".	1647-1655A 1647-1655A
Texture in Thin Copper and Aluminum Plates.	2431-2447A	Precipitation, Cooling effects	
Pole figures, Microstructural effects The Role of Grain Size and Strain in Work Hardening and Texture Development.	2803-2810A	The Microstructural Details of β -Sn Precipitation in a 5Sn— 95Pb Solder Alloy. Precipitation Behavior of MnS During δ/γ Transformation in	1325-1333A
Poling		Fe—Si Alloys.	1375-1383A
See Deoxidizing		Precipitation, Deformation effects Austenite Recrystallization and Carbonitride Precipitation in	
Pollution abatement Thermogravimetric Study of Lead Sulfide Chlorination Be-		Niobium Microalloyed Steels. A Creep Technique for Monitoring MnS Precipitation in Sill-	25-38A
tween 783-953K. The Selective Oxidation of Mixed Metal Sulfides With Lime in	87-96B	con Steels.	2707-2715A
the Presence of Steam Without Emitting Sulfur-Containing Pollutants.	237-242B	Precipitation, Heating effects The Influence of Annealing in the Ferrite-Plus-Austenite Phase Field on the Stability of Vanadium Carbide Precipi-	
Pores See Porosity		tates. The Microstructure of Selected Annealed Vanadium-Base Al-	237-245A
Porosity		loys.	1927-1932A
Wetting of Ceramic Particulates With Liquid Aluminum Alloys. I. Experimental Techniques.	527-532A	Carbide Precipitation During Stage I Tempering of Fe-Ni-C Martensites.	2749-2765A
Ultrasonic and Magnetic Analyses of Porosity in Iron Com-		Precipitation, Radiation effects	
pacts. Effect of Oxygen on Tungsten Filament Sag Kinetics.	571-578A 1144-1146A	Reaction Rate Theory Perspectives on Some Problems in Materials Science.	2583-2598A
Porous materials, Nondestructive testing Ultrasonic and Magnetic Analyses of Porosity in Iron Com-	571-578A	Precipitation, Welding effects Weld Thermal Cycles and Precipitation Effects in Ti—V- Containing HSLA Steels.	2093-2100A
pacts. Positron annihilation	3/1-3/6A	Precipitation hardening	2093-2100A
A Research on Hydrogen Cracking in α -Iron.	2379-2384A	See also Strain aging	
Positrons See Antiparticles		Structure and Properties of a β Solution Treated, Quenched, and Aged Silicon-Bearing Near-α Titanium Alloy. Eddy Current Analysis of Precipitation Kinetics in Aluminum	55-62A
Potassium, Dopants The Microstructure of Rolled and Annealed Tungsten Rod.	1669-1686A	Alloys. Nucleation Kinetics of Titanium Carbonitride in Microalloyed	605-610A
Pots (electrolytic) See Electrolytic cells	1000 10001	Austenite. A Small-Angle Neutron Scattering Study of the Kinetics of Phase Separation in a Supersaturated Ni—12.5 at.% Si	689-697A
Powder compacts		Alloy. Phase Transformations in the Al—Li—Hf and Al—Li—Ti	699-710A
See also Sintered compacts Powder compacts, Mechanical properties		Systems. Influence of Precipitates on the Mechanical Response and	999-1019A
Microstructure and Tensile Properties of Fe-40 at.% Al Al-	4704 47444	Substructure Evolution of Shock-Loaded and Quasi- Statically Deformed Al—Li—Cu Alloys.	1061-1075A
loys With C, Zr, Hf, and B Additions. Microstructures and Mechanical Properties of Explosively	1701-1714A	Atom-Probe Analysis of GP Zones in an Al-1.7 at.% Cu	
Consolidated Titanium Powder With a Pressure Medium.	2831-2839A	Alloy. The Influence of Copper Precipitation and Plastic Deforma-	1585-1591A
Powder compacts, Nondestructive testing Ultrasonic and Magnetic Analyses of Porosity in Iron Com- pacts.	571-578A	tion Hardening on the Impact-Transition Temperature of Rolled Structural Steels. Spinodal Decomposition During Aging of Fe—Ni—C Mar-	1657-1668A
Powder metallurgy		tensites. Solidification of the Nickel-Base Superalloy 718: a Phase Dia-	2717-2737A
See Sintering (powder metallurgy)		gram Approach.	2866-2868A
Powder metallurgy parts, Mechanical properties Evidence of a Thin Sheet Toughening Mechanism in Al— Fe—X Alloys.	155-164A	Precipitation hardening, Alloying effects Microstructure and Tensile Properties of Fe—40 at.% Al Alloys With C, Zr, Hf, and B Additions.	1701-1714A
Crack Bridging by Uncracked Ligaments During Fatigue- Crack Growth in SiC-Reinforced Aluminum-Alloy Compos-		Characterization of Titanium Carbosulfide Precipitation in Ti- tanium Microalloyed Steels.	1907-1915A
ites. Confirmation of a Thin Sheet Toughening Mechanism and	897-908A	Precipitation and Fine Structure in Medium-Carbon Vanadium	
Anisotropic Fracture in Al—Fe—X Alloys.	2337-2344A	and Vanadium/Niobium Microalloyed Steels. Precipitation hardening alloys, Mechanical properties	2279-2288A
Powder technology See Sintering (powder metallurgy)		Mechanism of Cyclic Softening and Fracture of a Nickel-Base γ '-Strengthened Alloy Under Low-Cycle Fatigue.	2793-2801A
Powdering Flow Separation and Liquid Rundown in a Gas-Atomization		Precipitation hardening steels See also Maraging steels	
Process. Influence of Gas Flow on Performance of "Confined" Atomization Nozzles.	613-622B 833-843B	Precipitation hardening steels, Corrosion On Crack Closure of Precipitation Hardened Steels in Aque-	
Powders See Alloy powders		ous Solution. Precipitation heat treatment	1055-1059A
Metal powders		See Precipitation hardening	
Precious metal alloys See Silver base alloys		Preferred orientation Experimental Deformation Textures of OFE Copper and 70:30 Brass From Wire Drawing, Compression, and Tor-	
Precious metals See also Gold		sion. A Comparison of Ultrasonic and X-Ray Determinations of	125-131A
Platinum Silver		Texture in Thin Copper and Aluminum Plates.	2431-2447A
Precious metals, Irradiation		Pressing	
Tracer Diffusion.	2577-2582A	See Hot isostatic pressing	
Precipitates Microstructure of High-Tensile Strength Brasses Containing Silicon and Manganese.	1199-1206A	Pressure See Hydrostatic pressure Partial pressure Vapor pressure	
The Role of Boundary Conditions in Modeling the Elastic Fields Around a Misfitting Precipitate.	1277-1279A	Pressure casting	
An Elastically Induced Morphological Instability of a Misfitting Precipitate.	2171-2175A	Microstructural Observations of Pressure Cast Ni ₂ Al/Al ₂ O ₃ and Ni/Al ₂ O ₃ Composites.	2159-2166A

Pressure vessels, Corrosion Fatigue Crack Growth Behavior of Pressure Vessel Steels		Analytical Electron Microscopy Studies of Radiation Damage. In Situ Studies of Ion Irradiation Effects in an Electron Micro-	2663-2671A
and Submerged Arc Weldments in a High-Temperature Pressurized Water Environment.	2069-2085A	scope. Mechanical Property Changes in Ion-Irradiated Metals. I.	2673-2680A
Pressure vessels, Materials selection		Ni—Cu Alloys. Mechanical Property Changes in Ion-Irradiated Metals. II.	2681-2687A
Effects of Manganese, Silicon, and Purity on the Design of 3.5NiCrMoV, 1CrMoV, and 2.25Cr—1Mo Bainitic Alloy	0407 00404	High-Strength Cu—Ni—Be Alloy.	2689-2693A
Steels. Pressure welding See Diffusion welding	2197-2212A	Radiators, Soldering The Microstructural Details of β -Sn Precipitation in a 5Sn— 95Pb Solder Alloy.	1325-1333A
Pressurized water reactors		Radioactive tracera	0577 05004
The Effects of Heat Treatment on the Sensitization and SCC Behavior of Inconel 600 Alloy.	1077-1088A	Tracer Diffusion. Radiocrystallography	2577-2582A
Fatigue Crack Growth Behavior of Pressure Vessel Steels and Submerged Arc Weldments in a High-Temperature Pressurized Water Environment.	2069-2085A	See Crystallography Rapid solidification	
Pressurized water reactors, Materials selection	2000 200011	Phase Decomposition of Rapidly Solidified Fe—Mn—Al—C Austenitic Alloys.	205-214A
The Effects of Heat Treatment on the Chromium Depletion, Precipitation Evolution, and Corrosion Resistance of Inco- nel Alloy 690.	2057-2067A	Extended Solid Solution and Nonequilibrium Phase Diagram for Ni—Al Alloy Formed During Laser Cladding. Metastable Phase Equilibria in the Lead—Tin Alloy System. I.	363-371A
Prestraining Transient Tensile Behavior of Interstitial-Free Steel and 70/30		Experimental. Metastable Phase Equilibria in the Lead—Tin Alloy System.	785-794A
Brass Following Plane-Strain Deformation.	1483-1493A	II. Thermodynamic Modeling. Synthesis and Structural Aspects of Quasicrystals in Mg—	795-803A
Process control Prediction of Weld Pool and Reinforcement Dimensions of		Al—Ag System: Mg4AleAg. Deformation of Rapidly Solidified Dispersion Strengthened	805-812A
GMA Welds Using a Finite-Element Model.	937-947B	Titanium Alloys. Effects of Particle Loading on a Reduced Pressure Induc-	875-887A
Propagation See Crack propagation		tively Coupled Radio Frequency Plasma Torch. Structural Study of Electrodeposited Aluminum—Manganese	949-958B
Properzi process See Continuous casting		Alloys. Correction to "Deformation Mechanisms of a Rapidly Solidi-	1351-1359A
Prosthetics		fied AI—8.8Fe—3.7Ce Alloy*. Characterization of the High-Temperature Phase Fields Near	1713-1719A
See also Surgical implants		Stoichiometric y-TiAl. Phase Distributions in Rapidly Solidified Stainless Steels.	1899-1906A 2259-2266A
Prosthetics, Mechanical properties Grain Egression: a New Mechanism of Fatigue-Crack Initiation in Ti—6AI—4V.	1715-1725A	Confirmation of a Thin Sheet Toughening Mechanism and Anisotropic Fracture in Al—Fe—X Alloys. Fatigue Crack Propagation in Rapidly Solidified Aluminum Al-	2337-2344A
Protective atmospheres See Controlled atmospheres		loys at 25°C and 300°C.	2425-2430A
Protective coatings		The Microstructure of Rapidly Solidified Ti—Fe Melt-Spun Ribbons.	2841-2845A
Carbon Fibers Coated With Chromium Carbide Using the Liq- uid Metal Transfer Agent Technique.	165-170A	Rare earth alloys See Dysprosium base alloys	
Laser-Clad Nir ₀ Al ₂₀ Cr ₇ Hf ₃ Alloys With Extended Solid Solution of Hafnium. II. Oxidation Behavior.	2489-2497A	Gadolinium base alloys Lanthanum base alloys	
Protective coatings, Microstructure	2100 210111	Rare earth metals	
Laser-Clad Ni ₇₀ Al ₂₀ Cr ₇ Hf ₃ Alloys With Extended Solid Solution of Hafnium. I. Microstructure Evolution.	2267-2277A	See Lanthanum Neodymium	
Pulse echo technique See Ultrasonic testing		Rare gases Fluid Flow and Bath Temperature Destratification in Gas- Stirred Ladles.	603-611B
Pyrometallurgy Electrochemical Transport Through a Lime—Silica—Alumina		Rayleigh waves	000-0110
Slag. Critical Evaluation of the Thermochemical Properties of Lead	31-37B	See Surface waves Reaction kinetics	
Sulfates. A Molten Salt Process for Producing Neodymium and	77-85B	Kinetic Study of the Dissolution of Cuprite in Oxyacid Solu-	E72 E00D
Neodymium—Iron Alloys. Quantitative analysis	805-813B	tions. Studies of the Interfacial Kinetics of the Reaction of CO ₂ With	573-580B
Interface Characterization of Fiber-Reinforced Ni ₃ Al Matrix	0450 04604	Liquid Iron—Nickel Alloys at 1873K. Reactions (chemical)	755-756B
Composites. A Statistically Significant Experimental Technique for Investi-	2459-2469A	See also Carbothermic reactions Chlorination	
gating Microsegregation in Cast Alloys. Quantitative metallography	2529-2533A	Deoxidizing Desulfurizing	
Determination of Carbide and Matrix Compositions in High- Speed Steels by Analytical Electron Microscopy.	2695-2701A	Interface reactions Nitrification	
Stereo (Scanning Electron Microscopy) Section Fractography of Isolated Cleavage Regions in Nuclear Vessel Steels.	2862-2866A	Oxidation Preparation of Submicron Titanium Nitride Powder by Vapor-	
Quasicrystalline structure, Cooling effects	EUOE-EUOUA	Phase Reactions. Kinetic Study of the Dissolution of Cuprite in Oxyacid Solu-	493-497B
Synthesis and Structural Aspects of Quasicrystals in Mg— Al—Ag System: Mg ₄ Al ₆ Ag.	805-812A	tions. Chemical Potentials of Oxygen for Fayalite—Quartz—Iron	573-580B
Quaternary systems, Phases (state of matter) A Study of the Thermodynamics and Phase Relationships of		and Fayalite—Quartz—Magnetite Equilibria. Reactions (chemical), Composition effects	679-685B
the Fe—Co—S—O Quaternary System. Quenching (cooling)	1523-1532A	Studies of the Interfacial Kinetics of the Reaction of CO ₂ With Liquid Iron—Nickel Alloys at 1873K.	755-756B
See Quenching and tempering Rapid solidification		Reactions (nuclear)	
Water quenching		See Neutron scattering Reactivity (chemical)	
The Influence of Tempering Temperature on Small Fatigue Crack Behavior Monitored With Surface Acoustic Waves in		See Activity (chemical)	
Quenched and Tempered 4140 Steel.	1257-1265A	Reactor vessels (nuclear) See Nuclear reactors	
Duplex Treatment of High-Strength Steels. Quenching stresses	1687-1699A	Reactors See Fast nuclear reactors	
See Residual stress		Light water reactors Nuclear fusion reactors	
Radiation See Ion beams		Nuclear reactors Nuclear reactors Pressurized water reactors	
Radiation damage Tracer Diffusion.	2577 2522	Recovery	
Reaction Rate Theory Perspectives on Some Problems in Materials Science.	2577-2582A	An Elastic Recovery Test for Recrystallization. The Rate Dependence and Microstructure of High-Purity Sil-	1885-1887A
Fluctuations in Composition in Dilute Alloys Under Irradiation.	2583-2598A 2599-2607A	ver Deformed to Large Strains Between 0.16 and 0.30 T _m .	2001-2010A
Irradiation-Enhanced and Induced Mass Transport. Ion Beam Characterization and Treatment.	2619-2626A 2627-2636A	Recrystallization See also Grain refinement	
Atom Probe Field-Ion Microscope: a Technique for Microstructural Characterization of Irradiated Materials on the Atomic Scale.	2651-2661A	Development of Rolling Textures in Aluminum Alloy 3004 Subjected to Varying Hot-Rolling Deformation. An Elastic Recovery Test for Recrystallization.	1495-1507A 1885-1887A
	200 - E001N	Lianto Houstory root for Houry stantactors.	A TOOL COOL

The Rate Dependence and Microstructure of High-Purity Silver Deformed to Large Strains Between 0.16 and 0.30 ${\rm T_m}.$	2001-2010A	Phase Diagrams in Materials Science. Mechanical Properties of Thin Films. Reaction Rate Theory Perspectives on Some Problems in	1295-1323B 2217-2245A
Recrystallization, Deformation effects Austenite Recrystallization and Carbonitride Precipitation in		Materials Science. Ion Beam Characterization and Treatment.	2583-2598A 2627-2636A
Niobium Microalloyed Steels. Modeling Recrystallization Kinetics in a Deformed Iron Single Crystal.	25-38A 391-401A	Impurity-Defect Interactions in Radiation Hardening and Em- brittlement in BCC Metals.	2637-2649A
The Microstructure of Rolled and Annealed Tungsten Rod. Recrystallization Microstructure in Cold-Rolled Aluminum	1669-1686A	Atom Probe Field-Ion Microscope: a Technique for Microstructural Characterization of Irradiated Materials on	0074 00044
Composites Reinforced by Silicon Carbide Whiskers. Microstructural Modeling of Recrystallization in Deformed	1743-1753A	the Atomic Scale. Rheological properties	2651-2661A
Iron Single Crystals. Large-Strain Deformation of Aluminum Single Crystals at Ele-	1933-1942A	See Viscosity Roasters	
vated Temperature as a Test of the Geometric—Dynamic- Recrystallization Concept.	2182-2185A	See Hearth roasters	
Recrystallization, Heating effects Alloy Partitioning in Ti—24Al—11Nb by Analytical Electron		Roasting Thermogravimetric Study of Lead Sulfide Chlorination Between 783-953K.	87-96B
Microscopy. The Microstructures of Strip-Cast Low-Carbon Steels and	1139-1142A	A Heat-Transfer Model for the Rotary Kiln. I. Pilot Kiln Trials. A Heat-Transfer Model for the Rotary Kiln. II. Development of	391-402B
Their Response to Thermal Processing. Red hardness	1191-1198A	the Cross-Section Model. Development of a Mathematical Model for Multihearth Roast-	403-419B
See Hardness Redox potential		ers. Roll pressing	925-935B
See Electrode potentials		See Rolling	
Reduction (chemical) See also Flash smelting		Rolling See also Cold rolling	
The Influence of Weathering on the Reduction of Ilmenite With Carbon.	735-745B	Controlled rolling Hot rolling	
A Molten Salt Process for Producing Neodymium and Neodymium—Iron Alloys.	805-813B	Workability of 1045 Spheroidized Steel Under Superimposed Hydrostatic Pressure.	1735-1741A
Reduction (electrolytic) See also Electrowinning		Microstructural Modeling of Recrystallization in Deformed Iron Single Crystals.	1933-1942A
Fundamental Studies on the Continuous Electrolytic Reduc- tion of Uranyl Sulfate.	337-343B	Rolling mill rolls, Service life Roll Cooling and its Relationship to Roll Life.	2305-2320A
Reduction (metal working) See Cold rolling		Rolling texture Development of Rolling Textures in Aluminum Alloy 3004	
Hot rolling Rolling		Subjected to Varying Hot-Rolling Deformation. Rolls	1495-1507A
Wire drawing Reduction potential		See Rolling mill rolls	
See Electrode potentials Refining		Rotary kilns See Kilns	
See also Electrorefining Vacuum refining		Rotors, Materials selection Effects of Manganese, Silicon, and Purity on the Design of	
Electrochemical Transport Through a Lime—Silica—Alumina Slag.	31-37B	 Steels. 	2197-2212A
Kinetics of Deoxidation of Liquid Copper by Graphite Parti- cles During Submerged Injection.	187-196B	Rotors, Mechanical properties Degradation of Mechanical Properties of Cr—Mo—V and	
Re-Evaluation of Standard Free Energy of Formation of CaO. Physical Characteristics of Gas Jets Injected Vertically Up-		2.25Cr—1Mo Steel Components After Long-Term Service at Elevated Temperatures.	87-97A
ward Into Liquid Metal. Refractory alloys	595-601B	The Influences of Impurity Content, Tensile Strength, and Grain Size on In-Service Temper Embrittlement of CrMoV	
See Molybdenum base alloys Niobium base alloys		Steels. Mechanism of Cyclic Softening and Fracture of a Nickel-Base	2345-2354A
Tungsten base alloys Vanadium base alloys		γ'-Strengthened Alloy Under Low-Cycle Fatigue. Roughing (rolling)	2793-2801A
Refractory metal compounds See Molybdenum compounds		See Hot rolling Roughness	
Niobium compounds Refractory metals		Mode I Stress Intensity Factors Induced by Fracture Surface Roughness Under Pure Mode III Loading: Application to the	
See Chromium Molybdenum		Effect of Loading Modes on Stress Corrosion Crack Growth.	1989-1999A
Niobium Tantalum		Rubber springs	
Tungsten Vanadium		See Springs (elastic) Rupture strength	
Relaxation See also Stress relaxation		See Creep rupture strength Seg	
Parameters Affecting Sag Resistance in Spring Steels.	1951-1959A	Effect of Oxygen on Tungsten Filament Sag Kinetics. Parameters Affecting Sag Resistance in Spring Steels.	1144-1146A 1951-1959A
Tin-Based Reactive Solders for Ceramic/Metal Joints.	919-924B	Saline water See Salt water	
Resistance welds See Welded joints		Salt water, Environment	
Resistivity, Microstructural effects The Electrical Conductivity of Cast Al—Si Alloys in the Range 2-12.6 wt.% Silicon.	383-389A	Microstructure and Corrosion Behavior of As-Cast and Heat- Treated Al—4.5 wt.% Cu—2.0 wt.% Mn Alloys. Saturation (material composition)	2499-2516A
Resonance testing See Ultrasonic testing	000 000	See Supersaturation Scandium compounds, Reactions (chemical)	
Retained austenite Fracture and Fatigue Crack Propagation Properties of Har-		Standard Enthalpy of Formation of Sc ₅ Si ₅ .	879-8828
dened 52100 Steel. Retained austenite, Alloying effects	1961-1973A	Scanning electron microscopy Stereo (Scanning Electron Microscopy) Section Fractography of Isolated Cleavage Regions in Nuclear Vessel Steels.	2862-2866A
Effect of Phosphorus on the Formation of Retained Austenite and Mechanical Properties in Silicon-Containing Low-		Scanning transmission electron microscopy See Scanning electron microscopy	
Carbon Steel Sheet. Retained austenite, Heating effects	437-445A	Scattering See Neutron scattering	
The Effects of Surface Hardening on Fracture Toughness of Carburized Steel.	519-525A	Scrap See also Steel scrap	
Revaporization See Vaporizing		Scrap, Recovering	
Reviews The Extractive Metallurgist in an Emerging World of Materi-		Determination of the Standard Gibbs Energies of Formation of Ca ₃ As ₂ , Ca ₃ Sb ₂ , and Ca ₃ Bi ₂ .	863-870B
als. Phase Diagrams in Materials Science.	291-313B 1295-1323A	Scrap steel See Steel scrap	
			0.00

Correlation of Microstructure and Creep Stages in the (100)		See Strip steel	
Oriented Superalloy SRR99 at 1253K. [011] Twinning in Fe—Ni—C Martensites.	1233-1238A 2739-2747A	Shielded arc welding	
Season cracking See Stress corrosion cracking		See Gas metal arc welding Gas tungsten arc welding Shielded metal arc welding	
Seeding See Nucleation		Submerged arc welding Shielded metal arc welding	
Seeding (inoculation)		Lower Acicular Ferrite.	1811-1818A
See Inoculation		Shock loading Influence of Precipitates on the Mechanical Response and	
Segregations Formation of Hot-Top Segregation in Steel Ingot and Effect of Steel Compositions.	723-730B	Substructure Evolution of Shock-Loaded and Quasi- Statically Deformed Al—Li—Cu Alloys.	1061-1075A
Hydrogen Embrittlement of Iron—Nickel Alloys. Segregations, Alloying effects	1475-1482A	Short arc welding See Gas metal arc welding	
Effect of Thermal Conditions and Alloying Constituents (Ni,Cr) on Macrosegregation in Continuously Cast High-	893-910B	Sigma hard facing See Gas metal arc welding	
Carbon (0.8%), Low-Alloy Steel. Improved Ductility of Ni ₃ Si by Microalloying With Boron or		Sigma welding See Gas metal arc welding	
Carbon. The Effect of Chromium on Antimony and Nickel Grain Boundary Segregation in Iron.	2025-2032A 2170-2171A	Silicides, Reactions (chemical) Standard Enthalpy of Formation of Sc ₅ Si ₃ .	879-882B
Segregations, Cooling effects	047.0504	Silicon	
On the Influence of Coarsening on Microsegregation. A Statistically Significant Experimental Technique for Investi- gating Microsegregation in Cast Alloys.	247-253A 2529-2533A	Effect of Phosphorus on the Formation of Retained Austenite and Mechanical Properties in Silicon-Containing Low- Carbon Steel Sheet.	437-445A
Efficient Estimation of Diffusion During Dendritic Solidifica- tion.	2847-2856A	Silicon, Alloying elements	
Segregations, Radiation effects Fluctuations in Composition in Dilute Alloys Under Irradiation.	2599-2607A	Carbide Stability Diagrams in 2.25Cr—1Mo Steels. X-Ray Diffraction Line Profile Analysis on the Microstructure of Cold-Worked Face-Centered Cubic Cu—Ge—Si Alloys:	1561-1564A
Self diffusion See Diffusion		Effects of Dilute Solutes Silicon and Germanium.	1883-1885A
Semicontinuous casting See Continuous casting		Silicon, Impurities Effects of Manganese, Silicon, and Purity on the Design of 3.5NiCrMoV, 1CrMoV, and 2.25Cr—1Mo Bainitic Alloy	
Semikilling		Steels. Silicon, Powder technology	2197-2212A
See Deoxidizing Senaitivity		The Role of Transport Phenomena in the Plasma Synthesis of Fine Particles: the Production of Silicon Powder.	243-250B
See Notch sensitivity		Silicon, Solubility	240 2000
Sensitizing The Effects of Heat Treatment on the Sensitization and SCC Behavior of Inconel 600 Alloy.	1077-1088A	Precipitation of Silicon in Aluminum—Silicon: a Calorimetric Analysis of Liquid-Quenched and Solid-Quenched Alloys.	1207-1214A
The Effects of Heat Treatment on the Chromium Depletion, Precipitation Evolution, and Corrosion Resistance of Inco- nel Alloy 690.	2057-2067A	Silicon carbide, Brazing The Interaction of Reaction-Bonded Silicon Carbide and Inco- nel 600 With a Nickel-Based Brazing Alloy.	1803-1810A
Behavior of Sensitized AISI Types 321 and 347 Austenitic Stainless Steels in Hydrogen.	2187-2190A	Silicon carbide, Composite materials Crack Bridging by Uncracked Ligaments During Fatigue-	
Shaft kilns See Kilns		Crack Growth in SiC-Reinforced Aluminum-Alloy Compos- ites.	897-908A
Shape		Friction Properties of Al—1.5Mg/SiC Particulate Metal-Matrix Composites.	1564-1566A
See Particle shape Shape memory, Microstructural effects		Recrystallization Microstructure in Cold-Rolled Aluminum Composites Reinforced by Silicon Carbide Whiskers.	1743-1753A
Correction to "Microstructural Refinement of W—Ni—Fe Heavy Alloys by Alloying Additions".	3100-3103A	Deformation of Whisker-Reinforced Metal-Matrix Compos- ites Under Changing Temperature Conditions. Effects of Microstructure on the Behavior of an Aluminum	2355-2368A
Shape memory alloys, Microstructure Nonbasal Plane Defects in 18R Martensite and the Effect of Abnormal Defects on Thermoelastic Martensitic Transfor-		Alloy and an Aluminum Matrix Composite Tested Under Low Levels of Superimposed Hydrostatic Pressure. Interface Characterization of Fiber-Reinforced Ni ₃ Al Matrix	2409-2417A
mation. Shear properties	1631-1636A	Composites.	2459-2469A
See also Shear strength Shear stress		Silicon compounds See also Silicon carbide Silicon nitride	
Shear properties, Pressure effects Microvoid Formation During Shear Deformation of Ultrahigh Strength Steels.	143-153A	Silicon compounds, Mechanical properties Improved Ductility of Ni ₃ Si by Microalloying With Boron or Carbon.	2025-2032A
Shear strength Study of the Interface and its Effect on Mechanical Properties		Silicon iron See Silicon steels	
of Continuous Graphite Fiber-Reinforced 201 Aluminum. Shear stress	727-739A	Silicon nitride, Soldering Tin-Based Reactive Solders for Ceramic/Metal Joints.	919-924B
Elastic Interaction Stresses. II. The Influence of Orientation on Stresses Generated in Iso-Axial Bicrystals.	1461-1473A	Silicon steels See also Electrical steels	010 0240
Shear stress, Corrosion effects The Influence of Hydrogen on Atomic Binding Energy, Critical Slip Shear Stress, and Fatigue Crack Propagation Rate of Aluminum Single Crystals.	921-924A	Silicon steels, Directional solidification Precipitation Behavior of MnS During δ/γ Transformation in Fe—Si Alloys.	1375-1383A
Shear stress, Temperature effects The Correlation Between the Temperature Dependence of		Silicon steels, Mechanical properties Parameters Affecting Sag Resistance in Spring Steels.	1951-1959A
the CRSS and the Formation of Superlattice-Intrinsic Stacking Faults in the Nickel-Base Superalloy PWA 1480. Sheet metal, Coating	1888-1889A	Silicon steels, Metal working A Creep Technique for Monitoring MnS Precipitation in Sili-	
The Effects of Silicon on the Reaction Between Solid Iron and Liquid 55 wt.% AI—Zn Bath.	543-555A	con Steels. Silicon steels, Phase transformations The Bainite Transformation in a Silicon Steel.	2707-2715A 324-334A
Sheet metal, Forming Experimental Investigation and Finite Element Modeling of Hemispherically Stretched Steel Sheet.	1500.4504.4	Silver, Structural hardening The Rate Dependence and Microstructure of High-Purity Sil-	324-334A
Determination of Friction Coefficient for Sheet Materials Under Stretch-Forming Conditions.	1509-1521A 2179-2182A	ver Deformed to Large Strains Between 0.16 and 0.30 T _m .	2001-2010A
Characterization of Formability in Cold-Rolled Steel Sheets Using Electromagnetic Acoustic Transducers.		Silver, Ternary systems A Note on the Ag—Au—Ge Equilibrium Phase Diagram.	2167-2170A
Sheet metal, Mechanical properties Evidence of a Thin Sheet Toughening Mechanism in Al-		Silver base alloys, Phase transformations Bainite Formation in a Silver—Cadmium Alloy.	1169-1174A
Fe—X Alloys. Confirmation of a Thin Sheet Toughening Mechanism and Anisotropic Fracture in Al—Fe—X Alloys.	155-164A	Silver base alloys, Reactions (chemical) Direct Activity Measurements in Liquid Ag—Cu Alloys Using a Valved Knudsen Cell—Mass Spectrometer System.	845-852B

Silver plating Electrode Mass Transfer Under Conditions of Natural and		Slabbing (rolling) See Rolling	
Forced Convection.	21-29B	Slag fuming	
Silvering See Silver plating		High-Pressure Coal Injection in Zinc Stag Furning. The Extractive Metallurgist in an Emerging World of Materials.	227-235B
Simulation See also Computer simulation		Slagging	291-313B
Flow Separation and Liquid Rundown in a Gas-Atomization Process.	613-622B	Thermodynamics of the Na ₂ O—P ₂ O ₅ System. Study on the Foaming of CaO—SiO ₂ —FeO Slags. I. Foaming	197-204B
Thermosolutal Convection During Dendritic Solidification of Alloys. I. Linear Stability Analysis. Solidification Microstructures Near the Limit of Absolute Sta-	711-721B	Parameters and Experimental Results. Study on the Foaming of CaO—SiO ₂ —FeO Slags. II. Dimen- sional Analysis and Foaming in Iron and Steelmaking Pro-	509-514B
bility.	769-777A	cesses.	515-521B
Vacuum Distillation of Copper Matte to Remove Lead, Arsenic, Bismuth, and Antimony.	793-804B	Slags Electrochemical Transport Through a Lime—Silica—Alumina	
Primary Dendrite Spacing and the Effect of Off-Axis Heat Flow.	969-973A	Slag. The Sulfur Partition Ratio With Fe—C _{SAT} Melts and the Sul-	31-37B
Modeling of Multidimensional Solidification of an Alloy. Deformation of Whisker-Reinforced Metal-Matrix Compos-	1833-1845A	fide Capacity of CaO—SiO ₂ —Na ₂ O—(Al ₂ O ₃) Slags. Optical Basicity and the Thermodynamic Properties of Slags.	71-76B 113-118B
ites Under Changing Temperature Conditions. Fluid Flow in Solidifying Monotectic Alloys. Dendritic Growth in the Carbon Tetrabromide and Hexachlor-	2355-2368A 2517-2527A	Sulfide Capacities of MnO—SiO ₂ Slags. Determination of the Standard Glibbs Energies of Formation of Ca ₃ As ₂ , Ca ₃ Sb ₂ , and Ca ₃ Bi ₂ .	137-140B 863-870B
ethane System. The Role of Grain Size and Strain in Work Hardening and	2567-2570A	Slip	000 0.02
Texture Development.	2803-2810A	See also Cross slip Slip planes	
Single crystals, Corrosion The Influence of Hydrogen on Atomic Binding Energy, Critical		Latent Hardening in Cyclic Deformation of Copper Single Crystals.	759-767A
Slip Shear Stress, and Fatigue Crack Propagation Rate of	921-924A	An Analysis of the Low Temperature, Low and High Strain- Rate Deformation of Ti—6AI—4V.	863-874A
Aluminum Single Crystals. The Influence of Water Vapor on the Fatigue Crack Propaga-		Slip, Deformation effects	003-014A
tion Kinetics in Pure Aluminum Single Crystals. The SCC of Single Crystals of β Brass in Water: Fractography	925-933A	Dislocation Structures of Monocrystalline Copper in Cyclic Latent Hardening.	2033-2045A
and Crystallography.	1439-1444A	Slip planes	2000-20101
Single crystals, Crystal growth Microstructural Modeling of Recrystallization in Deformed Iron Single Crystals. Single crystals, Crystal lattices	1933-1942A	The Development of Plastic Failure Modes in Crystalline Ma- terials: Shear Bands in FCC Polycrystals. Fracture and Fatigue Crack Propagation in a Nickel-Base Me- tallic Glass.	579-593A 1395-1409A
Hydrogen Retrapping After Thermal Charging of Hydrogen in	1700 10004	Slip planes, Deformation effects	1000-14004
Iron Single Crystal. Single crystals, Mechanical properties Influence of Precipitate Morphology on Intermediate Temper-	1793-1802A	Shear Band Formation in Heavily Cold Rolled 70-30 Brass. Smelting	1267-1275A
ature Creep Properties of a Nickel-Base Superalloy Single	133-141A	See also Flash smelting Physical Chemistry of the Carbothermic Reduction of Alu-	
Crystal. Latent Hardening in Cyclic Deformation of Copper Single		mina in the Presence of a Metallic Solvent. II. Measure- ments of Kinetics of Reaction.	161-173B
Crystals. The Correlation Between the Temperature Dependence of	759-767A	High-Pressure Coal Injection in Zinc Stag Furning.	227-235B
the CRSS and the Formation of Superlattice-Intrinsic Stacking Faults in the Nickel-Base Superalloy PWA 1480. Large-Strain Deformation of Aluminum Single Crystals at Ele-	1888-1889A	Snoek effect, Impurity effects Study of the Hydrogen Internal Friction Peak in Nb—10 at.% V in the Presence of Oxygen.	1215-1219A
vated Temperature as a Test of the Geometric—Dynamic- Recrystallization Concept.	2182-2185A	Soft annealing See Annealing	
Single crystals, Microstructure Observations of Directional Gamma Prime Coarsening Dur-		Soft solders	
ing Engine Operation.	683-688A	See Solders	
Single crystals, Nondestructive testing Acoustic Emission From Intergranular Subcritical Crack Growth.	637-648A	Softening Mechanism of Cyclic Softening and Fracture of a Nickel-Base γ '-Strengthened Alloy Under Low-Cycle Fatigue.	2793-2801A
Single crystals, Oxidation		Softening, Radiation effects Mechanical Property Changes in Ion-Irradiated Metals. II.	
Transient Oxidation of Single-Crystal β-NiAl. Single crystals, Rolling	499-518A	High-Strength Cu—Ni—Be Alloy.	2689-2693A
Modeling Recrystallization Kinetics in a Deformed Iron Single Crystal.	391-401A	Solders, Alloy development Tin-Based Reactive Solders for Ceramic/Metal Joints.	919-924B
Single crystals, Structural hardening A Small-Angle Neutron Scattering Study of the Kinetics of		Solders, Microstructure The Microstructural Details of β -Sn Precipitation in a 5Sn—95Pb Solder Alloy.	1325-1333A
Phase Separation in a Supersaturated Ni—12.5 at.% Si Alloy.	699-710A	Solid phases	
Single crystals, Welding Development of Microstructures in Fe—15Ni—15Cr Single		Phase Equilibria in the Al—Fe—C System: Isothermal Sections 1550-2300°C.	2703-2706A
Crystal Electron Beam Welds.	1125-1138A	Solid solubility	
Sintered compacts, Microstructure Reaction Sintering of an Fe—6 wt.% B—48 wt.% Mo Alloy		Formation of Metastable Structures and Amorphous Phases in Plutonium-Based Systems Using the Sputtering Tech-	
in the Presence of Liquid Phases.	17-24A	nique. Phase Structure of the Ti ₁ Cu _{1—x} Fe _x System.	813-823A 981-985A
Sintering See also Sintering (powder metallurgy)		Precipitation of Silicon in Aluminum—Silicon: a Calorimetric Analysis of Liquid-Quenched and Solid-Quenched Alloys.	1207-1214A
Mathematical Model of the Stack Region of a Commercial Lead Blast Furnace.	97-106B	Calculation of the Ti(C _y N _{1—y})—Ti ₄ C ₂ S ₂ —MnS—Austenite Equilibrium in Titanium-Bearing Steels.	1361-1374A
A Heat-Transfer Model for the Rotary Kiln. I. Pilot Kiln Trials. A Heat-Transfer Model for the Rotary Kiln. II. Development of the Cross-Section Model.	391-402B	Characterization of Titanium Carbosulfide Precipitation in Ti- tanium Microalloyed Steels.	1907-1915A
Sintering (powder metallurgy)	4004100	Solid solubility, Alloying effects Carbide Stability Diagrams in 2.25Cr—1Mo Steels.	1561-1564A
See also Liquid phase sintering Particle Bonding, Annealing Response, and Mechanical Properties of Dynamically Consolidated Type 304 Stainless		Solid solubility, Composition effects The Solubility of Hydrogen in Solid Binary Aluminum— Lithium Alloys.	523-533B
Steel Powders. Microstructures and Mechanical Properties of Explosively	2449-2457A	Solid solubility, Cooling effects	
Consolidated Titanium Powder With a Pressure Medium.	2831-2839A	Extended Solid Solution and Nonequilibrium Phase Diagram for Ni—Al Alloy Formed During Laser Cladding.	363-371A
Sites See Lattice sites		Solid solutions, Microstructure	
Size distribution (particle)		The Electrical Conductivity of Cast Al—Si Alloys in the Range 2-12.6 wt.% Silicon.	383-389A
See Particle size distribution Skull casting		Solidification	
See Casting		See also Directional solidification Rapid solidification	** ***
Slab casting, Field effects Electromagnetic Refining of Aluminum Alloys by the CREM Process II Specific Practical Problems and Their Solu-		A Mathematical Model of the Spray Deposition Process. Equilibrium Partition Coefficients in Iron-Based Alloys. The Growth of Tubular or Vermicular Structures in Organic	71-85A 149-160B
Process. II. Specific Practical Problems and Their Solutions.	631-643B	Monotectic Systems.	171-177A

	the Influence of Coarsening on Microsegregation. sezing Diagrams. I. Development and Implications for	247-253A	Spheroidal iron See Nodular iron	
(Blass Formability. Lezing Diagrams. II. Comparison With Experimental Obser-	287-297A	Spheroidal structure	
Mc	ation and Relevance to Crystallization of Metallic Glass. deling of Equiaxed Microstructure Formation in Casting.	299-309A 311-322A	See Nodular graphitic structure	
On	Identification of the Nucleant in Commercially Pure Alumi-		Spinodal decomposition The Effects of Elastic Stress on the Kinetics of Ostwald Ri-	
Fo	num Castings Inoculated With < 0.15% Titanium. rmation of Hot-Top Segregation in Steel Ingot and Effect of	564-566A	pening: the Two-Particle Problem. An Investigation on the Mechanism of 475°C Embrittlement in	1175-1189A
Eff	Steel Compositions. Sect of Thermal Conditions and Alloying Constituents	723-730B	High-Chromium Ferritic Stainless Steel. Spinodal Decomposition During Aging of Fe—Ni—C Mar-	2563-2567A
8	Ni,Cr) on Macrosegregation in Continuously Cast High- carbon (0.8%), Low-Alloy Steel. mary Dendrite Spacing and the Effect of Off-Axis Heat	893-910B	tensites.	2717-2737A
Pri	mary Dendrite Spacing and the Effect of Off-Axis Heat		Spinodal decomposition, Heating effects Carbide Precipitation During Stage I Tempering of Fe—Ni—	
Mo	flow. Ideling of Multidimensional Solidification of an Alloy.	969-973A 1833-1845A	C Martensites.	2749-2765A
	e Evolution of Microstructure in the Undercooled Zn—Sn Entrained Droplets.	2109-2115A	Sponginess See Porosity	
Mi	crostructural Development During Solidification of Stain-	2117-2131A	Spraying	
So	ess Steel Alloys. ildification of High-Speed Tool Steels. onel 718: a Solidification Diagram.	2133-2148A 2149-2158A	See also Plasma spraying A Mathematical Model of the Spray Deposition Process.	71-85A
Fa	cated—Nonfaceted Dandritic Transitions During the Laser		Spring alloys	,,,,,,,,,,,,,,,,,,,,,,,,,,,,,,,,,,,,,,,
AS	rocessing of Al ₂ O ₃ —1.0 wt.% MgO. Statistically Significant Experimental Technique for Investi-	2191-2194A	See Spring steels	
So	ating Microsegregation in Cast Alloys. lidification of the Nickel-Base Superalloy 718: a Phase Dia-	2529-2533A	Spring steels, Mechanical properties Parameters Affecting Sag Resistance in Spring Steels.	1951-1959A
9	ram Approach.	2866-2868A	Springs (elastic), Mechanical properties	
Solub Se	e also Solid solubility		Parameters Affecting Sag Resistance in Spring Steels.	1951-1959A
	mments on the Solubility of Carbon in Molten Aluminum. in billity of Vanadium in α and β Titanium.	191A 334-337A	Sputtering See also lon beam sputtering	
Th	e Solubility of Hydrogen in Molten Aluminum Alloys. e Solubility of Titanium Diboride in Aluminum.	1785-1791A 2185-2187A	Formation of Metastable Structures and Amorphous Phases in Plutonium-Based Systems Using the Sputtering Tech-	
Ph	ase Equilibria in the Al—Fe—C System: Isothermal Sec-		nique.	813-823A
	ions 1550-2300°C. ility, Cooling effects	2703-2706A	Squeezing See Compressing	
Pri	ecipitation Behavior of MnS During 8/y Transformation in	1075 10004	Stability	
	e—Si Alloys.	1375-1383A	See also Phase stability Thermal stability	
Th	ion annealing e Effects of Heat Treatment on the Chromium Depletion, gracinitation Evolution, and Corresion Resistance of Inc.		Thermosolutal Convection During Dendritic Solidification of Alloys. I. Linear Stability Analysis.	711-721B
	Precipitation Evolution, and Corrosion Resistance of Inco- nel Alloy 690.	2057-2067A	Solidification Microstructures Near the Limit of Absolute Sta- bility.	769-777A
Solut	ion hardening e Solution strengthening		An Elastically Induced Morphological Instability of a Misfitting	2171-2175A
	ien hest treatment		Precipitate. Stacking faults	21/1-21/5A
Se	e also Solution annealing ructure and Properties of a β Solution Treated, Quenched,		The Correlation Between the Temperature Dependence of the CRSS and the Formation of Superlattice-Intrinsic	
	and Aged Silicon-Bearing Near-α Titanium Alioy. oy Partitioning in Ti—24Al—11Nb by Analytical Electron	55-62A	Stacking Faults in the Nickel-Base Superalloy PWA 1480.	1888-1889A
1	Vicroscopy.	1139-1142A	Effects of Changes in Strain Path on Work Hardening in Cubic Metals.	2471-2482A
Solut	ion strengthening imputer Simulation of Solid Solution Strengthening in FCC		Stacking faults, Alloying effects Effect of Copper on the Strength of AISI 316 Stainless Steel.	421-429A
	Alloys. I. Friedel and Mott Limits.	1411-1418A	X-Ray Diffraction Line Profile Analysis on the Microstructure	421-423A
4	Imputer Simulation of Solid Solution Strengthening in FCC Alloys. II. At Absolute Zero Temperature.	1419-1428A	of Cold-Worked Face-Centered Cubic Cu—Ge—Si Alloys: Effects of Dilute Solutes Silicon and Germanium.	1883-1885A
Solut	ion strengthening, Structural hardening imputer Simulation of Thermally Activated Dislocation Mo-		Stacking faults, Deformation effects	
~	ion. III. In FCC Solid Solutions.	1429-1437A	An X-Ray Diffraction Line Profile Analysis in Cold-Worked Hexagonal (ζ)-Phase and Mixed ($\alpha + \zeta$)-Phase of	
Solve	Ints hysical Chemistry of the Carbothermic Reduction of Alu-		Copper—Germanium Alloys. Stainless steels	1142-1144A
1	mina in the Presence of a Metallic Solvent. II. Measure-	404 4700	See also Austenitic stainless steels	
Co	nents of Kinetics of Reaction. prection to "Thermodynamic Consistency of the Interaction	161-173B	Ferritic stainless steels Martensitic stainless steels	
	Parameter Formalism".	269-275B	Stainless steels, Casting	
Se	is (metallurgical) ie Solid solubility		Two-Dimensional Model for Twin-Roll Continuous Casting. Microstructural Development During Solidification of Stain-	381-390B
Sorp	tion e Absorption (material)		less Steel Alloys.	2117-2131A
36	Adsorption		Stainless steels, Nondestructive testing New Ultrasonic Methods for Measuring Deformation and	
Spac	Description e environment		Fracture Related Material States. Stainless steels, Phases (state of matter)	611-618A
Mi	xed Gravity Mode Grwoth During Directional Dendritic So- idification Aboard the KC-135.	1004 10004	Phase Distributions in Rapidly Solidified Stainless Steels.	2259-2266A
Spac		1284-1286A	Static casting See Casting	
Pr	imary Dendrite Spacing and the Effect of Off-Axis Heat Flow.	969-973A	Static fatigue	
	savage Fracture in Pearlitic Eutectoid Steel.	2321-2335A	See Creep rupture strength	
Spail	ing Il Cooling and Its Relationship to Roll Life.	2305-2320A	Static pressure See Hydrostatic pressure	
Spec	ific density	2000 2020	Statistical analysis	
	e Density		A Statistically Significant Experimental Technique for Investi- gating Microsegregation in Cast Alloys.	2529-2533A
	e Density		Steel constituents See also Bainite	
	ific resistance		Ferrite	
	ific volume		Martensite Retained austenite	0000 0000
	ee Density		Phase Distributions in Rapidly Solidified Stainless Steels. Steel constituents, Cooling effects	2259-2266A
	ific weight # Density		Microstructural Development During Solidification of Stain-	2117-2131A
Spec	tra		less Steel Alloys. Steel converters	2117-2131A
Spet	Mass spectra		See Bottom blown converters	
S	se Zinc		Steel making See also Oxygen steel making	
Sphe	eroidal graphite Pe Nodular graphitic structure		The Sulfur Partition Ratio With Fe—C _{SAT} Melts and the Sulfide Capacity of CaO—SiO ₂ —Na ₂ O—(Al ₂ O ₃) Slags.	71-76B

Re-Evaluation of Standard Free Energy of Formation of CaO. Morphology of Nonmetallic Inclusions Using Silicon, Aluminum, and Calcium—Silicon Alloy in Steel Melt.	431-433B 581-594B	Strain aging Impurity-Defect Interactions in Radiation Hardening and Embrittlement in BCC Metals.	2637-2649A
Physical Characteristics of Gas Jets Injected Vertically Up- ward Into Liquid Metal.	595-601B	Strain hardening Latent Hardening in Cyclic Deformation of Copper Single	2007 201011
Fluid Flow in Pachuca (Air-Agltated) Tanks. I. Laboratory- Scale Experimental Measurements.	781-791B	Crystals. Martensite Formation, Strain Rate Sensitivity, and Deforma-	759-767A
Decarburization Kinetics of Liquid Fe—C _{sat} Alloys by CO ₂ . Determination of the Standard Gibbs Energies of Formation of Ba ₃ P ₂ and Ba ₃ (PO ₄) ₂ .	853-861B 871-877B	tion Behavior of Type 304 Stainless Steel Sheet. Shear Band Formation in Heavily Cold Rolled 70-30 Brass. The Influence of Copper Precipitation and Plastic Deforma-	1239-1246A 1267-1275A
Steel scrap Steel Dissolution in Quiescent and Gas Stirred Fe/C Melts.	363-374B	Rolled Structural Steels.	1657-1668A
Steels	303-3745	Calculation of the Forming Limit Diagram. The Rate Dependence and Microstructure of High-Purity Sil-	1975-1987A
See also Aluminum killed steels Austenitic stainless steels		ver Deformed to Large Strains Between 0.16 and 0.30 T _m . Dislocation Structures of Monocrystalline Copper in Cyclic	2001-2010A
Bearing steels Carbon manganese steels		Latent Hardening. Theory of Work-Hardening Applied to Stages III and IV.	2033-2045A 2393-2397A
Carbon steels		Effects of Changes in Strain Path on Work Hardening in Cubic Metals.	2471-2482A
Chromium molybdenum steels Chromium molybdenum vanadium steels		The Role of Grain Size and Strain in Work Hardening and Texture Development.	2803-2810A
Chromium steels Electrical steels		Strain hardening, High temperature effects	2000-2010N
Ferritic stainless steels Galvanized steels		On Microstructure—Property Correlation of Thermally Aged Type 316L Stainless Steel Weld Metal.	1115-1124A
High speed tool steels High strength low alloy steels		Strain hardening, Stress effects	
Hot work tool steels Killed steels		Determination of Effective Stress and Dislocation Velocity in the Deformation of Titanium-Doped Iron.	1029-1036A
Maraging steels Martensitic stainless steels		Strain hardening, Temperature effects	
Molybdenum steels		Analysis of the Temperature Dependence of Strain- Hardening Behavior in High-Strength Steel.	2819-2829A
Nickel chromium molybdenum steels Nickel chromium steels		Strain rate Combined Effects of Oxygen and Hydrogen on Tensile Prop-	
Nickel molybdenum steels Nickel steels		erties of a Nb10 at.% V Alloy. Cavitation Behavior of an AlCu Eutectic Alloy During Su-	273-278A
Precipitation hardening steels Silicon steels		perplastic Deformation. An Analysis of the Low Temperature, Low and High Strain-	453-462A
Spring steels Stainless steels		Rate Deformation of Ti—6AI—4V.	863-874A
Titanium steels Tool steels		Deformation of Rapidly Solidified Dispersion Strengthened Titanium Alloys. The Delta of Control of Strengthened In the Strengthened Correction	875-887A
Vanadium steels		The Role of Crack Tip Strain Rate in the Stress Corrosion Cracking of High Strength Steels in Water.	889-895A
Steels, Casting Fluid Flow and Bath Temperature Destratification in Gas-		Effect of Deformation on Ferrite Nucleation and Growth in a Plain Carbon and Two Microalloyed Steels.	987-998A
Stirred Ladles.	603-611B	Influence of Precipitates on the Mechanical Response and Substructure Evolution of Shock-Loaded and Quasi-	
Steels, Forming Determination of Friction Coefficient for Sheet Materials		Statically Deformed Al—Li—Cu Alloys. Martensite Formation, Strain Rate Sensitivity, and Deforma-	1061-1075A
Under Stretch-Forming Conditions. Characterization of Formability in Cold-Rolled Steel Sheets	2179-2182A	tion Behavior of Type 304 Stainless Steel Sheet. Correction to "Deformation Mechanisms of a Rapidly Solidi-	1239-1246A
Using Electromagnetic Acoustic Transducers.	2385-2392A	fied Al—8.8Fe—3.7Ce Alloy". Calculation of the Forming Limit Diagram.	1713-1719A 1975-1987A
Steels, Heat treatment Dependence of the Lattice Parameter of γ' Iron Nitride,		The Rate Dependence and Microstructure of High-Purity Silver Deformed to Large Strains Between 0.16 and 0.30 T _m .	2001-2010A
Fe ₄ N _{1-x} , on Nitrogen Content; Accuracy of the Nitrogen Absorption Data.	1533-1539A	Stress Relaxation of an AISI 1080 Steel. Deformation of Whisker-Reinforced Metal-Matrix Compos-	2011-2015A
Steels, Irradiation Fluctuations in Composition in Dilute Alloys Under Irradiation.	2599-2607A	ites Under Changing Temperature Conditions. Simulation of Static and Deformation-Enhanced Grain	2355-2368A
Impurity-Defect Interactions in Radiation Hardening and Em- brittlement in BCC Metals.	2637-2649A	Growth Effects on Superplastic Ductility. Effect of Strain Rate on Martensitic Transformation During	2783-2792A
Steels, Mechanical properties	2037-2049A	Uniaxial Testing of AISI-304 Stainless Steel. Discussion of "Correlations of Microstructure With Dynamic	2857-2859A
Transient Tensile Behavior of Interstitial-Free Steel and 70/30 Brass Following Plane-Strain Deformation.	1483-1493A	and Quasi-Static Fracture in a Plain Carbon Steel".	2860-2862A
Steels, Metallography		Strain rate, Stress effects Determination of Effective Stress and Dislocation Velocity in	4000 40004
Atom Probe Field-Ion Microscope: a Technique for Microstructural Characterization of Irradiated Materials on		the Deformation of Titanium-Doped Iron. Strengthening (solution)	1029-1036A
the Atomic Scale.	2651-2661A	See Solution strengthening	
Steels, Refining Determination of the Standard Gibbs Energies of Formation	200 2700	Stress aging See Strain aging	
of Ca ₃ As ₂ , Ca ₃ Sb ₂ , and Ca ₃ Bi ₂ . Steels, Rolling	863-870B	Stress analysis Elastic Interaction Stresses, II. The Influence of Orientation	
Roll Cooling and its Relationship to Roll Life.	2305-2320A	on Stresses Generated in Iso-Axial Bicrystals.	1461-1473A
Steels, Welding Mechanisms of Inclusion Formation in Al—Ti—Si—Mn De-		Stress corrosion cracking Effects of Near-Tip Inhomogeneities on Scattering of Ultra-	
oxidized Steel Weld Metals.	1335-1349A	sonic Waves by Cracks. The Role of Crack Tip Strain Rate in the Stress Corrosion	619-626A
Stereography See Stereophotography		Cracking of High Strength Steels in Water. The Effects of Heat Treatment on the Sensitization and SCC	889-895A
Stereophotography Stereo (Scanning Electron Microscopy) Section Fractography		Behavior of Inconel 600 Alloy. The SCC of Single Crystals of β Brass in Water: Fractography	1077-1088A
of Isolated Cleavage Regions in Nuclear Vessel Steels.	2862-2866A	and Crystallography. Application of Modeling of the Texture Dependence of Envi-	1439-1444A
Stick electrode arc welding See Shielded metal arc welding		ronmentally Assisted Crack Growth of Long and Short Cracks to Zircaloy Fuel Tubing.	1943-1950A
Stirring		Mode I Stress Intensity Factors Induced by Fracture Surface Roughness Under Pure Mode III Loading: Application to the	
See also Electromagnetic stirring Mathematical Modeling of Mixing Phenomena in a Gas		Effect of Loading Modes on Stress Corrosion Crack Growth.	1989-1999A
Stirred Liquid Bath. Fluid Flow and Bath Temperature Destratification in Gas-	53-59B	The Effects of Heat Treatment on the Chromium Depletion,	1909-1999A
Stirred Ladles. On Effective Viscosity Models for Gas-Stirred Ladle Systems.	603-611B 967-969B	Precipitation Evolution, and Corrosion Resistance of Inco- nel Alloy 690.	2057-2067A
Stora Kaldo process		Retrogression and Reaging and the Role of Dislocations in the Stress Corrosion of 7000-Type Aluminum Alloys.	2087-2092A
See Oxygen steel making Storage		Stress corrosion resistance See Corrosion resistance	
See Data storage		Stress intensity	
Strain See also True strain		Mode I Stress Intensity Factors Induced by Fracture Surface Roughness Under Pure Mode III Loading: Application to the	
Experimental Investigation and Finite Element Modeling of Hemispherically Stretched Steel Sheet.	1509-1521A	Effect of Loading Modes on Stress Corrosion Crack Growth.	1989-1999A

Stress relaxation Nucleation Kinetics of Titanium Carbonitride in Microalloyed	689-697A	Superalloys Investigations on the Influence of Internal Nitridation on	1553-1560A
Austenite. Stress Relaxation of an AISI 1080 Steel. A Creep Technique for Monitoring MnS Precipitation in Sili-	2011-2015A	Creep Crack Growth in Alloy 800H. Superalloys, Brazing	1553-1560A
con Steels. Stress relaxation, Microstructural effects	2707-2715A	The Interaction of Reaction-Bonded Silicon Carbide and Inco- nel 600 With a Nickel-Based Brazing Alloy.	1803-1810A
The Effect of Microstructure on Properties and Behaviors of Annealed Fe ₇₈ B ₁₃ Si ₉ Amorphous Alloy Ribbon.	63-70A	Superalloys, Cladding Phase Transformations at Steel/IN625 Clad Interfaces.	665-681A
Stress relieving See Grain refinement		Laser-Clad Ni ₇₀ Al ₂₀ Cr ₇ Hf ₃ Alloys With Extended Solid Solution of Hafnium. I. Microstructure Evolution. Laser-Clad Ni ₇₀ Al ₂₀ Cr ₇ Hf ₃ Alloys With Extended Solid Solu-	2267-2277A
Stress rupture strength		tion of Hafnium. II. Oxidation Behavior.	2489-2497A
See Creep rupture strength		Superalloys, Composite materials High Temperature Reaction Zone Growth in Tungsten Fiber	
Stress strain curves Microvoid Formation During Shear Deformation of Ultrahigh Strength Steels.	143-153A	Reinforced Superalloy Composites. I. Application of the Moving Boundary Equations. High Temperature Reaction Zone Growth in Tungsten Fiber	255-266A
Latent Hardening in Cyclic Deformation of Copper Single Crystats. Shear Band Formation in Heavily Cold Rolled 70-30 Brass.	759-767A 1267-1275A	Reinforced Superalloy Composites. II. Matrix Chemistry Effects.	267-272A
Transient Tensie Behavior of Interstitial-Free Steel and 70/30 Brass Following Plane-Strain Deformation. Stress Relaxation of an AISI 1080 Steel.	1483-1493A 2011-2015A	Superalloys, Corrosion The Effects of Heat Treatment on the Sensitization and SCC	1077-1088A
Stresses	2011-2013A	Behavior of Inconel 600 Alloy. Oxidation and Nitridation of Alloy 800 H at a Growing Creep Crack and for Unstressed Samples.	1541-1551A
See Residual stress Shear stress		Mass Spectrometric Observations of Metal Oxychlorides	
Stress intensity Thermal stresses		Produced by Oxidation—Chlorination Reactions. The Effects of Heat Treatment on the Chromium Depletion, Precipitation Evolution, and Corrosion Resistance of Inco-	1566-1568A
Stretch forming		nel Alloy 690.	2057-2067A
Determination of Friction Coefficient for Sheet Materials Under Stretch-Forming Conditions. Stretching	2179-2182A	Superalloys, Mechanical properties Influence of Precipitate Morphology on Intermediate Temper- ature Creep Properties of a Nickel-Base Superalloy Single	
See also Stretch forming Experimental Investigation and Finite Element Modeling of		Crystal. Correlation of Microstructure and Creep Stages in the (100)	133-141A
Hemispherically Stretched Steel Sheet. Calculation of the Forming Limit Diagram.	1509-1521A 1975-1987A	Oriented Superalloy SRR99 at 1253K. The Effects of Hold Time and Frequency on Crack Growth in	1233-1238A
Effects of Changes in Strain Path on Work Hardening in Cubic Metals.	2471-2482A	Alloy 800H at 650°C. The Correlation Between the Temperature Dependence of	1727-1734A
Strip See Strip steel		the CRSS and the Formation of Superlattice-Intrinsic Stacking Faults in the Nickel-Base Superalloy PWA 1480.	1888-1889A
Strip steel, Casting The Microstructures of Strip-Cast Low-Carbon Steels and	4404 44004	Superalloys, Microstructure Observations of Directional Gamma Prime Coarsening Dur- ing Engine Operation.	683-688A
Their Response to Thermal Processing. Strip steel, Structural hardening	1191-1198A	Superalloys, Structural hardening	
Martensite Formation, Strain Rate Sensitivity, and Deforma- tion Behavior of Type 304 Stainless Steel Sheet.	1239-1246A	Solidification of the Nickel-Base Superalloy 718: a Phase Dia- gram Approach.	2866-2868A
Strontium, Alloying elements The Electrical Conductivity of Cast Al—Si Alloys in the Range		Superalloys, Welding Inconel 718: a Solidification Diagram.	2149-2158A
2-12.6 wt.% Silicon.	383-389A	Supercooling	
Dissolution of Reactive Strontium-Containing Alloys in Liquid			
Aluminum and A356 Melts.	815-831B	The Growth of Tubular or Vermicular Structures in Organic Monotectic Systems. Modeling of Equiaxed Microstructure Formation in Casting.	171-177A 311-322A
Aluminum and A356 Melts. Structural hardening See Precipitation hardening		The Growth of Tubular or Vermicular Structures in Organic Monotectic Systems. Modeling of Equiaxed Microstructure Formation in Casting. Metastable Phase Equilibria in the Lead—Tin Alloy System. I. Experimental.	
Aluminum and A356 Melts. Structural hardening		The Growth of Tubular or Vermicular Structures in Organic Monotectic Systems. Modeling of Equiaxed Microstructure Formation in Casting. Metastable Phase Equilibria in the Lead—Tin Alloy System. I. Experimental. Metastable Phase Equilibria in the Lead—Tin Alloy System. II. Thermodynamic Modeling.	311-322A
Aluminum and A356 Melts. Structural hardening See Precipitation hardening Solution strengthening Strain aging		The Growth of Tubular or Vermicular Structures in Organic Monotectic Systems. Modeling of Equiaxed Microstructure Formation in Casting. Metastable Phase Equilibria in the Lead—Tin Alloy System. I. Experimental. Metastable Phase Equilibria in the Lead—Tin Alloy System. II. Thermodynamic Modeling. The Evolution of Microstructure in the Undercooled Zn—Sn Entrained Droplets.	311-322A 785-794A
Aluminum and A356 Melts. Structural hardening See Precipitation hardening Solution strengthening Strain aging Strain hardening Structural members See I beams Structural shapes		The Growth of Tubular or Vermicular Structures in Organic Monotectic Systems. Modeling of Equiaxed Microstructure Formation in Casting. Metastable Phase Equilibria in the Lead—Tin Alloy System. I. Experimental. Metastable Phase Equilibria in the Lead—Tin Alloy System. II. Thermodynamic Modeling. The Evolution of Microstructure in the Undercooled Zn—Sn Entrained Droplets. Superplasticity Deformation of Whisker-Reinforced Metal-Matrix Compos-	311-322A 785-794A 795-803A 2109-2115A
Aluminum and A356 Melts. Structural hardening See Precipitation hardening Solution strengthening Strain aging Strain hardening Structural members See I beams Structural shapes See I beams Structural chapes See I beams		The Growth of Tubular or Vermicular Structures in Organic Monotectic Systems. Modeling of Equiaxed Microstructure Formation in Casting. Metastable Phase Equilibria in the Lead—Tin Alloy System. I. Experimental. Metastable Phase Equilibria in the Lead—Tin Alloy System. II. Thermodynamic Modeling. The Evolution of Microstructure in the Undercooled Zn—Sn Entrained Droplets. Superplasticity Deformation of Whisker-Reinforced Metal-Matrix Composites Under Changing Temperature Conditions. Simulation of Static and Deformation-Enhanced Grain	311-322A 785-794A 795-803A 2109-2115A 2355-2368A
Aluminum and A356 Melts. Structural hardening See Pracipitation hardening Solution strengthening Strain aging Strain hardening Structural members See I beams Structural shapes See J beams Structures (crystalline) See Acicular structure Crystal structure		The Growth of Tubular or Vermicular Structures in Organic Monotectic Systems. Modeling of Equiaxed Microstructure Formation in Casting. Metastable Phase Equilibria in the Lead—Tin Alloy System. I. Experimental. Metastable Phase Equilibria in the Lead—Tin Alloy System. II. Thermodynamic Modeling. The Evolution of Microstructure in the Undercooled Zn—Sn Entrained Droplets. Superplasticity Deformation of Whisker-Reinforced Metal-Matrix Composites Under Changing Temperature Conditions.	311-322A 785-794A 795-803A 2109-2115A
Aluminum and A356 Melts. Structural hardening See Precipitation hardening Solution strengthening Strain aging Strain hardening Structural members See I beams Structural shapes See I beams Structures (crystalline) See Acicular structure Crystal structure Dendritic structure Equiaxed structure		The Growth of Tubular or Vermicular Structures in Organic Monotectic Systems. Modeling of Equiaxed Microstructure Formation in Casting. Metastable Phase Equilibria in the Lead—Tin Alloy System. I. Experimental. Metastable Phase Equilibria in the Lead—Tin Alloy System. II. Thermodynamic Modeling. The Evolution of Microstructure in the Undercooled Zn—Sn Entrained Droplets. Superplasticity Deformation of Whisker-Reinforced Metal-Matrix Composites Under Changing Temperature Conditions. Simulation of Static and Deformation-Enhanced Grain Growth Effects on Superplastic Ductliity. Supersaturation Metastable Phase Equilibria in the Lead—Tin Alloy System. I.	311-322A 785-794A 795-803A 2109-2115A 2355-2368A 2783-2792A
Aluminum and A356 Melts. Structural hardening See Precipitation hardening Strain aging Strain hardening Strain hardening Structural members See I beams Structural shapes See I beams Structural crystalline) See Accular structure Crystal structure Dendritic structure Equiaxed structure Grain structure Grain structure Graphitic structure Graphitic structure		The Growth of Tubular or Vermicular Structures in Organic Monotectic Systems. Modeling of Equiaxed Microstructure Formation in Casting. Metastable Phase Equilibria in the Lead—Tin Alloy System. I. Experimental. Metastable Phase Equilibria in the Lead—Tin Alloy System. II. Thermodynamic Modeling. The Evolution of Microstructure in the Undercooled Zn—Sn Entrained Droplets. Superplasticity Deformation of Whisker-Reinforced Metal-Matrix Composites Under Changing Temperature Conditions. Simulation of Static and Deformation-Enhanced Grain Growth Effects on Superplastic Ductifity. Supersaturation Metastable Phase Equilibria in the Lead—Tin Alloy System. I. Experimental. Metastable Phase Equilibria in the Lead—Tin Alloy System.	311-322A 785-794A 795-803A 2109-2115A 2355-2368A 2783-2792A 785-794A
Aluminum and A356 Melts. Structural hardening See Precipitation hardening Strain aging Strain aging Strain hardening Structural members See I beams Structural shapes See I beams Structural c(rystalline) See Acicular structure Crystal structure Dendritic structure Equiaxed structure Grain structure Grain structure Graphitic structure Lameliar structure Microstructure Microstructure Microstructure		The Growth of Tubular or Vermicular Structures in Organic Monotectic Systems. Modeling of Equiaxed Microstructure Formation in Casting. Metastable Phase Equilibria in the Lead—Tin Alloy System. I. Experimental. Metastable Phase Equilibria in the Lead—Tin Alloy System. II. Thermodynamic Modeling. The Evolution of Microstructure in the Undercooled Zn—Sn Entrained Droplets. Superplasticity Deformation of Whisker-Reinforced Metal-Matrix Composites Under Changing Temperature Conditions. Simulation of Static and Deformation-Enhanced Grain Growth Effects on Superplastic Ductlifty. Supersaturation Metastable Phase Equilibria in the Lead—Tin Alloy System. I. Experimental. Metastable Phase Equilibria in the Lead—Tin Alloy System. II. Thermodynamic Modeling. Precipitation of Silicon in Aluminum—Silicon: a Calorimetric	311-322A 785-794A 795-803A 2109-2115A 2355-2368A 2783-2792A 785-794A 795-803A
Aluminum and A356 Melts. Structural hardening See Precipitation hardening Solution strengthening Strain aging Strain hardening Structural members See I beams Structural shapes See I beams Structural structure See Acicular structure Crystal structure Dendritic structure Equiaxed structure Grain structure Grain structure Lamellar structure Lamellar structure Microstructure Nodular graphitic structure Quasicrystallines structure		The Growth of Tubular or Vermicular Structures in Organic Monotectic Systems. Modeling of Equiaxed Microstructure Formation in Casting. Metastable Phase Equilibria in the Lead—Tin Alloy System. I. Experimental. Metastable Phase Equilibria in the Lead—Tin Alloy System. I. I. Thermodynamic Modeling. The Evolution of Microstructure in the Undercooled Zn—Sn Entrained Droplets. Superplasticity Deformation of Whisker-Reinforced Metal-Matrix Composites Under Changing Temperature Conditions. Simulation of Static and Deformation-Enhanced Grain Growth Effects on Superplastic Ductility. Supersaturation Metastable Phase Equilibria in the Lead—Tin Alloy System. I. Experimental. Metastable Phase Equilibria in the Lead—Tin Alloy System. II. Thermodynamic Modeling. Precipitation of Silicon in Aluminum—Silicon: a Calorimetric Analysis of Liquid-Quenched and Solid-Quenched Alloys. Surface alloying	311-322A 785-794A 795-803A 2109-2115A 2355-2368A 2783-2792A 785-794A
Aluminum and A356 Melts. Structural hardening See Precipitation hardening Solution strengthening Strain aging Strain hardening Structural members See I beams Structural shapes See I beams Structures (crystalline) See Acicular structure Crystal structure Dendritic structure Equiaxed structure Graphitic structure Graphitic structure Lamellar structure Microstructure Nodular graphitic structure Ouasicrystalline structure Unit cell Subograin boundaries		The Growth of Tubular or Vermicular Structures in Organic Monotectic Systems. Modeling of Equiaxed Microstructure Formation in Casting. Metastable Phase Equilibria in the Lead—Tin Alloy System. I. Experimental. Metastable Phase Equilibria in the Lead—Tin Alloy System. II. Thermodynamic Modeling. The Evolution of Microstructure in the Undercooled Zn—Sn Entrained Droplets. Superplasticity Deformation of Whisker-Reinforced Metal-Matrix Composites Under Changing Temperature Conditions. Simulation of Static and Deformation-Enhanced Grain Growth Effects on Superplastic Ductifity. Supersaturation Metastable Phase Equilibria in the Lead—Tin Alloy System. I. Experimental. Metastable Phase Equilibria in the Lead—Tin Alloy System. II. Thermodynamic Modeling. Precipitation of Silicon in Aluminum—Silicon: a Calorimetric Analysis of Liquid-Quenched and Solid-Quenched Alloys. Surface alloying Improving Tantalum's Oxidation Resistance by Al* Ion Implantation.	311-322A 785-794A 795-803A 2109-2115A 2355-2368A 2783-2792A 785-794A 795-803A
Aluminum and A356 Melts. Structural hardening See Precipitation hardening Strain aging Strain hardening Structural members See I beams Structural shapes See I beams Structural shapes See I beams Structural structure Crystal structure Crystal structure Equiaxed structure Equiaxed structure Grain structure Graphitic structure Graphitic structure Lamellar structure Microstructure Microstructure Nodular graphitic structure Quasicrystalline structure Quasicrystalline structure Unit cell Subgrain boundaries See Grain sub boundaries		The Growth of Tubular or Vermicular Structures in Organic Monotectic Systems. Modeling of Equiaxed Microstructure Formation in Casting. Metastable Phase Equilibria in the Lead—Tin Alloy System. I. Experimental. Metastable Phase Equilibria in the Lead—Tin Alloy System. II. Thermodynamic Modeling. The Evolution of Microstructure in the Undercooled Zn—Sn Entrained Droplets. Superplasticity Deformation of Whisker-Reinforced Metal-Matrix Composites Under Changing Temperature Conditions. Simulation of Static and Deformation-Enhanced Grain Growth Effects on Superplastic Ductlifty. Supersaturation Metastable Phase Equilibria in the Lead—Tin Alloy System. I. Experimental. Metastable Phase Equilibria in the Lead—Tin Alloy System. II. Thermodynamic Modeling. Precipitation of Silicon in Aluminum—Silicon: a Calorimetric Analysis of Liquid-Quenched and Solid-Quenched Alloys. Surface alloying Improving Tantalum's Oxidation Resistance by Al* Ion Im-	311-322A 785-794A 795-803A 2109-2115A 2355-2368A 2783-2792A 785-794A 795-803A 1207-1214A
Aluminum and A356 Melts. Structural hardening See Precipitation hardening Strain aging Strain hardening Structural members See I beams Structural shapes See I beams Structural shapes See I beams Structural structure Crystal structure Crystal structure Equiaxed structure Equiaxed structure Grain structure Grain structure Graphitic structure Lamellar structure Microstructure Nodular graphitic structure Quasicrystalline structure Unit cell Subgrain boundaries See Grain sub boundaries Submerged arc welding Mechanisms of Inclusion Formation in Al—Ti—Si—Mn Deoxidized Steel Weld Metals.		The Growth of Tubular or Vermicular Structures in Organic Monotectic Systems. Modeling of Equiaxed Microstructure Formation in Casting. Metastable Phase Equilibria in the Lead—Tin Alloy System. I. Experimental. Metastable Phase Equilibria in the Lead—Tin Alloy System. II. Thermodynamic Modeling. The Evolution of Microstructure in the Undercooled Zn—Sn Entrained Droplets. Superplasticity Deformation of Whisker-Reinforced Metal-Matrix Composites Under Changing Temperature Conditions. Simulation of Static and Deformation-Enhanced Grain Growth Effects on Superplasticity. Supersaturation Metastable Phase Equilibria in the Lead—Tin Alloy System. I. Experimental. Metastable Phase Equilibria in the Lead—Tin Alloy System. II. Thermodynamic Modeling. Precipitation of Silicon in Aluminum—Silicon: a Calorimetric Analysis of Liquid-Quenched and Solid-Quenched Alloys. Surface alloying Improving Tantalum's Oxidation Resistance by Al* Ion Implantation.	311-322A 785-794A 795-803A 2109-2115A 2355-2368A 2783-2792A 785-794A 795-803A 1207-1214A 2101-2108A
Aluminum and A356 Melts. Structural hardening See Precipitation hardening Solution strengthening Strain aging Strain hardening Structural members See I beams Structural shapes See I beams Structural shapes See I beams Structural crystalline) See Acicular structure Crystal structure Equiaxed structure Equiaxed structure Graphitic structure Graphitic structure Graphitic structure Lamellar structure Hicrostructure Microstructure Nodular graphitic structure Quasicrystalline structure Unit cell Subgrain boundaries See Grain sub boundaries See Grain sub boundaries Submerged arc welding Mechanisms of Inclusion Formation in Al—Ti—Si—Mn Deoxidizad Steel Weld Metals. Fatigue Crack Growth Behavior of Pressure Vessel Steels and Submerged Arc Weldments in a High-Temperature Pressurized Water Environment. Weld Thermal Cycles and Precipitation Effects in Ti—V-	815-831B 1335-1349A 2069-2085A	The Growth of Tubular or Vermicular Structures in Organic Monotectic Systems. Modeling of Equiaxed Microstructure Formation in Casting. Metastable Phase Equilibria in the Lead—Tin Alloy System. I. Experimental. Metastable Phase Equilibria in the Lead—Tin Alloy System. II. Thermodynamic Modeling. The Evolution of Microstructure in the Undercooled Zn—Sn Entrained Droplets. Superplasticity Deformation of Whisker-Reinforced Metal-Matrix Composites Under Changing Temperature Conditions. Simulation of Static and Deformation-Enhanced Grain Growth Effects on Superplastic Ductlify. Supersaturation Metastable Phase Equilibria in the Lead—Tin Alloy System. I. Experimental. Metastable Phase Equilibria in the Lead—Tin Alloy System. II. Thermodynamic Modeling. Precipitation of Silicon in Aluminum—Silicon: a Calorimetric Analysis of Liquid-Quenched and Solid-Quenched Alloys. Surface alloying Improving Tantalum's Oxidation Resistance by Al* Ion Implantation. Surface analysis (chemical) Ion Beam Characterization and Treatment. Surface analysis (chemical) Two-Dimensional Finite Difference Analysis of Shape Instabilities in Plates.	311-322A 785-794A 795-803A 2109-2115A 2355-2368A 2783-2792A 785-794A 795-803A 1207-1214A 2101-2108A
Aluminum and A356 Melts. Structural hardening See Precipitation hardening Solution strengthening Strain aging Strain hardening Structural members See I beams Structural shapes See I beams Structures (crystalline) See Acicular structure Crystal structure Equiaxed structure Equiaxed structure Graphitic structure Graphitic structure Graphitic structure Unit cell Subgrain boundaries See Grain sub boundaries See Grain sub boundaries Submerged arc welding Mechanisms of Inclusion Formation in AI—TI—SI—Mn Deoxidized Steel Weld Metals. Fatigue Crack Growth Behavior of Pressure Vessel Steels and Submerged Arc Weldments in a High-Temperature Pressurized Water Environment. Weld Thermal Cycles and Precipitation Effects in Ti—V-Containing HSLA Steels. Submerged arc welds	815-831B	The Growth of Tubular or Vermicular Structures in Organic Monotectic Systems. Modeling of Equiaxed Microstructure Formation in Casting. Metastable Phase Equilibria in the Lead—Tin Alloy System. I. Experimental. Metastable Phase Equilibria in the Lead—Tin Alloy System. II. Thermodynamic Modeling. The Evolution of Microstructure in the Undercooled Zn—Sn Entrained Droplets. Superplasticity Deformation of Whisker-Reinforced Metal-Matrix Composities Under Changing Temperature Conditions. Simulation of Static and Deformation-Enhanced Grain Growth Effects on Superplastic Ductlify. Supersaturation Metastable Phase Equilibria in the Lead—Tin Alloy System. I. Experimental. Metastable Phase Equilibria in the Lead—Tin Alloy System. II. Thermodynamic Modeling. Precipitation of Silicon in Aluminum—Silicon: a Calorimetric Analysis of Liquid-Quenched and Solid-Quenched Alloys. Surface alloying Improving Tantalum's Oxidation Resistance by Al* Ion Implantation. Surface analysis (chemical) Ion Beam Characterization and Treatment. Surface diffusion See Diffusion Surface Analysis of Shape Instabilities in Plates. Surface Araburizing	311-322A 785-794A 795-803A 2109-2115A 2355-2368A 2783-2792A 785-794A 795-803A 1207-1214A 2101-2108A 2627-2636A
Aluminum and A356 Melts. Structural hardening See Precipitation hardening Strain aging Strain aging Strain hardening Structural members See I beams Structural shapes See I beams Structures (crystalline) See Acicular structure Crystal structure Equiaxed structure Equiaxed structure Graphitic structure Graphitic structure Graphitic structure Lameliar structure Nodular graphitic structure Unit cell Subgrain boundaries See Grain sub boundaries Submerged arc welding Mechanisms of Inclusion Formation in Al—Ti—Si—Mn Deoxidized Steel Weld Metals. Fatigue Crack Growth Behavior of Pressure Vessel Steels and Submerged Arc Weldments in a High-Temperature Pressurized Water Environment. Weld Thermal Cycles and Precipitation Effects in Ti—V-Containing HSLA Steels.	815-831B 1335-1349A 2069-2085A	The Growth of Tubular or Vermicular Structures in Organic Monotectic Systems. Modeling of Equiaxed Microstructure Formation in Casting. Metastable Phase Equilibria in the Lead—Tin Alloy System. I. Experimental. Metastable Phase Equilibria in the Lead—Tin Alloy System. II. Thermodynamic Modeling. The Evolution of Microstructure in the Undercooled Zn—Sn Entrained Droplets. Superplasticity Deformation of Whisker-Reinforced Metal-Matrix Composities Under Changing Temperature Conditions. Simulation of Static and Deformation-Enhanced Grain Growth Effects on Superplastic Ductlify. Supersaturation Metastable Phase Equilibria in the Lead—Tin Alloy System. I. Experimental. Metastable Phase Equilibria in the Lead—Tin Alloy System. II. Thermodynamic Modeling. Precipitation of Silicon in Aluminum—Silicon: a Calorimetric Analysis of Liquid-Quenched and Solid-Quenched Alloys. Surface alloying Improving Tantalum's Oxidation Resistance by Al* Ion Implantation. Surface analysis (chemical) Ion Beam Characterization and Treatment. Surface diffusion See Diffusion Surface energy Two-Dimensional Finite Difference Analysis of Shape Instabilities in Plates. Surface hardening See Carburizing Ion nitriding Nitriding	311-322A 785-794A 795-803A 2109-2115A 2355-2368A 2783-2792A 785-794A 795-803A 1207-1214A 2101-2108A 2627-2636A
Aluminum and A356 Melts. Structural hardening See Precipitation hardening Strain aging Strain hardening Structural members See I beams Structural shapes See I beams Structures (crystalline) See Acicular structure Crystal structure Equiaxed structure Equiaxed structure Graphitic structure Graphitic structure Graphitic structure Lamellar structure Hierostructure Nodular graphitic structure Quasicrystallines structure Unit cell Subgrain boundaries See Grain sub boundaries See Grain sub boundaries See Grain sub boundaries See Grain Sub See Healed Are Weldments in a High-Temperature Pressurized Water Environment. Weld Thermal Cycles and Precipitation Effects in Ti—V- Containing HSLA Steels. Submerged arc weldids See Welded joints Sulfides The Selective Oxidation of Mixed Metal Sulfides With Lime in the Presence of Steam Without Emitting Sulfur-Containing	815-831B 1335-1349A 2069-2085A 2093-2100A	The Growth of Tubular or Vermicular Structures in Organic Monotectic Systems. Modeling of Equiaxed Microstructure Formation in Casting. Metastable Phase Equilibria in the Lead—Tin Alloy System. I. Experimental. Metastable Phase Equilibria in the Lead—Tin Alloy System. II. Thermodynamic Modeling. The Evolution of Microstructure in the Undercooled Zn—Sn Entrained Droplets. Superplasticity Deformation of Whisker-Reinforced Metal-Matrix Composites Under Changing Temperature Conditions. Simulation of Static and Deformation-Enhanced Grain Growth Effects on Superplastic Ductility. Supersaturation Metastable Phase Equilibria in the Lead—Tin Alloy System. I. Experimental. Metastable Phase Equilibria in the Lead—Tin Alloy System. II. Thermodynamic Modeling. Precipitation of Silicon in Aluminum—Silicon: a Calorimetric Analysis of Liquid-Quenched and Solid-Quenched Alloys. Surface alloying Improving Tantalum's Oxidation Resistance by Al+ Ion Implantation. Surface analysis (chemical) Ion Beam Characterization and Treatment. Surface energy Two-Dimensional Finite Difference Analysis of Shape Instabilities in Plates. Surface hardening See Carburizing Ion nitriding	311-322A 785-794A 795-803A 2109-2115A 2355-2368A 2783-2792A 785-794A 795-803A 1207-1214A 2101-2108A 2627-2636A
Aluminum and A356 Melts. Structural hardening See Precipitation hardening Solution strengthening Strain aging Strain hardening Structural members See I beams Structural shapes See I beams Structures (crystalline) See Acicular structure Crystal structure Equiaxed structure Equiaxed structure Graphitic structure Graphitic structure Graphitic structure Unit cell Subgrain boundaries See Grain sub boundaries See Grain sub boundaries Submerged arc welding Mechanisms of Inclusion Formation in AI—TI—SI—Mn Deoxidized Steel Weld Metals. Fatigue Crack Growth Behavior of Pressure Vessel Steels and Submerged Arc Weldments in a High-Temperature Pressurized Water Environment. Weld Thermal Cycles and Precipitation Effects in Ti—V-Containing HSLA Steels. Submerged arc welds See Welded joints Sulfides The Selective Oxidation of Mixed Metal Sulfides With Lime in the Presence of Steam Without Emitting Sulfur-Containing Pollutants. Sulfur, Impurities	1335-1349A 2069-2085A 2093-2100A	The Growth of Tubular or Vermicular Structures in Organic Monotectic Systems. Modeling of Equiaxed Microstructure Formation in Casting. Metastable Phase Equilibria in the Lead—Tin Alloy System. I. Experimental. Metastable Phase Equilibria in the Lead—Tin Alloy System. II. Thermodynamic Modeling. The Evolution of Microstructure in the Undercooled Zn—Sn Entrained Droplets. Superplasticity Deformation of Whisker-Reinforced Metal-Matrix Composites Under Changing Temperature Conditions. Simulation of Static and Deformation-Enhanced Grain Growth Effects on Superplastic Ductility. Supersaturation Metastable Phase Equilibria in the Lead—Tin Alloy System. I. Experimental. Metastable Phase Equilibria in the Lead—Tin Alloy System. II. Thermodynamic Modeling. II. Thermodynamic Modeling. Precipitation of Silicon in Aluminum—Silicon: a Calorimetric Analysis of Liquid-Quenched and Solid-Quenched Alloys. Surface alloying Improving Tantalum's Oxidation Resistance by Al+ Ion Implantation. Surface analysis (chemical) Ion Beam Characterization and Treatment. Surface energy Two-Dimensional Finite Difference Analysis of Shape Instabilitics in Plates. Surface hardening See Carburizing Ion nitriding Nitriding Pack carburizing Surface layer	311-322A 785-794A 795-803A 2109-2115A 2355-2368A 2783-2792A 785-794A 795-803A 1207-1214A 2101-2108A 2627-2636A
Aluminum and A356 Melts. Structural hardening See Precipitation hardening Strain aging Strain aging Strain hardening Structural members See I beams Structural shapes See I beams Structures (crystalline) See Acicular structure Crystal structure Equiaxed structure Equiaxed structure Graphitic structure Graphitic structure Graphitic structure Graphitic structure Lameliar structure Nodular graphitic structure Quasicrystalline structure Unit cell Subgrain boundaries See Grain sub boundaries See Grain sub boundaries Submerged arc welding Mechanisms of Inclusion Formation in Al—Ti—Si—Mn Deoxidized Steel Weld Metals. Fatigue Crack Growth Behavior of Pressure Vessel Steels and Submerged Arc Weldments in a High-Temperature Pressurized Water Environment. Weld Thermal Cycles and Precipitation Effects in Ti—V-Containing HSLA Steels. Submerged arc welds See Welded joints Sulfides The Selective Oxidation of Mixed Metal Sulfides With Lime in the Presence of Steam Without Emitting Sulfur-Containing Pollutants. Sulfur, Impurities Hydrogen Embrittiement of Iron—Nickel Alloys.	815-831B 1335-1349A 2069-2085A 2093-2100A	The Growth of Tubular or Vermicular Structures in Organic Monotectic Systems. Modeling of Equiaxed Microstructure Formation in Casting. Metastable Phase Equilibria in the Lead—Tin Alloy System. I. Experimental. Metastable Phase Equilibria in the Lead—Tin Alloy System. II. Thermodynamic Modeling. The Evolution of Microstructure in the Undercooled Zn—Sn Entrained Droplets. Superplasticity Deformation of Whisker-Reinforced Metal-Matrix Composities Under Changing Temperature Conditions. Simulation of Static and Deformation-Enhanced Grain Growth Effects on Superplastic Ductlify. Supersaturation Metastable Phase Equilibria in the Lead—Tin Alloy System. I. Experimental. Metastable Phase Equilibria in the Lead—Tin Alloy System. II. Thermodynamic Modeling. Precipitation of Silicon in Aluminum—Silicon: a Calorimetric Analysis of Liquid-Quenched and Solid-Quenched Alloys. Surface alloying Improving Tantalum's Oxidation Resistance by Al* Ion Implantation. Surface and System Chemical Ion Beam Characterization and Treatment. Surface Interest Chemical Ion Beam Characterization and Treatment. Surface Arburizing Sorface Interest Chemical Ion Intriding Nitriding Pack carburizing Surface Interest Chemical Ion Intriding Nitriding Pack carburizing Surface Interest Chemical Intriding Nitriding Pack carburizing Surface Interest Chemical Interest Carburizing Surface Interest Chemical Interest Carburizing Surface Interest Chemical Interest Carburizing Surface Interest Carburizing Surface Interest Carburizing Surface Interest Carburizing Surface Interest Carburizing Interest Carburizing Surface Interest Carburizing Interest Carburizing Surface Interest Carburizing Interest Interest Interest Interest Interest Interest Interest Interest Interes	311-322A 785-794A 795-803A 2109-2115A 2355-2368A 2783-2792A 785-794A 795-803A 1207-1214A 2101-2108A 2627-2636A 1385-1394A
Aluminum and A356 Melts. Structural hardening See Precipitation hardening Solution strengthening Strain aging Strain hardening Structural members See I beams Structural shapes See I beams Structures (crystalline) See Acicular structure Crystal structure Equiaxed structure Equiaxed structure Graphitic structure Graphitic structure Graphitic structure Unit cell Subgrain boundaries See Grain sub boundaries See Grain sub boundaries Submerged arc welding Mechanisms of Inclusion Formation in AI—TI—SI—Mn Deoxidized Steel Weld Metals. Fatigue Crack Growth Behavior of Pressure Vessel Steels and Submerged Arc Weldments in a High-Temperature Pressurized Water Environment. Weld Thermal Cycles and Precipitation Effects in Ti—V-Containing HSLA Steels. Submerged arc welds See Welded joints Sulfides The Selective Oxidation of Mixed Metal Sulfides With Lime in the Presence of Steam Without Emitting Sulfur-Containing Pollutants. Sulfur, Impurities	1335-1349A 2069-2085A 2093-2100A	The Growth of Tubular or Vermicular Structures in Organic Monotectic Systems. Modeling of Equiaxed Microstructure Formation in Casting. Metastable Phase Equilibria in the Lead—Tin Alloy System. I. Experimental. Metastable Phase Equilibria in the Lead—Tin Alloy System. II. Thermodynamic Modeling. The Evolution of Microstructure in the Undercooled Zn—Sn Entrained Droplets. Superplasticity Deformation of Whisker-Reinforced Metal-Matrix Composites Under Changing Temperature Conditions. Simulation of Static and Deformation-Enhanced Grain Growth Effects on Superplastic Ductility. Supersaturation Metastable Phase Equilibria in the Lead—Tin Alloy System. I. Experimental. Metastable Phase Equilibria in the Lead—Tin Alloy System. II. Thermodynamic Modeling. Precipitation of Silicon in Aluminum—Silicon: a Calorimetric Analysis of Liquid-Quenched and Solid-Quenched Alloys. Surface alloying Improving Tantalum's Oxidation Resistance by Al* Ion Implantation. Surface analysis (chemical) Ion Beam Characterization and Treatment. Surface energy Two-Dimensional Finite Difference Analysis of Shape Instabilities in Plates. Surface hardening See Carburizing Ion nitriding Nitriding Pack carburizing Surface layer Kinetics of Layer Growth and Multiphase Diffusion in Ion-Nitrided Titanium. Ion Beam Characterization and Treatment.	311-322A 785-794A 795-803A 2109-2115A 2355-2368A 2783-2792A 785-794A 795-803A 1207-1214A 2101-2108A 2627-2636A 1385-1394A

Surface tension Estimation of the Surface Tensions of Binary Liquid Alloys.	693-703B	Tensile properties, Heating effects Structure and Properties of a β Solution Treated, Quenched, and Aged Silicon-Bearing Near-α Titanium Alloy.	55-62A
Surface waves The Influence of Tempering Temperature on Small Fatigue Crack Behavior Monitored With Surface Acoustic Waves in Quenched and Tempered 4140 Steel.	1257-1265A	Tensile properties, High temperature effects On Microstructure—Property Correlation of Thermally Aged Type 316L Stainless Steel Weld Metal.	1115-1124A
See Hard surfacing		Tensile properties, Microstructural effects Microstructures and Mechanical Properties of Explosively Consolidated Titanium Powder With a Pressure Medium.	2831-2839A
Surgical implants, Mechanical properties Observations on the Faceted Fatigue Fracture of Cast Co— Cr—Mo Alloy Used for Surgical Implants.	99-103A	Tensile shear strength See Shear strength	2001-2000A
Suspensions See Dispersions		Tensile strength Evidence of a Thin Sheet Toughening Mechanism in Al— Fe—X Alloys.	155-164A
Synthesis Diamond Growth in $O_2 + C_2H_4$ and $O_2 + C_2H_2$ Flames.	1282-1284A	The Influences of Impurity Content, Tensile Strength, and Grain Size on In-Service Temper Embrittlement of CrMoV	
Systems (metallurgical) See Binary systems Quaternary systems		Steels. Particle Bonding, Annealing Response, and Mechanical Properties of Dynamically Consolidated Type 304 Stainless Steel Powders.	2345-2354A 2449-2457A
Ternary systems Tanks (electrolytic)		Analysis of the Temperature Dependence of Strain- Hardening Behavior in High-Strength Steel.	2819-2829A
See Electrolytic cells Tantalum, Heat treatment		Tensile strength, Alloying effects A Comparison of the Fracture Behavior of Two Heats of the	
Improving Tantalum's Oxidation Resistance by Al* Ion Implantation.	2101-2108A	Secondary Hardening Steel AF1410. The Effect of Molybdenum Addition on Properties of Iron Aluminides.	105-123A 751-757A
Tear strength Evidence of a Thin Sheet Toughening Mechanism in Al— Fe—X Alloys.	155-164A	Tensile strength, Coating effects Carbon Fibers Coated With Chromium Carbide Using the Liquid Metal Transfer Agent Technique.	165-170A
Tellurium, Alloying elements Effect of Tellurium on Morphological Transitions in Fe—C— Si Alloys. I. Directional Solidification. Effect of Tellurium on Morphological Transitions in Fe—C—	1867-1873A	Tensile strength, High temperature effects Degradation of Mechanical Properties of Cr—Mo—V and 2.25Cr—1Mo Steel Components After Long-Term Service	87-97A
Si Alloys. II. Auger Analysis. Temper brittleness	1875-1881A	at Elevated Temperatures. Tensile strength, Microstructural effects Effect of Phosphorus on the Formation of Retained Austenite	8/-9/A
Carbide Stability Diagrams in 2.25Cr—1Mo Steels. Temper brittleness, Impurity effects Effects of Manganese, Silicon, and Purity on the Design of	1561-1564A	and Mechanical Properties in Silicon-Containing Low- Carbon Steel Sheet. Cleavage Fracture in Pearlitic Eutectoid Steel.	437-445A 2321-2335A
3.5NiCrMoV, 1CrMoV, and 2.25Cr—1Mo Bainitic Alloy Steels.	2197-2212A	Tensile tests See Tension tests	
Temper brittleness, Microstructural effects Correlation of Microstructure and Tempered Martensite Em-		Tensile yield strength See Yield strength	
brittlement in Two 4340 Steels. The Influences of Impurity Content, Tensile Strength, and	1089-1103A	Tension See Surface tension	
Grain Size on In-Service Temper Embrittlement of CrMoV Steels.	2345-2354A	Tension tests	
Temperature See Curie temperature Glass transition temperature		The Effect of Void Shape on Void Growth and Ductility in Ax- isymmetric Tension Tests. Martensite Formation, Strain Rate Sensitivity, and Deforma-	853-861A
Temperature distribution Temperature gradient		tion Behavior of Type 304 Stainless Steel Sheet. Effect of Strain Rate on Martensitic Transformation During Uniaxial Testing of AISI-304 Stainless Steel.	1239-1246A 2857-2859A
Temperature control Fluid Flow and Bath Temperature Destratification in Gas- Stirred Ladles.	603-611B	Ternary systems, Phases (state of matter) The Thermodynamic Activities of Copper and Iron in the System Copper—Iron—Platinum at 1300°C.	127-135B
Temperature distribution Emission Spectroscopy of Plasma During Laser Welding of		Thermodynamic Properties of the Co—W—C System. Phase Diagrams in Materials Science.	935-956A 1295-1323A
AISI 201 Stainless Steel. Roll Cooling and Its Relationship to Roll Life. Infiltration of Fibrous Preforms by a Pure Metal. I. Theory. Infiltration of Fibrous Preforms by a Pure Metal. II. Experi-	277-286B 2305-2320A 2535-2547A	Phase Diagrams in Materials Science. A Note on the Ag—Au—Ge Equilibrium Phase Diagram. Phase Equilibria in the Al—Fe—C System: Isothermal Sections 1550-2300°C.	1295-1323B 2167-2170A 2703-2706A
ment.	2549-2557A	Ternary systems, Surface properties	
Temperature field See Temperature distribution		Equilibrium Surface Composition of Ternary Alloys. Ternary systems, Thermal properties	215-223A
Temperature gradient Primary Dendrite Spacing and the Effect of Off-Axis Heat Flow.	969-973A	Thermodynamic Consistency of the Ternary Functions. Texture	2047-2055A
Tempering See also Quenching and tempering	909-97SA	See also Rolling texture Characterization of Formability in Cold-Rolled Steel Sheets Using Electromagnetic Acoustic Transducers.	2385-2392A
Heat Treatment Behavior and Tensile Properties of Cr—W Steels. The Effects of Surface Hardening on Fracture Toughness of	463-470A	A Comparison of Ultrasonic and X-Ray Determinations of Texture in Thin Copper and Aluminum Plates.	2431-2447A
Carburized Steel. Carbide Precipitation During Stage I Tempering of Fe—Ni—C Martensites.	519-525A 2749-2765A	Texture, Corrosion effects Application of Modeling of the Texture Dependence of Envi- ronmentally Assisted Crack Growth of Long and Short Cracks to Zircaloy Fuel Tubing.	1943-1950A
Tenacity See Tensile strength		Texture, Deformation effects	7010 10001
Tensile modulus See Modulus of elasticity		Experimental Deformation Textures of OFE Copper and 70:30 Brass From Wire Drawing, Compression, and Tor- sion.	125-131A
Tensile properties See also Elongation Tensile strength		Texture, Microstructural effects The Role of Grain Size and Strain in Work Hardening and Texture Development.	2803-2810A
Yield strength Ultrasonic and Magnetic Analyses of Porosity in Iron Compacts.	571-578A	Thermal cycling Weid Thermal Cycles and Precipitation Effects in Ti—V- Containing HSLA Steels.	2093-2100A
Tensile properties, Alloying effects Combined Effects of Oxygen and Hydrogen on Tensile Properties of a Nb—10 at.% V Alloy.	273-278A	Deformation of Whisker-Reinforced Metal-Matrix Compos- ites Under Changing Temperature Conditions.	2355-2368A
Heat Treatment Behavior and Tensile Properties of Cr—W Steels. Notch Effects in Tensile Behavior of Ni ₂ Al and Ni ₃ Al + B.	463-470A 1247-1255A	Thermal expansion Dependence of the Lattice Parameter of γ' Iron Nitride, Fe ₄ N _{1—x} , on Nitrogen Content; Accuracy of the Nitrogen	1500 15001
Microstructure and Tensile Properties of Fe—40 at.% Al Alloys With C, Zr, Hf, and B Additions.		Absorption Data. Thermal flux	1533-1539A
Tensile properties, Cryogenic effects Cryogenic Toughness of Commercial Aluminum—Lithium Al-		See Heat transmission Thermal measurements	
loys: Role of Delamination Toughening.	485-497A	See Calorimetry	

Thermal properties See Thermal expansion		Titanium, Dopants Determination of Effective Stress and Dislocation Velocity in	4000 40004
Thermal stability Vapor pressure		the Deformation of Titanium-Doped Iron. Titanium, Extraction	1029-1036A
Thermal reduction		Modeling of Fluidized Bed Chlorination of Rutile.	959-966B
See Flash smelting Thermal stability A Research on Hydrogen Cracking in α-Iron.	2379-2384A	Titanium, Heat treatment Kinetics of Layer Growth and Multiphase Diffusion in Ion- Nitrided Titanium.	1819-1832A
Thermal stresses Roll Cooling and its Relationship to Roll Life.	2305-2320A	Titanium, Irradiation Ion Beam Characterization and Treatment.	2627-2636A
Thermochemistry Critical Evaluation of the Thermochemical Properties of Lead	77-85B	Titanium, Mechanical properties Deformation of Rapidly Solidified Dispersion Strengthened Titanium Alloys.	875-887A
Sulfates. Thermocycling See Thermal cycling	77-035	Titanium, Powder technology Microstructures and Mechanical Properties of Explosively Consolidated Titanium Powder With a Pressure Medium.	2831-2839A
Thermodynamics Optical Basicity and the Thermodynamic Properties of Slags.	113-118B	Titanium, Solubility	
The Thermodynamic Activities of Copper and Iron in the System Copper—Iron—Platinum at 1300°C.	127-135B	Solubility of Vanadium in α and β Titanium. Titanium base alloys, Crystal growth	334-337A
Sulfide Capacities of MnO—SiO ₂ Slags. Conceptual Model of the Iron Blast Furnace Considering	137-140B	Isothermal Particle Growth in Two-Phase Titanium Alloys.	39-54A
Thermodynamic and Kinetic Constraints on the Process. Correction to "Thermodynamic Consistency of the Interaction Parameter Formalism".	205-218B 269-275B	Titanium base alloys, Heat treatment Alloy Partitioning in Ti—24AI—11Nb by Analytical Electron Microscopy.	1139-1142A
Discussion of "Thermodynamic Consistency of the Interac- tion Parameter Formalism".	434-439B	Titanium base alloys, Mechanical properties An Analysis of the Low Temperature, Low and High Strain-	
The Mechanism of Oxidation of Ferrous Sulfide (FeS) Pow- ders in the Range of 648-923K.	661-670B	Rate Deformation of Ti—6AI—4V. Deformation of Rapidly Solidified Dispersion Strengthened	863-874A
Estimation of the Surface Tensions of Binary Liquid Alloys. Direct Activity Measurements in Liquid Ag—Cu Alloys Using	693-703B	Titanium Alloys. Grain Egression: a New Mechanism of Fatigue-Crack Initia-	875-887A
a Valved Knudsen Cell—Mass Spectrometer System. Standard Enthalpy of Formation of Scs3is. Standard Gibbs Energies of Formation of the Carbidge of	845-852B 879-882B	tion in Ti—6AI—4V. Simulation of Static and Deformation-Enhanced Grain Growth Effects on Superplastic Ductility.	1715-1725A 2783-2792A
Standard Gibbs Energies of Formation of the Carbides of Chromium by EMF Measurements. Thermodynamic Properties of the Co—W—C System. Phase Diagrams in Materials Science.	911-917B 935-956A 1295-1323A	Titanium base alloys, Microstructure The Microstructure of Rapidly Solidified Ti—Fe Melt-Spun	2841-2845A
Phase Diagrams in Materials Science. Calculation of the $Ti(C_yN_{1-y})$ — $Ti_4C_2S_2$ —MnS—Austenite Equilibrium in Titanium-Bearing Steels.	1295-1323B	Ribbons. Titanium base alloys, Structural hardening	2041-2043A
A Study of the Thermodynamics and Phase Relationships of	1361-1374A	Structure and Properties of a β Solution Treated, Quenched, and Aged Silicon-Bearing Near-α Titanium Alloy.	55-62A
the Fe—Co—S—O Quaternary System. Thermodynamic Consistency of the Ternary Functions. Phase Equilibria of the AI—Li Binary System.	1523-1532A 2047-2055A 2247-2258A	Titanium carbide, Diffusion On the Diffusion of Carbon in Titanium Carbide.	403-411A
Thermoelastic properties See Internal friction Shape memory		Titanium carbide, Synthesis Preparation of Submicron Titanium Nitride Powder by Vapor- Phase Reactions.	493-497B
Snoek effect Thermomechanical treatment		Titanium compounds See also Titanium carbide	
See also Controlled rolling Austenite Recrystallization and Carbonitride Precipitation in Niobium Microalloyed Steels. Standard Gibbs Energies of Formation of the Carbides of	25-38A	Titanium compounds, Mechanical properties Mechanical Properties of High-Temperature Beryllium Inter- metallic Compounds.	1279-1282A
Chromium by EMF Measurements. Thermostability	911-917B	Titanium compounds, Microstructure Microstructure Evolution in TIAI Alloys With Boron Additions: Conventional Solidification.	1847-1859A
See Thermal stability Thickness		Titanium compounds, Phases (state of matter) Phase Structure of the Ti ₁ Cu _{1—x} Fe _x System.	981-985A
Confirmation of a Thin Sheet Toughening Mechanism and Anisotropic Fracture in Ai—Fe—X Alloys.	2337-2344A	Titanium compounds, Solubility The Solubility of Titanium Diboride in Aluminum.	2185-2187A
Thin films, Mechanical properties Mechanical Properties of Thin Films.	2217-2245A	Titanium ores See ilmenite	
Thin films, Synthesis Modeling the Early Stages of Thin Film Formation by Energetic Atom Deposition.	2609-2617A	Titanium steels, Metal working A Creep Technique for Monitoring MnS Precipitation in Silicon Steels.	2707-2715A
Thinners See Solvents		$ \begin{array}{ll} \textbf{Titanium steels, Solubility} \\ \textbf{Calculation of the } \textbf{Ti}(C_yN_{1-y}) & \textbf{Ti}_4C_2S_2 & \textbf{MnS-Austenite} \\ \textbf{Equilibrium in Titanium-Bearing Steels.} \end{array} $	1361-1374A
Thorium, Diffusion Study of the Mechanism of Fast Diffusion of Cobalt in Tho- rium by Diffusion and Internal Friction Measurements.	2289-2297A	Titanium steels, Structural hardening Nucleation Kinetics of Titanium Carbonitride in Microalloyed	
Tig arc welding See Gas tungsten arc welding		Austenite. Tool steels	689-697A
Tilting furnaces See Bottom blown converters		See also High speed tool steels Hot work tool steels	
Tin, Binary systems Metastable Phase Equilibria in the Lead—Tin Alloy System. I. Experimental.	785-794A	Tool steels, Nondestructive testing Acoustic Emission From Intergranular Subcritical Crack Growth.	637-648A
Metastable Phase Equilibria in the Lead—Tin Alloy System. II. Thermodynamic Modeling.	795-803A	Tools See Cutting tools	
Tin base alloys, Casting On the Influence of Coarsening on Microsegregation. Two-Dimensional Model for Twin-Roll Continuous Casting.	247-253A 381-390B	Topography Real-Time X-Ray Diffraction Investigation of Metal Deformation.	595-604A
The Evolution of Microstructure in the Undercooled Zn—Sn Entrained Droplets.	2109-2115A	Effects of Near-Tip Inhomogeneities on Scattering of Ultra- sonic Waves by Cracks.	619-626A
Titanium, Alloying elements Phase Transformations in the Al—Li—Hf and Al—Li—Ti Systems.	999-1019A	Topology Contacting Surfaces: a Problem in Fatigue and Diffusion Bonding.	627-636A
Characterization of Titanium Carbosulfide Precipitation in Ti- tanium Microalloyed Steels.	1907-1915A	Torches See Plasma arc torches	
Titanium, Binary systems Freezing Diagrams. I. Development and Implications for Glass Formability.	287-297A	Torsion Experimental Deformation Textures of OFE Copper and	
Freezing Diagrams. II. Comparison With Experimental Obser- vation and Relevance to Crystallization of Metallic Glass. Characterization of the High-Temperature Phase Fields Near	299-309A	70:30 Brass From Wire Drawing, Compression, and Torsion. Torsional strength	125-131A
Stoichiometric y-TiAl.	1899-1906A	See Shear strength	

Torsional vibration		Tubes	
See Torsion Toughness		See Boiler tubes	
See also Fracture toughness Notch toughness Fracture and Fatigue Crack Propagation Properties of Har-		Tubing (metal), Corrosion Application of Modeling of the Texture Dependence of Envi- ronmentally Assisted Crack Growth of Long and Short Cracks to Zircaloy Fuel Tubing.	1943-1950A
dened 52100 Steel. Toughness, High temperature effects	1961-1973A	Tubing (metal), Materials selection	1545-15001
Degradation of Mechanical Properties of Cr—Mo—V and 2.25Cr—1Mo Steel Components After Long-Term Service at Elevated Temperatures.	87-97A	The Effects of Heat Treatment on the Chromium Depletion, Precipitation Evolution, and Corrosion Resistance of Inco- nel Alloy 690.	2057-2067A
Toughness, Impurity effects Effects of Manganese, Silicon, and Purity on the Design of	Or-ora	Tubing (metal), Mechanical properties The Effects of Hold Time and Frequency on Crack Growth in Alloy 800H at 650°C.	1727-1734A
3.5NiCrMoV, 1CrMoV, and 2.25Cr—1Mo Bainitic Alloy Steels.	2197-2212A	Tubular goods See Tubing (metal)	
See Radioactive tracers		Tungsten, Alloying elements	373-382A
Tracing (radioactive) See Radioactive tracers		The Microstructure of Chromium—Tungsten Steels. Heat Treatment Behavior and Tensile Properties of Cr—W Steels.	463-470A
Transferring See Heat transfer Mass transfer		Tungsten, Composite materials High Temperature Reaction Zone Growth in Tungsten Fiber Reinforced Superalloy Composites. I. Application of the	
Transformations (materials) See Allotropic transformation Martensitic transformations Phase transformations		Moving Boundary Equations. High Temperature Reaction Zone Growth in Tungsten Fiber Reinforced Superalloy Composites. II. Matrix Chemistry Effective Composities.	255-268A 267-272A
Transformer steels		fects. Tungsten, Diffusion	201-2124
See Electrical steels Transgranular fracture		Two-Dimensional Finite Difference Analysis of Shape Insta- bilities in Plates.	1385-1394A
Acoustic Emission From Intergranular Subcritical Crack Growth. The SCC of Single Crystals of β Brass in Water: Fractography	637-648A	Tungsten, Mechanical properties Effect of Oxygen on Tungsten Filament Sag Kinetics.	1144-1146A
and Crystallography. Fatigue Crack Propagation in Rapidly Solidified Aluminum Alloys at 25°C and 300°C.	1439-1444A 2425-2430A	Tungsten, Microstructure On the Formation of Potassium Bubbles in Tungsten Rod. The Microstructure of Rolled and Annealed Tungsten Rod.	179-184A 1669-1686A
Transition metal alloys See Cobalt base alloys		Tungsten, Ternary systems Thermodynamic Properties of the Co-W-C System.	935-956A
Copper base alloys Ferrous alloys		Tungsten arc welding See Gas tungsten arc welding	
Molybdenum base alloys Nickel base alloys Niobium base alloys		Tungsten base alloys, Casting Correction to "Orientation Dependence of $\beta_1 \rightarrow \beta_1$ Stress-	915-923A
Silver base alloys Titanium base alloys Tungsten base alloys Vanadium base alloys		Induced Martensitic Transformation in a Gu—Al—Ni Alloy*. Tungsten base alloys, Powder technology Microstructural Change During Liquid Phase Sintering of W—Ni—Fe Alloy.	837-845A
Zinc base alloys Zirconium base alloys		Turbine blades, Microstructure Observations of Directional Gamma Prime Coarsening Dur-	
Transition metal compounds See Copper compounds Iron compounds		ing Engine Operation. Twinning	683-688A
Molybdenum compounds Nickel compounds Niobium compounds		An Investigation on the Mechanism of 475°C Embrittlement in High-Chromium Ferritic Stainless Steel. [011] Twinning in Fe-Ni-C Martensites.	2563-2567A 2739-2747A
Scandium compounds Titanium carbide Titanium compounds		Twinning, Alloying effects Precipitation and Fine Structure in Medium-Carbon Vanadium and Vanadium/Niobium Microalloyed Steels.	2279-2288A
Zirconium compounds Transition metals		Twinning, Deformation effects	1267-1275A
See Cadmium Chromium Cobalt		Shear Band Formation in Heavily Cold Rolled 70-30 Brass. Twinning, Impurity effects Discussion of "The Mechanism of Silicon Modification in	
Copper Gold Hafnium		Aluminum—Silicon Alloys: Impurity-Induced Twinning*. Ultimate shear strength See Shear strength	1286-1290A
iron Manganese Mercury (metal)		Ultimate tensile strength	
Molybdenum Nickel		See Tensile strength Ultrasonic attenuation	
Niobium Platinum		Characterization of Formability in Cold-Rolled Steel Sheets Using Electromagnetic Acoustic Transducers.	2385-2392A
Precious metals Silver		Ultrasonic Nondestructive Evaluation of Matrix Structures and Nodularity in Cast Irons.	2399-2407A
Tantalum Titanium Tungsten Vanadium		A Comparison of Ultrasonic and X-Ray Determinations of Texture in Thin Copper and Aluminum Plates. Ultrasonic testing	2431-2447A
Zinc Zirconium		Ultrasonic and Magnetic Analyses of Porosity in Iron Compacts.	571-578A
Transmission		New Ultrasonic Methods for Measuring Deformation and Fracture Related Material States.	611-618A
See Heat transmission Transmission gears		Effects of Near-Tip Inhomogeneities on Scattering of Ultra- sonic Waves by Cracks. Contacting Surfaces: a Problem in Fatigue and Diffusion	619-626A
See Gears Transuranium metal alloys		Bonding.	627-636A
See Plutonium base alloys		Undercooling See Supercooling	
Tribology Tribologically-Driven Steady-State Hydrogen Evolution From Mild Steel by Electrochemical Extraction Technique.	557-560A	Unit cell Phase Structure of the Ti ₁ Cu _{1—X} Fe _X System. UP hardfacing method	981-985A
True strain Effect of Strain Rate on Martensitic Transformation During Uniaxial Testing of AISI-304 Stainless Steel.	2857-2859A	See Hard surfacing	
TTT curves Freezing Diagrams. i. Development and Implications for Glass Formability.	287-297A	Upgrading Ferrochromium to Chromium by Nitriding, Leaching, and Dissociation. Uranium, Extraction	219-226B
Freezing Diagrams. II. Comparison With Experimental Obser- vation and Relevance to Crystallization of Metallic Glass.		Fundamental Studies on the Continuous Electrolytic Reduc- tion of Uranyl Sulfate.	337-343B

Fluid Flow in Pachuca (Air-Agitated) Tanks. 1. Laboratory- Scale Experimental Measurements.	781-791B	Wear resistance, Coating effects A TEM Study of CVD TiC _x /Ti(C, N) _x Coating on WC—Co Ce-	
Uranium base alloys, Phase transformations Electron Microscopy Study of the Early Stage of the Marten- sitic Transformation in a U(Ga) Alloy.	1163-1168A	mented Carbide. Wear resistance, Composition effects Friction Properties of AI—1.5Mg/SiC Particulate Metal-Matrix	279-285B
Vacuum annealing The Microstructure of Selected Annealed Vanadium-Base Alloys.	1927-1932A	Composites. Weathering	1564-1566A
Vacuum refining Vacuum Distillation of Copper Matte to Remove Lead, Arse-		The Influence of Weathering on the Reduction of Ilmenite With Carbon. Weld cladding	735-745B
nic, Bismuth, and Antimony. Vanadium, Alloying elements Effects of Second-Phase Particles on Coarsening of Austen-	793-804B	Phase Transformations at Steel/IN625 Clad Interfaces. Weld defects Development of Microstructures in Fe15Ni15Cr Single	665-681A
ite in 0.15% Carbon Steels. The Microstructure of Chromium—Tungsten Steels. Heat Treatment Behavior and Tensile Properties of Cr—W Steels.	13-16A 373-382A 463-470A	Crystal Electron Beam Welds. The Influence of Carbon Content on Austenite—Ferrite Morphology in Fe—Mn—Al Weld Metals.	1125-1138A 2559-2561A
Precipitation and Fine Structure in Medium-Carbon Vanadium and Vanadium/Niobium Microalloyed Steels. Vanadium, Diffusion	2279-2288A	Weld metal, Mechanical properties On Microstructure—Property Correlation of Thermally Aged Type 316L Stainless Steel Weld Metal.	1115-1124A
Isothermal Particle Growth in Two-Phase Titanium Alloys.	39-54A	Weld metal, Metallography	
Vanadium, Irradiation Impurity-Defect Interactions in Radiation Hardening and Embrittlement in BCC Metals.	2637-2649A	Stereo (Scanning Electron Microscopy) Section Fractography of Isolated Cleavage Regions in Nuclear Vessel Steels. Weld metal, Microstructure	2862-2866A
Vanadium, Solubility Solubility of Vanadium in α and β Titanium.	334-337A	Heat Transfer During Nd:YAG Pulsed Laser Welding and Its Effect on Solidification Structure of Austenitic Stainless	
Vanadium base alloys, Microstructure	334-337 A	Steels. The Influence of Carbon Content on Austenite—Ferrite Mor-	957-967A
The Microstructure of Selected Annealed Vanadium-Base Alloys.	1927-1932A	phology in Fe—Mn—Al Weld Metals. Weldability	2559-2561A
Vanadium steels See also Chromium molybdenum vanadium steels Vanadium steels, Diffusion		Inconel 718: a Solidification Diagram. The Influence of Carbon Content on Austenite—Ferrite Morphology in Fe—Mn—Al Weld Metals.	2149-2158A 2559-2561A
A Mass Transport Theory for Interphase Precipitation With Application to Vanadium Steels.	1647-1655A	Welded joints See also Butt welds	
Correction to "A Mass Transport Theory for Interphase Pre- cipitation With Application to Vanadium Steels". Vapor deposition	1647-1655A	Welded joints, Mechanical properties On Microstructure—Property Correlation of Thermally Aged Type 316L Stainless Steel Weld Metal.	1115 11044
A TEM Study of CVD TiC _x /Ti(C, N) _x Coating on WC—Co Cemented Carbide.	279-285B	Welded joints, Microstructure	1115-1124A
Vapor pressure	273-2030	Lower Acicular Ferrite. Weld Thermal Cycles and Precipitation Effects in Ti-V-	1811-1818A
The Thermodynamic Activities of Copper and Iron in the Sys- tem Copper—Iron—Platinum at 1300°C.	127-135B	Containing HSLA Steels.	2093-2100A
Vaporizing Mathematical Modeling of Minor-Element Behavior in Flash Smelting of Copper Concentrates and Flash Converting of	20.545	Welded joints, Nondestructive testing Contacting Surfaces: a Problem in Fatigue and Diffusion Bonding. Welding	627-636A
Copper Mattes. Emission Spectroscopy of Plasma During Laser Welding of AISI 201 Stainless Steel.	39-51B	See Arc welding	
Vapors See Water vapor	277-286B	Diffusion welding Electron beam welding Flux core wire welding Gas metal arc welding	
Veining (cracks) See Cracks		Gas tungsten arc welding Laser beam welding Shielded metal arc welding	
Veining (structure) See Preferred orientation		Submerged arc welding	
Vessels		Welding parameters Prediction of Weld Pool and Reinforcement Dimensions of	
See Pressure vessels Vickers hardness		GMA Welds Using a Finite-Element Model. Heat Transfer During Nd:YAG Pulsed Laser Welding and Its	937-947B
See Diamond pyramid hardness		Effect on Solidification Structure of Austenitic Stainless Steels.	957-967A
Viscosity Diffusivities and Viscosities of Some Gases at Elevated Temperatures: Gas Diffusivities in Porous Solids.	141-148B	Mechanisms of Inclusion Formation in Al—Ti—Si—Mn De- oxidized Steel Weld Metals.	1335-1349A
On Effective Viscosity Models for Gas-Stirred Ladle Systems. Volatilizing	967-969B	Weldments, Corrosion Fatigue Crack Growth Behavior of Pressure Vessel Steels and Submerged Arc Weldments in a High-Temperature	
See Vaporizing Water		Pressurized Water Environment. Welds	2069-2085A
See also Salt water		See Welded joints	
Water, Environment The Role of Crack Tip Strain Rate in the Stress Corrosion Cracking of High Strength Steels in Water.	889-895A	Wettability Wetting of Ceramic Particulates With Liquid Aluminum Alloys. I. Experimental Techniques.	527-532A
Water, Reactions (chemical) Water and Solute Activities in the Aqueous H ₂ SO ₄ — (NH ₄) ₂ SO ₄ Solutions.	13-20B	Wetting of Ceramic Particulates With Liquid Aluminum Alloys. II. Study of Wettability. Tin-Based Reactive Solders for Ceramic/Metal Joints.	533-541A 919-924B
Modification of McKay—Perring Method for the Calculation of Mean Activity Coefficients of Solutes in Mixed Solutions.	110-113B	Wettability, Coating effects Carbon Fibers Coated With Chromium Carbide Using the Liquid Metal Transfer Agent Technique.	165-170A
Water quenching Structure and Properties of a β Solution Treated, Quenched, and Aged Silicon-Bearing Near- α Titanium Alloy.	55-62A	Whisker composites, Crystal growth Recrystallization Microstructure in Cold-Rolled Aluminum Composites Reinforced by Silicon Carbide Whiskers.	1743-1753A
Water vapor, Environment The Influence of Water Vapor on the Fatigue Crack Propagation Kinetics in Pure Aluminum Single Crystals.	925-933A	Whisker composites, Mechanical properties Deformation of Whisker-Reinforced Metal-Matrix Compos-	
Waves See Surface waves		ites Under Changing Temperature Conditions. Wire, Crystal growth	2355-2368A
Wear		An Elastic Recovery Test for Recrystallization.	1885-1887A
See also Abrasive wear Roll Cooling and Its Relationship to Roll Life.	2305-2320A	Wire drawing Experimental Deformation Textures of OFE Copper and	
Wear rate, Microstructural effects Comparison of the Microstructures and Abrasive Wear Properties of Stellite Hardfacing Alloys Deposited by Arc Weld-		70:30 Brass From Wire Drawing, Compression, and Torsion. Wolfram	125-131A
ing and Laser Cladding.	1037-1054A	See Tungsten	
Wear resistance See also Abrasive wear		Work hardening See Strain hardening	

149-160B

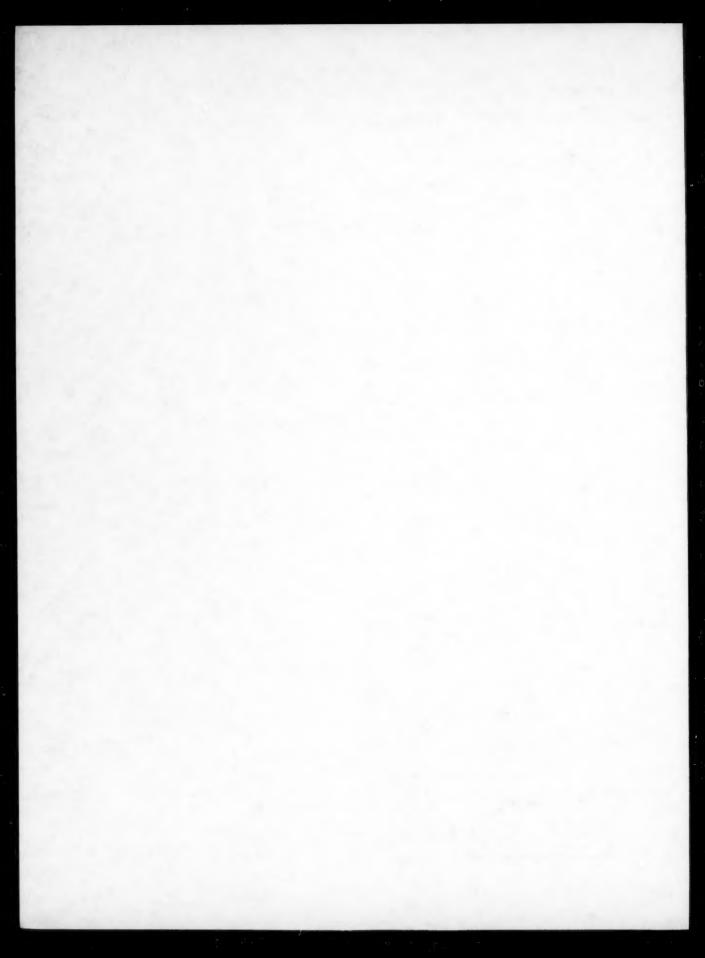
Zone melting Equilibrium Partition Coefficients in Iron-Based Alloys.

Zone refining See Zone melting

Work strengthening See Strain hardening	
Workability See also Formability	
Workability, Pressure effects	
Workability of 1045 Spheroidized Steel Under Superimposed Hydrostatic Pressure.	1735-1741A
X ray analysis See X ray diffraction	
X ray diffraction Real-Time X-Ray Diffraction Investigation of Metal Deforma-	
tion. An X-Ray Diffraction Line Profile Analysis in Cold-Worked Hexagonal (f)-Phase and Mixed (α + f)-Phase of	595-604A
Copper—Germanium Alloys. Bainite Formation in a Silver—Cadmium Alloy. A Comparison of Ultrasonic and X-Ray Determinations of	1142-1144A 1169-1174A
Texture in Thin Copper and Aluminum Plates. X ray diffractometer	2431-2447A
See X ray diffraction X ray emission	
See Emission	
Yield strain See Strain	
Yield strength The Effect of Small Plastic Deformation and Annealing on the	
Properties of Polycrystals. I. Experimental Observations. The Effect of Small Plastic Deformation and Annealing on the Properties of Polycrystals. II. Theoretical Model for the	471-477A 479-484A
Transformation of Nonequilibrium Grain Boundaries. An Analysis of the Low Temperature, Low and High Strain- Rate Deformation of Ti—6AI—4V.	
Computer Simulation of Solid Solution Strengthening in FCC	863-874A
Alloys. I. Friedel and Mott Limits. Computer Simulation of Solid Solution Strengthening in FCC	1411-1418A
Alloys. II. At Absolute Zero Temperature. The Influence of Copper Precipitation and Plastic Deformation Hardening on the Impact-Transition Temperature of	1419-1428A
Rolled Structural Steels. The Rate Dependence and Microstructure of High-Purity Sil-	1657-1668A
ver Deformed to Large Strains Between 0.16 and 0.30 T _m . The Role of Grain Size and Strain in Work Hardening and	2001-2010A
Texture Development. Analysis of the Temperature Dependence of Strain-	2803-2810A
Hardening Behavior in High-Strength Steel.	2819-2829A
Yield strength, Alloying effects A Comparison of the Fracture Behavior of Two Heats of the Secondary Hardening Steel AF1410.	105-123A
Combined Effects of Oxygen and Hydrogen on Tensile Prop- erties of a Nb—10 at.% V Allov.	273-278A
Effect of Copper on the Strength of AISI 316 Stainless Steel. Heat Treatment Behaztor and Tensile Properties of Cr—W Steels.	421-429A 463-470A
Yield strength. High temperature effects	
Degradation of Mechanical Properties of Cr—Mo—V and 2.25Cr—1Mo Steel Components After Long-Term Service at Elevated Temperatures.	87-97A
Yield strength, impurity effects Study of the Hydrogen Internal Friction Peak in Nb—10 at.% V in the Presence of Oxygen.	
	1215-1219A
Yield strength, Microstructural effects Cleavage Fracture in Pearlitic Eutectoid Steel.	2321-2335A
Yield strength, Temperature effects Computer Simulation of Thermally Activated Dislocation Mo-	
tion. III. In FCC Solid Solutions. The Correlation Between the Temperature Dependence of	1429-1437A
the CRSS and the Formation of Superlattice-Intrinsic Stacking Faults in the Nickel-Base Superalloy PWA 1480.	1888-1889A
Deformation of Whisker-Reinforced Metal-Matrix Composites Under Changing Temperature Conditions.	2355-2368A
Discussion of "Correlations of Microstructure With Dynamic and Quasi-Static Fracture in a Plain Carbon Steel".	2860-2862A
Yield stress See Yield strength	
Youngs modulus See Modulus of elasticity	
Zinc, Diffusion	
In Situ Observations of Chemically Induced Grain-Boundary Migration and Discontinuous Precipitation in the Aluminum—Zinc System.	1593-1600A
Zinc, Extraction Fluid Flow in Pachuca (Air-Agitated) Tanks. I. Laboratory- Scale Experimental Measurements.	781-791B
Zinc base alloys, Casting The Evolution of Microstructure in the Undercooled Zn—Sn Entrained Droplets.	2109-2115A
Zirconium, Alloying additive Microstructure and Tensile Properties of Fe—40 at.% Al Alloys With C, Zr, Hf, and B Additions.	
Zirconium base alloys, Corrosion	
Application of Modeling of the Texture Dependence of Envi- ronmentally Assisted Crack Growth of Long and Short Cracks to Zircaloy Fuel Tubing.	1943-1950A
Tirconium compounds Machanical properties	

Zirconium compounds, Mechanical properties Mechanical Properties of High-Temperature Beryllium Intermetallic Compounds.

1279-1282A



Combined Author Index

324-334A 1277-1279A 619-626A 315-325B 315-325B 645-659B 2767-2781A 1029-1036A 2321-2335A 2517-2527A Aaronson, H.I. Achenbach, J.D. Aidun, D.K. Akuezue, H.C. Alden, T.H. Alexander, D.J. Alexander, J.I.D. 2321-2335A 2517-2527A 793-804B 2117-2131A 1395-1409A 17-24A 334-337A 39-54A 2811-2818A 1888-1889A 523-533B 555-565B 251-262B 249-958R Allaire, A. Allen, S.M. Alpas, A.T. Ando, T. Ankem, S. Antolovich, S.D.

949-958B 853-861A 2862-2866A 1657-1668A

1411-1418A 1419-1428A

1429-1437A 5-12B 579-593A 1089-1103A

1951-1959A 1037-1054A 889-895A 13-20B

13-20B 110-113B 485-491B 337-343B 555-565B 573-580B

763-771B 2289-2297A 665-681A 143-153A

107-110B

107-110B 39-51B 773-779B 2561-2563A 1139-1142A 564-566A 391-402B 403-419B 773-779B 403-411A 1833-1845A 149-160B 853-861A

149-160B 853-861A 184-188A 2069-2085A 755-756B 2673-2680A 2321-2335A 447-451A 909-919A

1961-1973A 1875-1881A 1811-1818A

291-313B

2167-2170A 1951-1959A

Anyalebechi, P.N. Aoki, M. Apelian, D. Appleby, E.J. Armstrong, R.W. Aróztegui, J.J. Arsenault, R.J.

Asaki, Z. Asaro, R.J.

Assefpour-Dezfuly, Atamert, S. Atrens, A. Awakura, Y.

Axtell, S.C.

Baek, H.D. Bailey, L.K. Ballester, A. Banester, A. Bamola, R.K. Banerjee, D. Banerji, A. Barr, P.V.

Barril, M.A. Bastin, G.F. Basu, B. Battle, T.P. Becker, R. Beckman, J.P. Begiey, J.A. Belton, G.R. Bench, M.W.

Beswick, J.M. Bevolo, A.J. Bhadeshia, H.K.D.H.

1811-1818A 1037-1054A 2191-2194A 547-550B 2171-2175A 1475-1482A 2695-2701A 1439-1444A 137-140B Bharti, A. Bharti, A.
Bhattacharya, I.N.
Biancaniello, F.S.
Birnbaum, H.K.
Bischoff, E.
Blanchard, W.K., Jr.
Blander, M.
Blazquez, M.L.
Boatner, L.A. 773-779B 1125-1138A 2197-2212A 1021-1028A Bodnar, R.L. Bongartz, K. Borzone, G. Bose, A. Bourgeois, T. Brailsford, A.D. Brasche, L.J.H. Braski, D.N. Briant, C.L. Bodnar, B.L. 1021-1028A 2167-2170A 3100-3103A 421-429B 2583-2598A 627-836A 1927-1932A 179-184A 1669-1686A 2170-2171A 2025-2032A 227-235B 391-402B 403-419B 595-601B 603-611B 291-313B

Bros, J.P.

Buck O

Bui, R.T. Burke, M.G. Butler, J.E.

Cahoon, J.R. Caley, W.F. Canright, D. Cao, W.-D. Carlson, O.N.

Carolan, R.A. Carrington, W.A. Castillejos, A.H.E.

Caulfield, T.

Chakraborti, N. Chan, A.H. Chan, K.S.

Chang, L. Chang, S.K. Chang, Y.A.

Chang, Y.W. Chao, C.G. Charette, A. Chattopadhyay, K.

Chaubal, P.C. Chen, E.C. Chen, H. Chen, H.C. Chen, S. Chen, S.-W. Chen, T.-K. Chen, T.T. Cheruvu, N.S.

Chiba, A.
Chikwembani, S.
Chilton, J.P.
Cho, E.H.
Choi, W.
Choo, W.K.
Chou, C.-P.
Chu, W.Y.
Cleslak, M.J.
Clapp, P.C.

Cockcroft, S.L. Cohen, M.

Collur, M.M. Comstock, R.J. Cooke, A.V. Coombs, P.G. Cornie, J.A.

Coudert, J.F Courtney, T.H. Cowie, J.G. Cramb, A.W.

Daehn, G.S. Daeubler, M. Dariel, M.P. Das, S.C. David, S.A.

Davidson, D.L. Davis, S.H. Dayan, D. De, M.

Debroy, T. Denholm, W.T. Desbiolles, J.L. Dève, H.E. Devereux, O.F. Dewing, E.W.

Dilawari, A.H.

611-618A 627-636A 273-278A 1215-1219A 421-429B 2651-2661A

197-203A 31-37B 225-235A 1687-1699/ 2289-2297A 273-278A 1215-1219A 1215-1219A 421-429A 1282-1284A 595-601B 603-611B 255-266A 267-272A

925-935B 71-76B 2337-2344A 155-164A 2369-2378A 2717-2737A 87-96B 2247-2258A 795-803A 1523-1532A 187-196B 431-436A

421-429B 805-812A 2109-2115A 87-96B 87-96B 699-710A 437-445A 1169-1174A 2247-2258A 1461-1473A 345-361B 2345-2354A 87-97A

2831-2839A 1221-1231A 21-29B 567-571B 567-571B 1975-1987A 205-214A 2559-2561A 1475-1482A 2149-2158A 2087-2092A 1601-1615A

1617-1629A 227-235B 2739-2747A 2749-2765A 277-286B 1943-1950A

661-670B 2535-2547A 2549-2557A 527-532A 533-541A 263-276B 1385-1394A 143-153A 755-756B

2355-2368A 447-451A 1163-1168A 1125-1138A 1125-1138A 645-659B 2369-2378A 225-235A 1163-1168A 1883-1885A

1142-1144A 277-286B 957-967A 327-3368 311-322A 579-593A 2499-2516A 2185-2187A 671-674B

Dodd B.A. Dollar, M. Doucet, A.B. Doychak, J. Draper, S. Draper, S.L. Dreshfield, R. Drew, R.A.L. 2681-2687A 2689-2693A 447-451A

1483-1493A 499-518A 683-688A

1701-1714A 683-688A 383-389A

1803-1810A 2175-2179A

747-754B 475-483B 345-361B

919-924B

2117-2131A

813-823A 2517-2527A 1395-1409A 493-497B

2187-2190A

161-173B 2117-2131A 573-580B 649-664A 699-710A 437-445A 645-659B 987-998A

987-998A 1411-1418A 1419-1428A 837-845A 141-148B 781-791B

2567-2570A 251-262B 949-958B 263-276B 785-794A 795-803A 883-891B 711-721B

1233-1238A

2695-2701A 2133-2148A 1279-1282A

315-325B 315-325B 2535-2547A 2549-2557A

2449-2457A 863-874A 1943-1950A 2179-2182A 161-173B

21-29B 219-226B

2517-2527A 2517-2527A 1325-1333A 637-648A 853-861B 509-514B 515-521B

71-76B 1657-1668A

2385-2392A

105-123A 127-135B 113-118B 1701-1714A

39-51B 637-648A 493-497B 3100-3103A 2609-2617A 53-59B 1715-1725A

1115-1124A 2011-2015A 1975-1987A

197-203A 349-355A 719-725A

711-718A

773-779B 2355-2368A

5-12B

564-566A 161-173B

161-173B

Drury, W.J. Du, S. Dutrizac, J.E.

Eagar, T.W.
Eager, T.W.
Echeverria, A.W.
Ecker, A.
Edwards, L.
Eiger, G.W.
Eilezer, D.
Elliott, J.F. Elliott, J.F. Elmer, J.W. Enami, K. Enomoto, M. Epperson, J.E. Era, H. Era, H. Erasian, A.H. Essadiqi, E. Esterling, D.M.

Eun, K.Y. Evans, J.W.

Fabietti, L.M. Farouk, B. Fauchais, P. Fecht, H.J.

Felicelli, S.

Feller-Kniepmeier, M. Feng, Q.L. Finn, C.W.

Fischmeister, H.F. Fleischer, R.L.

Fleming, C.A. Flemings, M.C.

Flinn, J.E. Follansbee, P.S. Foster, J.P. Fox, R.T. Frank, R.A. Fray, D.J.

Frazier D.O. Frear, D.R. Friesel, M.A. Fruehan, R.J.

Fujisawa, K. Fukunaka, Y. Fukuoka H

Garrison, W.M., Jr. Gaskell, D.R.

Gaydosh, D.J.
George, D.B.
Gerberich, W.W.
Gerdemann, S.J.
German, R.M.
Ghoniem, N.M.
Ghosh, A.
Gilbert, J.L.
Gill, T.P.S.
Gillis, P.P.

Goel, N.C.

Gonzalez, F. González-Doncel, G. Goto, S. Gotoh, A. Gråbaek, L. Granger, D.A. Grant, N.J. Gray, G.T., III

Green, R.E., Jr. Grewal, G.

Grieveson, P. Grong, Ø. Gross, T.S. Grugel, R.N.

Grushko, B. Gruzieski J.F.

Gschneidner, K.A., Jr.

Guillermet, A.F. Gunderia, A.S. Gungor, M.N. Gupt, K.M. Gupta, G.S. Gupta, S.K. Gutterrez-Miravete, E.

Ha, K.F.

Hajra, J.P. Hall, E.L. Hamano, R. Hamilton, C.H. Hammetter, W.F. Hampikian, J.M. Han, K.H.

Hansen, S.S. Hanssen, L.M. Harada, H. Harris, R. Hassam, S. Headley, T.J. Heinrich, J.C.

Heldt, L.A. Hellawell, A. Herchenroeder, J.W. Hetherington, M.G.

Himbeault, D.D. Hirao, M. Hirato, T.

Hirono, S. Ho, W.-Y. Hoch, M. Hoffmann, M Hogan, L.M. Hojo, H. Hollinshead, Hon, M.H. Hon, M.H. Hong, J.W. Hono, K. Horikawa, H. Horton, J.A. Hour, K.Y. Howard, S.M. Hsiao, C.-M.

Hsu, T.Y. Hu, H. Huang, C.T. Huang, G.L. Huang, J.C. Huang, S.C. Huang, T.A. Hull, D.

Ichinose, S. Ide, T. Iijima, S. Ilegbusi, O.J. Imamura, K. Inal, O.T.

2419-2423A 2259-2266A 523-533B 71-85A 1061-1075A 863-874A 595-604A 334-337A 39-54A 735-745B 1335-1349A 1284-1286A 969-973A 1351-1359A

1575-1583A 935-956A 2305-2320A 2529-2533A 581-594B 925-935B

71-954 2563-2567A 2379-2384A 2047-2055A 1669-1686A 1055-1059A 2783-2792A 2149-2158A 2101-2108A 205-214A 105-123A 2803-2810A 2393-2397A 1743-1753A 25-38A 1282-1284A 649-664A 793-804B

793-8048 2167-2170A 2149-2158A 883-891B 711-721B 1439-1444A 171-177A 171-177A 1575-1583A 2651-2661A 485-491B 337-343B 165-170A

2385-2392A 485-491B 573-580B 337-343B 519-525A 1785-1791A 1785-1791A 215-223A 1286-1290A 381-390B 1495-1507A 431-436A 560-563A 1585-1591A 915-923A 751-757A 1727-1734A 845-852B

845-852B 921-924A 925-933A 1169-1174A 324-334A 197-204B 1239-1246A 1061-1075A 1077-1088A 683-688A 97-106B

915-923A 17-24A 2419-2423A 1637-1646A 2831-2839A 1819-1832A 273-278A 1215-1219A 5-11A 2862-28664

2793-2801A 1847-1859A

Ito, K.	509-514B	Lee, JY.	1793-1802A	Metin, E.	1819-1832A	Platias, S.
	515-521B		2483-2488A	Michal, G.M.	237-245A	Poirier, D.R.
lyengar, G.N.K.	679-685B	Lee, J.K. Lee, S.	1385-1394A 1089-1103A	Michel, D.J. Mikkelsen, B.	2425-2430A 197-203A	
		Lee, SC.	2399-2407A	Miller, M.K.	2651-2661A	
Jacob, K.T.	269-275B	Lee, SM.	519-525A 2483-2488A	Milligan, W.W.	2811-2818A 1888-1889A	Polat, S. Posthill, J.B.
	679-685B 687-691B	Lee, S.S.	2431-2447A	Min, D.J.	863-870B	Potter, D.I.
Jacobson, N.S.	1566-1568A	Lee, Y.Y. Leewis, K.G.	1566-1568A 31-37B	Minato, H.	871-877B 2831-2839A	Pradhan, S.K.
Jaffee, R.I. Jan, CH.	2197-2212A 2247-2258A	Legzdina, D.	1713-1719A	Miner, R.V.	133-141A	Price, D.
Jankowski, A.F.	357-362A	Leo, P.H. Leta, D.P.	1277-1279A 665-681A	Mishra, N.S. Mishra, S.	2819-2829A 2819-2829A	Pugh, J.W.
Jensen, D.J.	2803-2810A 1743-1753A	Leverant, G.R.	2369-2378A	Mitchell, T.E.	499-518A	Pugh, M.D.
Jia, C.L.	1631-1636A 5-12B	Levi, C.G. Levi, I.	1847-1859A 2841-2845A	Mittemeijer, E.J.	1207-1214A 1533-1539A	Purdy, G.R. Pyun, SI.
Jiang, MF. Jie, W.	723-730B	Levoy, N.F. Lewandowski, J.J.	999-1019A 2409-2417A	Miyazaki, S. Miyoshi, T.	915-923A 2419-2423A	•
Jiles, D.C. Jing, K.L.	571-578A 2563-2567A	Lewandowski, J.J.	1247-1255A	Mizoguchi, S.	1375-1383A	Quadakkers, W.J.
Johnson, E.	2259-2266A	Li, B.Q. Li, CY.	141-148B 421-429A	Mohar Ali Bepari, M. Moody, N.R.	13-16A 105-123A	Quadanners, W.J.
Johnson, G.C. Johnson, W.C.	2431-2447A 1175-1189A	Li, J.	981-985A	Moore, J.J.	893-910B	
	2171-2175A	Li, J.C. Li, S.	279-285B 1429-1437A	Morii, K. Morral, J.E.	915-923A 2299-2303A	Radhakrishnan, B. Rahmel, A.
Jonas, J.J.	1361-1374A 1907-1915A	Liang, FL.	1861-1866A	Morris, D.R.	97-106B	
	689-697A	Liang, F.L. Liao, J.	2159-2166A 279-285B	Morris, J.W., Jr. Mortensen, A.	1325-1333A 247-253A	Rajakumar, V. Ramanujan, R.V.
	2707-2715A 987-998A	Liaw, P.K.	2069-2085A		2535-2547A 2549-2557A	Ramaswamy, V.
Jones, L.L. Jones, R.H.	1867-1873A 637-648A	Liebermann, H.H. Liem, I.	63-70A 2695-2701A	Mueller, R.R.	665-681A	Rana, F. Ranganathan, S.
Jones, S.E.	1975-1987A	Lin, F.H.	2305-2320A 2247-2258A	Mukhopadhyay, N.K. Mulazimoglu, M.H.	805-812A 383-389A	Rao, K.T.V.
		Lin, JC. Lin, R.Y.	1785-1791A	Munir, Z.A.	661-670B	Rao, P.K. Rappaz, M.
Kai, J.J.	2057-2067A	Lin, S.	197-204B 921-924A	Muraleedharan, K. Murayama, R.	1139-1142A 2385-2392A	Rath, B.B.
	1077-1088A		925-933A	Murphy, S.M.	2599-2607A	
Kajioka, H. Kale, G.M.	1375-1383A 679-685B	Link, T. Liu, B.Z.	1233-1238A 2379-2384A	Murty, K.L. Musbah, O.A.	2637-2649A 1523-1532A	Reddy, R.G. Reed, J.R.
	687-691B	Liu, C.T.	2017-2023A		1000 1000	Rehbein, D.K.
Kampe, S.L. Kang, C.G.	875-887A 381-390B	Liu, D.S.	2459-2469A 2409-2417A		101 1000	Rehn, L.E. Reid, C.N.
Kang, SJ.L.	837-845A	Liu, M.N.	2057-2067A	Nagamori, M. Nandapurkar, P.	434-439B 883-891B	Reif, W.
Kao, A.S. Kao, W.H.	1735-1741A 2459-2469A	Liu, S.K.	1077-1088A 324-334A	Nathal, M.V.	711-721B	Reuter, K.B.
Kapoor, R.R.	919-924B	Liu, W.J.	1361-1374A	•	133-141A 1701-1714A	Reynolds, W.T., Jr. Ribaudo, C.
Kar, A. Karagoz, S.	363-371A 2695-2701A		1907-1915A 689-697A	Nayeb-Hashemi, H. Nelson, D.V.	727-739A 1257-1265A	
Kashyap, B.P.	2133-2148A 453-462A	Liu, Y.L.	2707-2715A 1743-1753A	Nesarikar, V.V.	1889-1893A	Richards, G.G. Richmond, O.
Kassner, M.E.	2001-2010A	Locci, I.E.	237-245A	Neu, R.W.	1755-1767A 1769-1783A	
Kato, E.	2182-2185A 975-976A	Logsdon, W.A. London, B.	2069-2085A 1257-1265A	Ni, D.S.	2305-2320A	Ridley, N. Rieck, R.M.
Kattamis, T.Z.	2499-2516A	Lorimer, G.W.	1199-1206A	Nickel, H. Nishida, M.	1021-1028A 2831-2839A	Riedl, R.
Katz, J.D. Kaufman, M.J.	175-185B 2171-2175A	Lo, B. Lo, X.	413-419A 413-419A	Nishihara, T.	499-508B 741-749A	Ritchie, R.O.
Kellogg, H.H. Kemori, N.	77-85B 327-336B	Lu, XP. Lui, T.S.	1687-1699A 431-436A	Nishijima, S. Nix, W.D.	2217-2245A	Rizzo, H.F.
Kenik, E.A.	2663-2671A	Lui, 1.5.	431-430A	North, T.H. Notis, M.R.	2093-2100A 543-555A	Robertson, I.M. Rodriguez, P.
Khadkikar, P.S. Kim, JS.	1247-1255A 557-560A			Nourbakhsh, S.	1267-1275A	Romanow, W.J. Romig, A.D., Jr.
King, T.B.	175-185B	MacKay, R.A. Maity, A.K.	133-141A 1142-1144A		2159-2166A 1861-1866A	Rosen, M.
Kirby, A.W. Kirk, M.A.	219-226B 2673-2680A	Majima, H.	13-20B	Nunoue, SY.	975-976A	Roy Chaudhury, G. Rozenak, P.
Kleppa, O.J. Klueh, R.L.	879-882B 373-382A		110-113B 485-491B			Russell, K.C.
Kluen, H.L.	463-470A		337-343B	Oakes, D.B.	1282-1284A	Ryum, N.
Kluken, A.O. Knibloe, J.R.	1335-1349A 1509-1521A		555-565B 573-580B	Oden, L.L.	2703-2706A 705-710B	•
Knorovsky, G.A.	2149-2158A	Manfrinetti, P.	763-771B 1575-1583A	Ogawa, O. Oh, SY.	527-532A	Saitoh, T.
Kobayashi, K.F. Kocaste, Y.S.	1286-1290A 421-429B	Maniatty, A.M.	2179-2182A	Ohhashi, T.	533-541A 2197-2212A	Sakamoto, H.
Kodama, H.	2419-2423A	Mannion, F.J. Manoharan, M.	853-861B 2409-2417A	Ohira, T.	1105-1114A	Sakurai, T. Salcudean, M.E.
Kondo, Y.	5-12B 499-508B	Marder, A.R.	543-555A	Okamoto, A. Olson, F.A.	1917-1925A 237-242B	Sangal, S.
Korth, G.E.	2449-2457A	Margolin, H.	1461-1473A 2159-2166A	Olson, G.B.	2739-2747A	Sano, N.
Koss, D.A. Krauss, G.	875-887A 2279-2288A	Marti I	1861-1866A		2717-2737A 143-153A	
	1239-1246A 188-191A	Marti, J. Martis, R.J.	63-70A 63-70A	O'Rourke, J.A.	2749-2765A	Sagib, M.
Krishna Murthy, G.G.	53-59B	Marwick, A.D. Massalski, T.B.	2627-2636A 1295-1323B	Otsuka, K.	125-131A 915-923A	Sarma, D.S.
Kuhlmann-Wilsdorf, D.	2393-2397A	Massaski, 1.D.	813-823A			Sawada, Y. Schalkoord, D.
Kuhn, HA.	1735-1741A	Masumoto, T.	1295-1323A 5-11A	Padmanabhan, K.A.	1115-1124A	Schober, T. Schulten, R.
Kulcinski, G.L.	2681-2687A 2689-2693A	Masur, L.J.	2535-2547A	Palmer, D.D.	627-636A	Schütze, M.
Kumar, A.	2857-2859A	Matlock, D.K.	2549-2557A 1239-1246A	Pao, YH. Pardo, E.	1105-1114A 937-947B	Seefurth, R.N.
Kundrat, D.M. Kundu, A.L.	205-218B 581-594B	Matsuoka, S.	741-749A	Park, JK.	837-845A	Seetharaman, S.
Kuo, K.H. Kurokawa, H.	279-285B 327-336B	Maziasz, P.J.	373-382A 421-429A	Park, J.S.	1867-1873A 1875-1881A	
Kurzydlowski, K.J.	471-477A	Mazumdar, D.	967-969B	Park, K.Y.	959-966B	Seetharaman, V.
Kwon, H.	560-563A	Mazumder, J.	2267-2277A 2489-2497A	Park, SK. Park, S.K.	13-20B 763-771B	Sehitoglu, H.
		McCullough, C.	363-371A 1847-1859A	Park, YG. Parthasarathy, T.A.	127-135B 1713-1719A	Seigle, L.L.
Laird, C.	2033-2045A	McDermid, J.R.	1803-1810A	Partnasaratny, T.A. Patu, S.	1411-1418A	Sekhar, J.A.
Langer, E.W.	759-767A 99-103A	McEvily, A.J. McKamey, C.G.	741-749A 751-757A	Pehike, R.D.	1419-1428A 149-160B	
Lau, T.W.	2093-2100A	McMinn, A.	2369-2378A	Pekguleryuz, M.O.	815-831B	Selverian, J.H.
Lavernia, E.J. Laxmanan, V.	71-85A 2847-2856A	McNallan, M.J.	1566-1568A 187-196B	Perepezko, J.H.	785-794A 795-803A	Sen Gupta, S.P. Seth, B.B.
Lee, CH. Lee, D.	2559-2561A	McWhorter, L.K.	1885-1887A	Pettersen, K.	847-852A	Seyyedi, J. Shah, N.A.
	1889-1893A 2179-2182A	Medrano, R.E. Mehrabian, R.	2011-2015A 1847-1859A	Pickering, H.W. Piehler, H.R.	1585-1591A 1715-1725A	Shah, N.A. Shamsuzzoha, M.
Lee, D.Y. Lee, H.N.	1089-1103A 2793-2801A	Mehrotra, S.P. Mendelsohn, D.A.	53-59B 1989-1999A	Piekarski, K.	165-170A	Shang, J.K.
Lee, JL.	1793-1802A	Metelnick, M.	1153-1161A	Plantz, D.H.	2681-2687A 2689-2693A	Sharma, R.A. Shechtman, D.

2471-2482A 2847-2856A 883-891B 711-721B

711-721B 693-703B 699-710A 1325-1333A 2101-2108A 1883-1885A 1142-1144A 2471-2482A 1885-1887A 1144-1146A 1803-18100

1021-1028A

2866-2868A 1541-1551A

1541-1551A 1553-1560A 735-745B 1277-1279A 2819-2829A 1564-1566A 805-812A 485-497A 581-594B 311-322A 1125-1138A 1933-1942A

391-4014 137-140B 2425-2430A 627-636A 2619-2626A 1395-1409A 564-566A 711-718A 324-334A 2267-2277A 2489-2497A 227-235B 853-861A 1139-1206A 889-895A 2133-2148A 485-497A 897-908A 813-823A 2673-2680A 1115-1124A 759-767A 2149-2158A 605-610A 547-550B 2187-2190A 527-532A 533-541A

381-390B 2419-2423A 1585-1591A 603-611B 471-477A 479-484A 863-870B 871-877B 431-433B 2101-2108A 55-62A 1375-1383A 1533-1539A 1021-1028A 1533-1559A 1021-1028A 55-1560A 805-813B 747-754B 911-917B 2567-2570A 769-777A 1755-1767A 1759-1778 1833-1845A 543-555A 143-21144A 2345-2354A 893-910B 1286-1290A 897-908A 897-908A 805-813B 2841-2845A

Shekhar, R. Shekhar, R.
Sheppard, T.
Shiang, L.-T.
Shim, I.-O.
Shimada, T.
Shimizu, M.
Shyne, J.C.
Sichen, D.
Siemers, P.A.
Simensen, C.J.
Sicobel, I. K. Singhal, L.K. Sircar, S.

Sisak, W.J. Sisak, W.J.
Skolianos, S.M.
Slavens, G.J.
Slifkin, L.
Smelser, R.E.
Smialek, J.L.
Smith, H.H.
Smith, I.O.
Smith, J.F.

Smith, R.W. Snail K.A. Soepriyanto, S. Sohn, H.Y.

Somers, M.A.J. Son, Y.-H. Song, H. Song, Q. Sotiropoulos, D.A. Speelman, J.L. Speer, J.G. Speiser, R. Speitzig, W.A.

Sridhar, G. Srikanth, S. Srivastava, J.P.N. St. John, D.H.

Staffansson, L.-I.

Stafford, G.R. Stattord, G.R. Stefanescu, D.M. Stevens, M.F. Stickels, C.A. Stone, C.A. Stout, M.G. Stringer, J. Stubbins, J.F.

571-578A 1735-1741A 55-62A 269-275B 2109-2115A 287-297A 299-309A 747-754B 911-917B 1351-1359A 1564-1566A 909-919A 535-546B 2609-2617A 125-131A 2767-2781A 1727-1734A 1647-1655A 1727-1734A 1647-1655A 1647-1655A 375-380B 2399-2407A 1811-1818A Subbajah, T. Subbaiah, T. Suen, J.-M. Sugden, A.A.B. Sun, W.P. Sun, Y.S. Sundararajan, T. 1811-1818A 2707-2715A 1199-1206A 925-935B 2109-2115A 1637-1646A varnamba, P.R. 71-85A

Takeuchi, E. Takeyama, M. Talbot, D.E.J. Talianker, M.

Tangri, K.

Tashiro, K. Taub, A.I. Taylor, K.A.

Tewari, S.N. Theyoz, Ph. Thompson, A.W.

Thompson, R.B.

Thompson, R.G. Thompson, S.W. Tien, J.K.

Todd, J.A.

Toguri, J.M. Tong, Z.-X.

Topor, L. Trapaga, G.M. Traut, D.E. Trivedi, R.

Tsai, C.H.

781-791B

781-7918 1495-1507A 1191-1198A 323A 499-508B 437-445A 1257-1265A

911-917B 1899-1906A 191A 2857-2859A

2267-2277A

2267-2277A 2489-2497A 665-681A 2499-2516A 493-497B 2577-2582A

2577-2562A 853-861A 499-518A 2425-2430A 889-895A 2431-2447A

611-618A 825-836A 1282-1284A

237-242B 237-242B

39-51B 107-110B

1533-1539A 2299-2303A 171-177A 1267-1275A

619-626A 31-37B 25-38A

693-703B 571-578A

611-618A

243-250B

741-749A 2017-2023A

2017-2023A 523-533B 1163-1168A 2087-2092A 499-508B 453-462A 471-477A 479-484A 1593-1600A 2025-2032A 2739-2747A 2717-2737A 2749-2765A 1889-1893A 311-322A 2803-2810A

2803-2810A 447-451A

447-451A 2431-2447A 571-578A 611-618A 627-636A 2866-2868A 2279-2288A

255-266A 267-272A

1647-1655A 1647-1655A

87-96B 921-924A 925-933A 879-882B

879-882B 71-85A 493-497B 2191-2194A 2567-2570A 769-777A

Tsakalakos, T. Tseng, A.A. Tsuchiya, A. Tunca, N. Tyson, W.R.

825-836A 2860-2862A

Ueshima, H. Ueshima, Y. Ünal, A. 573-580B 1375-1383A 833-843B 61-69B 613-622B 110-113B 1657-1668A Uno, A. Urcola, J.J.

Valencia, J.J. van der Kouwe, E.Th.

van der Pers, N.M. van Loo, F.J.J. Van Rooyen, M. Vander Sande, J.B.

Vandermeer, R.A. Vandersande, J.B. Vardelle, A. Vardelle, M. Varin, R.A.

Vedula, K. Verhoeven, J.D.

Vetrano, J.S. Vijayalakshmi, M. Vitek, J.M.

Vivès, C. Voorhees, P.W.

Wagoner, R.H. Wakasugi, T. Wang, G.R. Wang, L.M. Wang, Z.

1483-1493A 1509-1521A 431-433B 2093-2100A

631-643B 1175-1189A

2171-2175A

Watkinson, A.P. Weatherly, G.C. Wechsler, M.S. Weckman, D.C. Weertman, J. Wei, D.Y

Weinberg, F. Welker, M.

Williams, D.B. Wong, C.P. Wood, J.V. Woodford, D.A. Wray, P.J. Wright, J.K. Wright, R.N. Wronski, Z. Wu, C. Wu, Y.P.

Yaguchi, H. Yaguchi, H. Yamaguchi, T. Yamamoto, M. Yamamoto, T. Yang, D.Z. Yang, J.-M. Yao, S.C. Yeum, K.S.

Wynblatt, P.

Yoon, B.H. Yoon, D.N. Youn, I.-J. Yu, G.P. Yu, J. Yu, W. Yu, Z.-Z.

Yue, S. Yukinobu, M.

Zabala, R.J. Zaccone, M.A. Zacharia, T. Zandrahimi, M. 2459-2469A 2057-2067A 2847-2856A 693-703B 2793-2801A 837-845A 959-966B 2057-2067A 1561-1564A 485-497A 1601-1615A 1617-1629A 705-710B

1279-1282A 188-191A 957-967A 645-659B 2471-2482A

Zhang, Ch. Zhang, H.M. Zhang, J. Zhang, L.W. Zhang, M.-X. Zhang, X.J. Zhang, X.

Zhu, M. Zhuang, L.Z. Ziv, I. Zupon, D.E.

619-626A 2563-2567A 1169-1174A 2379-2384A 795-803A 2862-2866A 413-419A 969-973A 723-730B 1631-1636A 99-103A 99-103A 731-734B 1175-1189A

1847-1859A

1077-1088A 357-362A 2305-2320A 555-565B

671-674B 1533-1539A 403-411A 1207-1214A 2739-2747A 2749-2765A 1933-1942A 391-401A 999-1019A 263-276B 263-276B 263-276B 165-170A 1153-1161A 1247-1255A 1867-1873A 1875-1881A 2673-2680A 1115-1124A 957-967A 1125-1138A 623-629B

2681-2687A 2033-2045A 759-767A 391-402B

403-419B 2093-2100A 2637-2649A 937-947B 1221-1231A

251-262B 949-958B 731-734B 1541-1551A 1553-1560A 719-725A 711-718A 63-70A 2259-2266A 184-188A 1191-1198A

363-374B 2449-2457A 1153-1161A 981-985A 267-272A 215-223A

381-390B 2831-2839A

1631-1636A

5-11A 5-12B

A-3